A gamma-ray telescope for on-line measurement of low boron concentrations in a head-phantom for BNCT

Verbakel, W.F.A.R.

Award date:
1997

ECN Nucleaire Energie
NFA-BNCT-94-01

A gamma-ray telescope for on-line measurements of low boron concentrations in a head phantom for BNCT

W.F.A.R. Verbakel

Petten, June 1994

JUNE 1994 NFA-BNCT-94-01

A gamma-ray telescope for on-line measurements of low boron concentrations in a head-phantom for BNCT.

Afstudeerverslag van
W.F.A.R. Verbakel

This investigation has been performed at the ECN in Petten
under supervision of dr.ir. F. Stecher-Rasmussen.

Faculteit Technische Natuurkunde van de Technische Universiteit Eindhoven
Groep Kernfysische technieken onder begeleiding
van prof.dr.ir. M.J.A. de Voigt.

Acknowledgement

The present work has been performed in completion of my study Technical Physics at the Technical University of Eindhoven. My graduation project was carried out at the Netherlands Energy Foundation (ECN) in Petten. During the project I received much assistence from the persons working in the Fermi building. Therefore I want to acknowledge them and all others who supported me. In particular I like to thank my supervisors Finn Stecher-Rasmussen and Han de Haas, also for reading this report and giving essential feedback. Last, but not least, I acknowledge Corine Vroegindeweij, Willy Freudenreich, Evert-jan Vonken and the crew of the LFR for their support. Further I am gratefull to prof. de Voigt and to the ECN for giving me the possibility of performing my graduation project at the institute.

Abstract

In Boron Neutron Capture Therapy the $^{10}B(n,\alpha)^{7}Li$ reaction is used to create a tumor destructing field of the emitted high-LET particles. This reaction is accompanied by the emission of a photon of energy 478 keV. This can serve as a probe for detection of the reaction rate and thereby provide a tool to assess the boron concentration during therapy. An experimental configuration has been designed for on-line measurements of the ^{10}B prompt gamma rays in a background of hydrogen prompt gamma rays, neutrons and gamma rays comming from the reactor. At an epithermal test facility of the Low Flux Reactor a head phantom has been irradiated with neutrons. This phantom is filled with water and a small volume containing 62 ppm ^{10}B, simulating a tumor. The experimental configuration for prompt gamma measurements has been expanded to perform tomography. The reconstruction of the position and the size of the tumor and its boron concentration appeared to be possible.

Next to this, Monte Carlo calculations and foil activation measurements have been performed to obtain the neutron spectrum of this epithermal beam. By the insight achieved with these calculations it has been possible to optimize the neutron flux. By introduction of a graphite scatterer in the beam tube close to the reactor core, the flux has been raised with about 65 %.

With computer code DORT neutron distributions over the phantom have been calculated for 47 energy groups. These calculations are necessary for ultimate boron tomography.

CONTENTS

1. INTRODUCTION

A new irradiation therapy in the battle against cancer is the Boron Neutron Capture Therapy (BNCT). The principle of BNCT is as follows [1]: BNCT is based on the high cross section of ^{10}B for thermal neutrons and its desintegration into two highly energetic particles after neutron absorption. These two particles, a ^{4}He nucleus of 1.5 MeV and a ^{7}Li nucleus of 0.85 MeV, have a range in the tissue of the order of 10 μm. As the energy of these ions is almost totally deposited within one cell, it gives rise to closely spaced ionizing events, resulting in the destruction of that cell. Before being totally stopped, the Li-particle releases a photon of energy 478 keV.

To convert this simple principle into a clinical therapy a multi-disciplinary European Collaboration has been established. The first objective of this collaboration is the treatment of brain tumors at the High Flux Reactor. A tumor seeking boron-compound is injected in the patient. When the boron concentration in the tumor has reached the right level of order several tens of ppm, irradiation of the head with neutrons is started. Compared with healthy tissue, the tumor boron concentration will be about a factor 10 higher.

To obtain thermal neutrons at the tumor position, the head is irradiated with epithermal neutrons (1 eV $< E <$ 0.5 MeV). These are slowed down by the brain tissue, resulting in a thermal flux peaking at a few centimeters under the skull. This irradiation will take place at beam HB11 of the High Flux Reactor (HFR) of the ECN. A succesfull operation of BNCT requires:

- high boron concentration in the tumor,
- low boron concentration in the healthy tissue,
- a field of thermal neutrons over the tumor region.

These first two items are very difficult to assess, as the boron concentration in the tumor and in the blood changes with time after injection. Furthermore the changes of boron concentrations exhibit large deviations for each patient [2, 3]. This is why a solution is sought in which the boron concentration in the tumor and healthy tissue can be measured on-line during irradiation. On-line detection of boron may be possible by prompt gamma ray measurement of the 478 keV photons released by the ^{7}Li. This possible measurement of boron concentration external from the head will be disturbed by the following:

- these boron gamma rays are attenuated by the brain tissue,
- the head will present a large source of different gamma radiation caused by interactions between neutrons and tissue,
- the 478 keV gamma line is Doppler broadened by the recoil of Li, therefore it is not any more an easy treatable Gaussian shaped peak.

From the above arguments appears that it is important to investigate whether the boron peak is recognizable in a whole spectrum of background radiation. Besides it should be investigated whether the boron gamma rays emitted by the tumor are distinguishable from the boron gamma rays originating from the blood and healthy tissue. For these investigations, irradiation of a human head at the HFR is simulated by irradiation of a "phantom" head at the Low Flux Reactor (LFR) at the ECN. There a neutron beam with epithermal and fast neutrons is available, but of much lower intensity.

The neutron spectrum of the beam and the thermal flux distribution over the

head can be obtained by means of calculations with computer codes. The exact position of the tumor can be detected with CT- and MRI-scans. If prompt gamma ray measurements are indeed succesfull, the possibility of reconstruction of the boron distribution in a head (tomography) by a number of measurements will be examined.

2. INTRODUCTION TO REACTOR CALCULATIONS, NEUTRON TRANSPORT

One of the features of nuclear fission is the release of neutrons. Free neutrons decay with a half life of about 12 minutes by emission of a proton, an electron and an antineutrino. In the meantime they can travel through matter and interact, well within their lifetime (in order of msec.). Neutrons have a few ways to interact:

- they can scatter elastically with nuclei loosing kinetic energy,
- they can be absorbed by a nucleus causing nuclear reactions,
- they can be absorbed, leaving the nucleus in a state of high internal energy, an excited state,
- a nuclear reaction of special interest is the fission reaction, which takes place only with nuclei of high mass as uranium, plutonium, etc.

The probabilities for each of these interactions are given by the cross sections σ with unit barns (1 barn = 10^{-24} cm^2), respectively σ_s, σ_a and for the fission reaction σ_f. The absorption cross section can be subdivided into cross sections for (n,γ), (n,α), (n,p), etc. reactions, from which the (n,γ) reaction occurs most frequently. With (n,γ) reactions gamma rays are emitted specific for the isotope and with energies corresponding with the nuclear levels of the newly formed nucleus.
The cross sections strongly depend on the reacting nuclei or isotopes and the energy of the neutron and the total probability for interaction is given by

$$\sigma_t = \sigma_s + \sigma_a + \sigma_f. \tag{2.1}$$

This means that with a uniform beam of neutrons of intensity I cm^{-2}s^{-1} that hits a monolayer with N_a atoms/cm^2, the total number of interactions C cm^{-2}s^{-1} is given by

$$C = N_a I \sigma_t. \tag{2.2}$$

Also a macroscopic cross section Σ

$$\Sigma = N\sigma \tag{2.3}$$

with unit cm^{-1} can be defined. Here Σ represents the mean number of interactions of one neutron over 1 cm, where N is the atom density (nuclei/cm^3). At this definition of Σ, the mean free path of the neutrons can be expressed as

$$\lambda = \frac{1}{\Sigma}, \tag{2.4}$$

at which the mean free path of absorption as well as of scattering can be discriminated. There is also a connection between the total mean free path and the diffusion distance in a straight line (L). Following are some values for λ_a and the diffusion distance before absorption, L_a, for thermal neutrons:

H_2O : λ_a = 45.5 cm, L_a = 2.54 cm,
D_2O : λ_a = 30300 cm, L_a = 160 cm,
C : λ_a = 3120 cm, L_a = 53.5 cm.

The energy dependency of e.g. σ_γ usually passes according to $\frac{1}{v}$ for low energies. For higher energies some resonances may exist (e.g. fig. 2.2).

Because free neutrons are the essence in a nuclear reactor, we like to be able to compute the neutron distribution over a system. This is possible by considering

neutron transport and regarding the neutrons as a free gas in matter. Boltzmann derived an equation to describe the diffusion of gasses: the Boltzmann transport equation. This same equation is also valid to describe the transport of neutrons in a system. Principially this is just a statement of local balance between currents, disappearing due to collision or reaction, and sources produced from material interaction or from external sources.

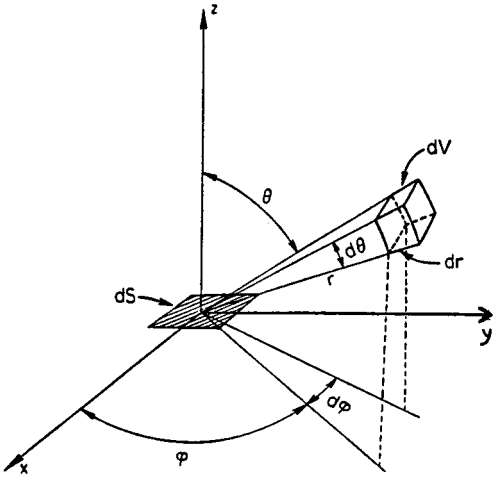

Figure 2.1 *Calculation of neutron fluence rate considering neutron transport.*

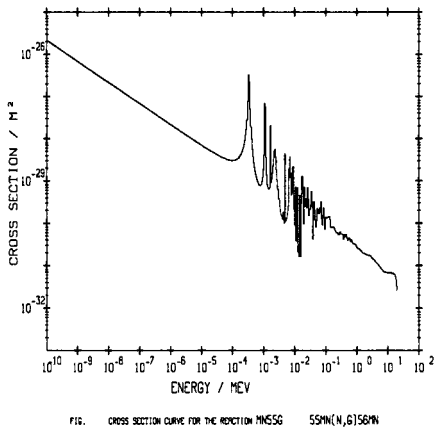

Figure 2.2 *Absorption cross section of the reaction $^{55}Mn(n,\gamma)^{56}Mn$.*

Consider a number of n neutrons in a volume V around position r with energy between E and $E+dE$ and moving in a differential solid angle $d\Omega$ about the direction vector $\vec{\Omega}$ (fig. 2.1). The angular neutron fluence rate with unit $\mathrm{cm}^{-2}\mathrm{s}^{-1}\mathrm{Sr}^{-1}$ is given by

$$\psi(\vec{r}, E, \vec{\Omega}, t) = n(\vec{r}, E, \vec{\Omega}, t)\, v, \tag{2.5}$$

with v the neutron velocity. The scalair fluence rate or flux (ϕ) has unit $\mathrm{cm}^{-2}\mathrm{s}^{-1}$. When S represents an external or an internal source, the neutron transport equation states [4], [5].

$$\begin{aligned}
&\frac{1}{v}\frac{d\psi(\vec{r}, E, \vec{\Omega}, t)}{dt} = S(\vec{r}, E, \vec{\Omega}, t) + \\
&\int_0^\infty \int_{4\pi} \Sigma_s(\vec{r}, E' \rightarrow E, \vec{\Omega}' \rightarrow \vec{\Omega})\, \psi(\vec{r}, E', \vec{\Omega}, t)\, d\Omega'\, dE' - \\
&\vec{\Omega} \cdot \vec{\nabla}\psi(\vec{r}, E, \vec{\Omega}, t) - \Sigma_t(\vec{r}, E)\, \psi(\vec{r}, E, \vec{\Omega}, t)
\end{aligned} \tag{2.6}$$

This equation can be explained as follows: the increase of this angular neutron fluence rate equals the production of neutrons by a source, plus the increase due to scattering from other energies and directions, minus the outflow due to currents, minus the total disappearance due to interaction. However in practice this equation is too complex to be solved analytically, and numerical solutions have to be found.

2.1 Nuclear reactors and slowing down of neutrons

In a nuclear reactor, the neutrons are produced by fission reactions. The number of neutrons emitted per fission is not the same for every individual fission (it depends e.g. on the fission fragments atomic numbers). For example ^{235}U has an average

of $\nu = 2.41$ emitted neutrons for thermal fission. The emitted neutrons have an energy distribution that is drawn in fig. 2.3 and is called the Watt fission spectrum. It can be approximated by:

$$\chi(E) = Ce^{-\frac{E}{a}} \sinh(\sqrt{bE}) \tag{2.7}$$

with a and b constants depending on the kind of fissionable isotope. The component in the source term S of equation 2.6 due to nuclear fission becomes

$$S_f(\vec{r}, E, \vec{\Omega}, t) = \frac{\chi(E)}{4\pi} \int_0^\infty \int_{4\pi} \nu(E')\, \Sigma_f(\vec{r}, E', t)\, \psi(\vec{r}, E', \vec{\Omega}, t)\, dE'\, d\Omega'. \tag{2.8}$$

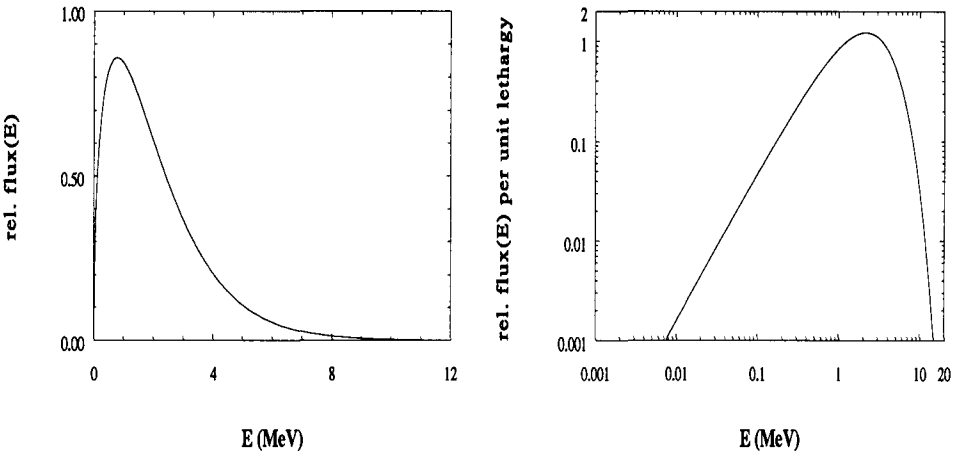

Figure 2.3 *Watt fission spectrum for thermal fission. At the right the relative flux is plotted per unit lethargy (see equation 2.10).*

Neutrons can be divided into three energy classes:

- fast neutrons with $E > 0.5$ MeV,
- epithermal neutrons with about 1 eV $< E <$ 0.5 MeV,
- thermal neutrons with energies smaller than 1 eV.

Thermal neutrons are those in thermal equilibrium with matter at local temperature. Therefore they are distributed according to the Maxwell-Boltzmann distribution. At room temperature (see fig. 2.4), their most probable energy is 0.025 eV, which implies a velocity $v \approx 2200$ m/s.

As in thermal reactors (with ^{235}U as fuel) the fission reaction is started by capture of thermal neutrons, the emitted neutrons have to be slowed down by a moderator material. They lose their kinetic energy by elastic scattering. The maximum energy transfer (for "head on collisions") of a neutron of energy E_0 and energy E' after the collision is

$$\left(\frac{E'}{E_0}\right)_{min} = \left(\frac{A-1}{A+1}\right)^2 = \alpha \tag{2.9}$$

and depends on the mass A of the moderator nucleus. In this way at one collision of a neutron with a ^{1}H nucleus (almost same mass) it is possible for a neutron to loose its total energy. This is why materials containing much hydrogen are used as shielding against neutrons. As, averaged over many collisions, a constant fraction of the neutron energy is transferred per collision, the concept lethargy

$$u = \ln \frac{E}{E'} \tag{2.10}$$

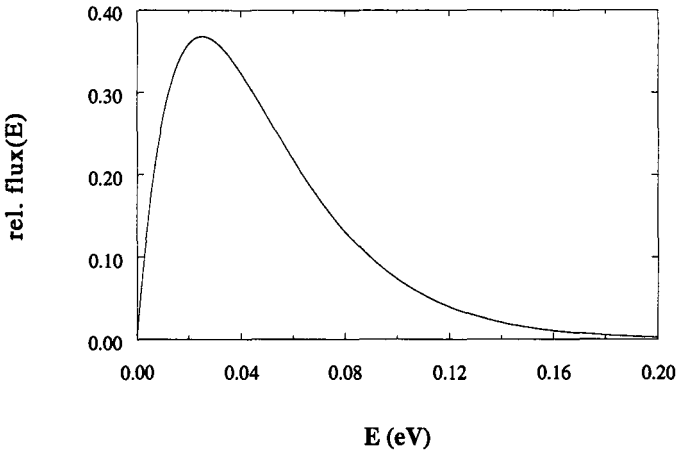

Figure 2.4 *Thermal fluence rate based on the Maxwell-Boltzmann distribution.*

is used in reactor physics (see fig. 2.3).

Considering the slowing down of Q mono-energetic neutrons of energy E_0 in an infinite nonabsorbing medium, it can be derived [5] that the neutron flux per unit energy passes as

$$\phi(E) = \frac{Q}{\Sigma_s E} \tag{2.11}$$

for energies much smaller than E_0. In the case of a nuclear reactor there is no matter of a mono-energetic neutron source. But, as can be seen in fig. 2.3 most emitted neutrons have an E_0 of about 1 MeV. Therefore it

can be expected that the epithermal spectrum of a reactor with a large volume of moderator (Σ_a small), behaves roughly as one over E. The thermal flux energy dependency will be according to the Maxwell- Boltzmann distribution, and the fast neutron flux will be according to the fission spectrum. In this way a schematic flux spectrum has been derived as shown in fig. 2.5

Both graphite and water (H_2O as well as D_2O) are often used as moderator material. To be able to control a nuclear reactor cadmium control rods are used, because cadmium has a very large thermal neutron capture cross section.

At every fission reaction of ^{235}U there is an energy release of 198 MeV distributed to the fission fragments and γ and β radiation. At a power level of P Watt the number of neutrons emitted per second can be calculated as

$$N = \frac{P}{198 \cdot 10^6 \cdot e} \cdot \nu \tag{2.12}$$

with $e = 1.6 \cdot 10^{-19}$ J/eV and $\nu = 2.41$. As the kinetic energy of the fission fragments is converted to heat, the reactors can be cooled by water circulation in which case water also serves as the moderator to slow down the neutrons.

2.2 Low Flux Reactor

The Low Flux Reactor (LFR) at the ECN is a small thermal nuclear reactor of the type "Argonaut". A cross-section is drawn in fig. 2.6a. This reactor operates at a maximal power of 30 kW, and it is only used for research. Fission takes place in 10 fuel elements containing uranium with 90% enriched in ^{235}U, positioned in a "one

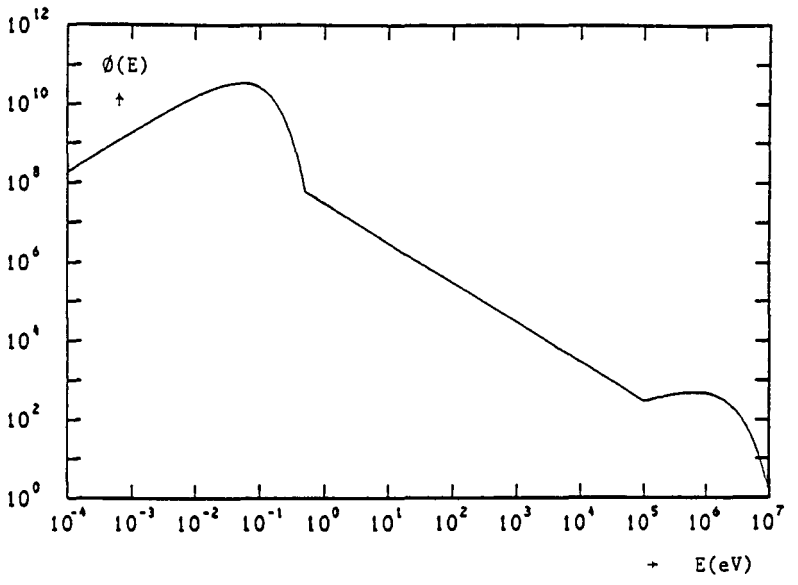

Figure 2.5 *A schematic $\frac{1}{E}$ spectrum in a thermal reactor, linked with a Maxwell-Boltzmann distribution at the low energy side, and a fission spectrum at the high energy side.*

slab core" between an inner and an outer aluminium vessel (see fig. 2.6b). The remaining spaces between the vessels are filled with graphite elements. During operation the interspace between and the space above and below the fuel elements is filled up with cooling water. Besides acting as cooling medium, this water will thermalize fission neutrons to maintain the fission process. The neutrons are moderated as well by means of graphite reflectors inside the inner vessel and outside the outer vessel. The reactor is regulated with one cadmium control rod and there are four Cd safety rods for emergencies and shut down. Because of the low reactor power only 9 grams ^{235}U of the 1.9 kg uranium has been fissioned during 30 years of use.

In the inner graphite reflector five vertical channels are available for irradiation experiments. Larger (biological) irradiation experiments with thermal neutrons can be done on the shielded trolley on wheels on the left of fig. 2.6. In the concrete shielding there are two horizontal beam tubes, HZ and HN, of which the latter has been used for the present experiments. These beam tubes are filled with graphite/concrete plugs when they are out of use.

2.3 Test facility for epithermal neutrons

Beam channel HN is a tangential beam therefore only scattered neutrons leave the reactor there. It has been designed for an epithermal neutron beam. It consists of a square hole in the graphite reflector (7.9 x 7.9 cm^2), and in the concrete shielding an iron beam tube (of inner dimension 10 x 10 cm^2) surrounded by fine sand. There is no graphite between HN and the outer vessel and the channel is directed next to the fuel elements. A circular neutron beam (8 cm diameter) can be formed by putting two neutron collimators of polythene and lead in the beam tube (see fig. 2.7). The polythene is used to stop the fast neutrons and lead is used to reduce the gamma component of the beam. To stop the thermal neutrons of the beam the two collimators are supplied with a filter of 1 mm cadmium.

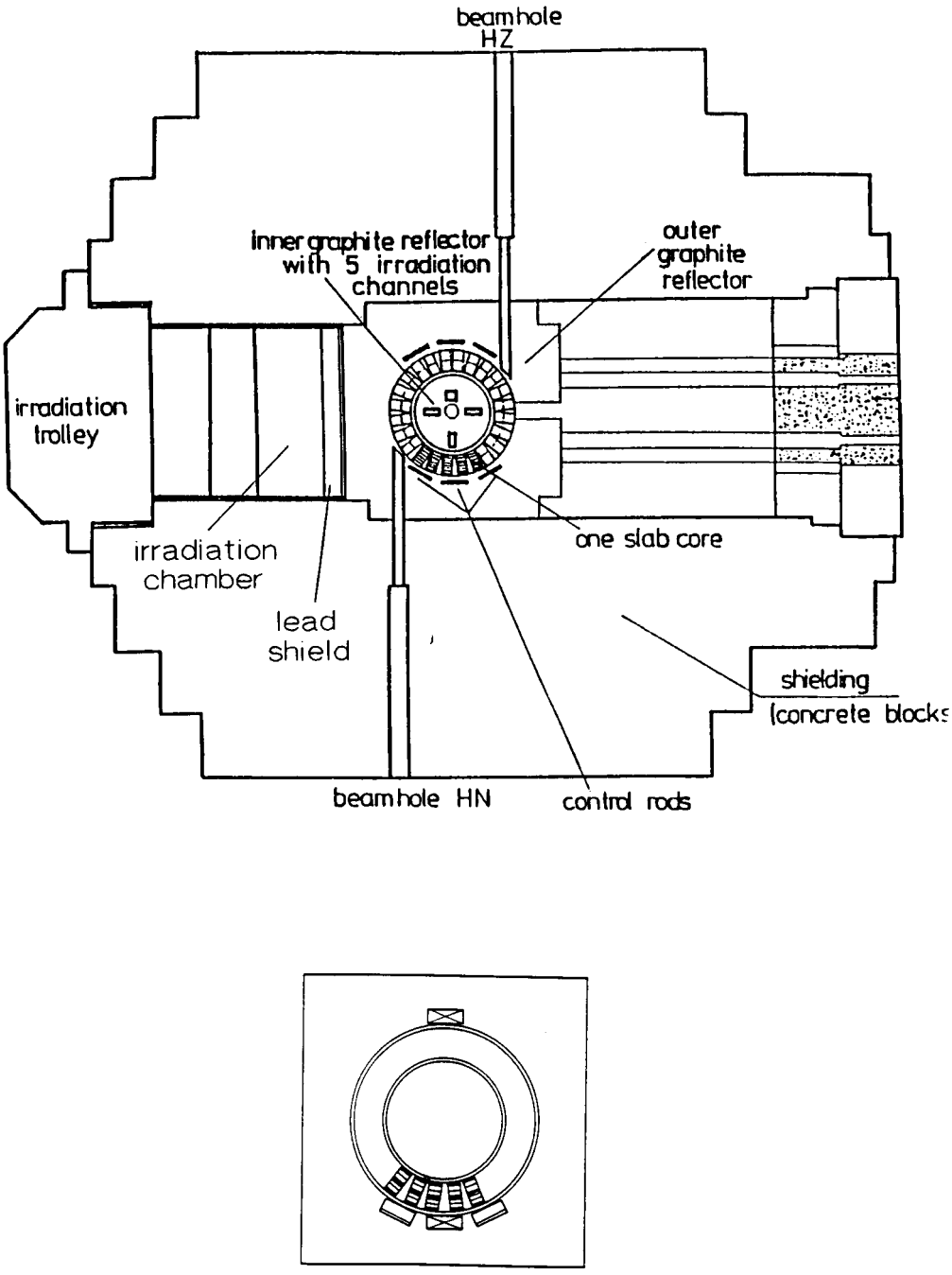

Figure 2.6 *Cross section of the LFR and the "one slab core" configuration.*

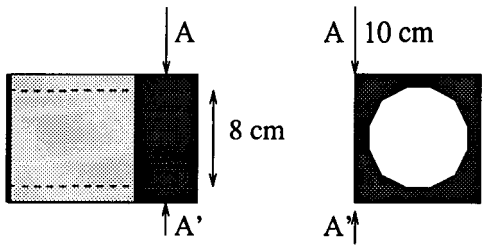

Figure 2.7 *Neutron beam collimator as used in HN. It consists of a Cd filter of 1 mm, 10 cm boron-polythene and 5 cm lead with an aperture of 8 cm.*

For the experiments, a cylindrical phantom (see chapter 3) has to be irradiated in neutron beam HN. The phantom is filled with water containing a small volume of boron with water. During irradiation this phantom can be considered as a large gamma ray source. At some distance the emitted γ radiation will be measured. Because of the large number of scattered neutrons, and the high gamma rate, the surroundings have to be shielded from the experiment. This is done by a wall of 40 to 50 cm of concrete or basalt, covered inside with 5 cm of boron-polythene as can be seen in fig. 2.8. The roof is constructed of 5 cm boron-polythene, 4 cm of steel, again polythene, and some lead. The polythene is used as neutron shielding, lead and steel as gamma shielding and concrete is a shielding material for both of them (it is heavy, and contains a large amount of light elements). The shielding should be such that the total external dose rate reduces to a safe level.

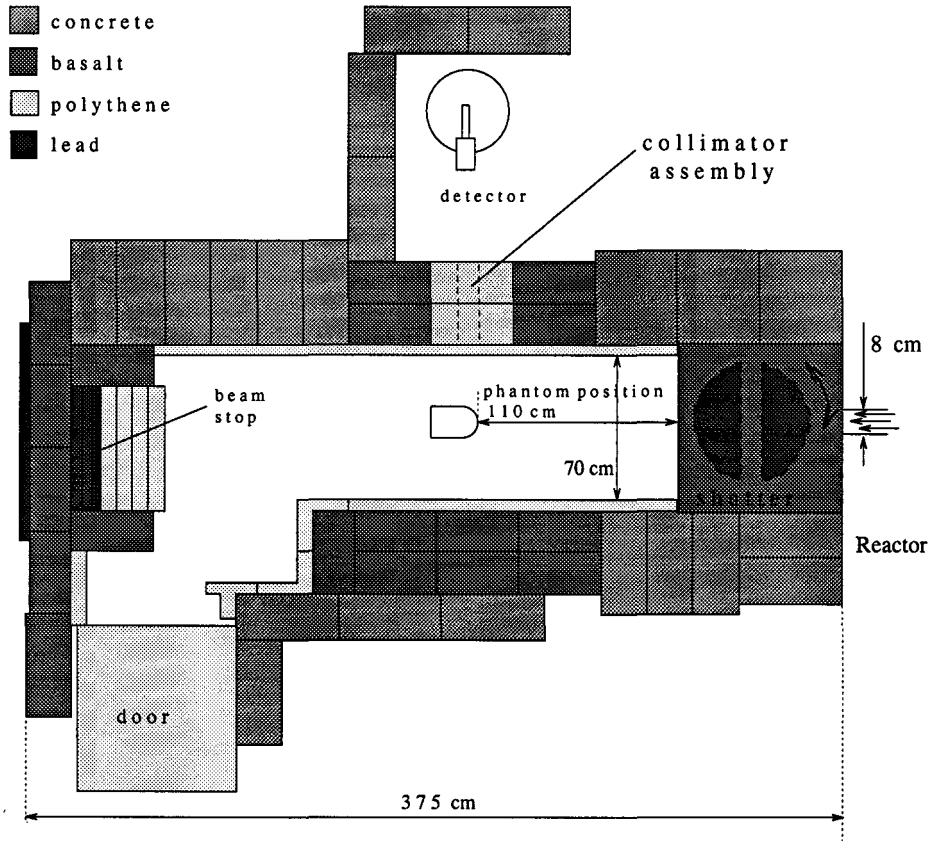

Figure 2.8 *The shielding of the experiment, top view.*

At the exit of the beam tube a shutter enables the closure of the beam when out of use. This shutter can be handled from outside the shielding. At the far end a beam stopper has been designed, made of 30 cm boron-polythene, 15 cm lead and 20 cm basalt. The entrance to this experiment room can be closed with a door of

massive paraffine for shielding.

The phantom (see chapter 3) is positioned by a three points suspension with thin iron chains. In the basalt shielding of the wall an area of 40 cm x 40 cm has been kept free for measuring the gamma rays by means of a HPGe detector (Germanium High Purity).

2.4 MCNP

In chapter 2 could be seen that neutron distributions over a system can be described by the Boltzmann transport equation. However, in practice this equation is impossible to be solved analytically. That is why computer codes are designed that try to approximate a solution of the transport equation. There are two kinds of codes:

1. probabilistic codes,
2. deterministic codes.

The probabilistic codes are based on the Monte Carlo principle: they sample particles and let them travel according to their natural physical probability distributions. In this way the real particle distribution is approximated by a statistical sample. Also secondary particles like gamma rays created by reactions like (n, γ) are sampled. By following a large number of particles statistical fluctuations of the result can be reduced. In deterministic codes the parameters of the transport equation (like space and energy) are divided into discrete regions. Then the Boltzmann transport equation can be numerically solved for all these discrete parts.

An example of a probabilistic code is MCNP (Monte Carlo N-Particle). MCNP is a Monte Carlo program that calculates fluxes of neutrons and/or photons coming from a known source by following a determined amount of particles (NPS) along their tracks. Because MCNP allows many techniques (variance reduction techniques) that are not consistent with physical transport, it is not possible to let every MCNP-particle represent one real physical particle. The sequence of all events along the track(s) of one starting particle is called a history. Each particle carries a weight factor W, and this implies that the ultimate solution (the "tally" you want to know), is normalized per starting particle. Particle tracks are determined by sampling a probability (defined by the cross-sections of interaction of the material) to undergo an interaction during its flight across a medium. Also the scattering angle is determined by sampling of probabilities. For the exact treatment of collisions and sampling in MCNP, reference to the MCNP-manual [6] is made.

In MCNP the geometry of the problem is modelled by defining surfaces, and constructing cells by mentioning the boundary inter surfaces. For each cell the material is defined by it's density and the fractions of constituing elements, referring to the cross-section libraries. In the case of a nuclear reactor, the neutron source can be created by defining a source spectrum, e.g. the Watt fission spectrum (eq. 2.7) and mentioning the distribution of this source over the cells containing the nuclear fuel elements. In that case fission neutrons are repressed.

Fluxes or reaction rates can be obtained by demanding tallies. For example a surface flux tally is calculated as

$$\sum_i \frac{W_i}{\mu A} \ , \tag{2.13}$$

with μ = cosine of angle between surface and particle track,
i = particle crossing the surface,
A = surface area,
W = weight of particle i.

To obtain an absolute flux, this value has to be multiplied by the total number of neutrons produced in the source per second.

Next to this common surface flux tally, also a point detector tally exist. A point detector makes an estimation of the flux at a point by creating, at every source particle release and at every collision, a pseudoparticle that is only used for tallying. At its creation it is send directly to the tally (with reduction in weight). After having made a contribution to the tally the pseudoparticle is killed. The probability for a particle to be scattered into solid angle $d\Omega$ about the direction (θ, ϕ) is $p(\theta, \phi)d\Omega$. If R is the distance from the collision point to the point detector, and dA is a surface element of the point detector, then $d\Omega = \frac{dA}{R^2}$. With $\Sigma_t(s)$ as the macroscopic total cross section at s, the reduction in weight of the pseudoparticle at arriving at the point detector is

$$W_i' = W_i \, p(\theta, \phi) \, \frac{dA}{R^2} \, e^{-\int_0^R \Sigma_t(s) ds} \tag{2.14}$$

Because the flux represents the number of particles passing through a unit area normal to the line of flight, the dA drops out of the equation calculating the point detector flux.

Point detectors can only reliably be used in non-scattering media (air), because the distance to collision (R) must be that large that the $\frac{1}{R^2}$ factor doesn't cause any trouble in statistics. If there is much difference in weight of pseudoparticles that are tallied, the statistics of that tally will fluctuate, causing bad statistics.

2.4.1 Uncertainty

With all tallies, MCNP gives an estimation of the precision of the obtained results. This is more a calculation of the uncertainty of the tally, or the statistical error of the result. If x_i has been defined as the total contribution from the i'th history to the tally ($0 \leq x_i \leq 1$), than an estimation of the variance of the whole population of results is

$$S = \sum_{i=1}^{N} \frac{(x_i - \bar{x})^2}{N - 1} \tag{2.15}$$

with N = total number of histories,
$\bar{x}$ = mean of all the scores x.

An estimation of variance of the mean is given by

$$S_{\bar{x}}^2 = \frac{S^2}{N}, \text{ and } R_S = \frac{S_{\bar{x}}}{\bar{x}} \tag{2.16}$$

with R_S the relative uncertainty given at the result of a tally. Here it is clear to note that R is proportional to $\frac{1}{\sqrt{N}}$. This means that the most important and the easiest way to reduce the uncertainty is to increase the number of histories. The confidence intervals of the solutions behave according to the Gaussian distribution.

MCNP also calculates the FOM (Figure Of Merit):

$$FOM = \frac{1}{R^2 T}, \quad T = \text{computing time.} \tag{2.17}$$

The FOM is a measure of how reliable a calculation is. For an increasing number of histories the computing time increases proportional and the variance reduces by $\frac{1}{\sqrt{N}}$, this means that the FOM should remain constant. In a good calculation the FOM is as large as possible and it doesn't fluctuate. Fluctuations point to instabilities in the precision and it diminishes the reliability of the tally. A possibility to increase the FOM is the use of variance reduction techniques.

One should note the difference between the uncertainty of a Monte Carlo calculation and the systematic error. A solution can be obtained with a good precision, but with a very high systematic error by not well modelling of the problem. The systematic error is a measure of how close MCNP's estimation of the mean is to the real value (see fig 2.9). However this systematic error is something that can only be known by measurements in real. One can obtain an indication of the systematic error by introducing minor changes in the geometry, or the source, or the materials, in a sensitivity study.

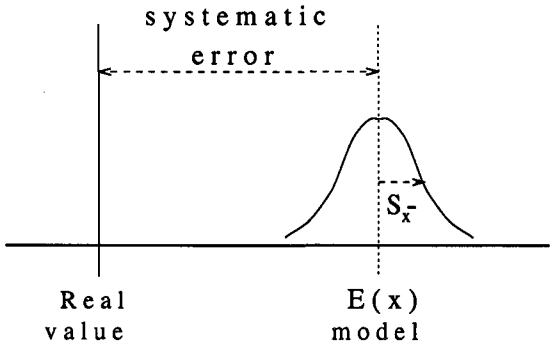

Figure 2.9 *Systematic error and uncertainty.*

2.4.2 Variance reduction techniques

There are a few problems with Monte Carlo simulation: when the defined problem is a very complex one (like calculating fluxes out of a beam tube of a nuclear reactor), the program is busy for a long time by following particles that have very little contribution to the tally. Furthermore, when you want to calculate a flux at a large distance of the source, it is clear by the $\frac{1}{r^2}$-law that the number of starting particles must be very large to obtain any score at that distance.

In MCNP the random walk sampling can be influenced by directing particles more frequently (with a correction for the weight) to a desired region: so called variance reduction techniques [7], [6]. These kind of techniques make it possible to enlarge the FOM. One of them is the Geometry Splitting/Russian Roulette. This is based on more frequently following the particles that have a larger probability of being tallied. When a particle is moving towards a detector (tally position), it can be splitted at a surface into $\frac{I_i}{I_{i-1}} = IN$ (I_i = importance of cell i, $I_i > I_{i-1}$) identical particles, but each with a weight lowered by $\frac{1}{IN}$. Conversely, when a particle is moving away from the detector, the cell importances can be defined such that only one per $\frac{1}{IN}$ particles survives with a larger weight, and the others are killed (Russian Roulette).

A technique much related to that of importance sampling is the use of "weight windows". For each cell and for certain energy intervals lower weight bounds are defined. The upper weight bound is a factor times the lower weight bound. Every particle without suitable weight will be split or rouletted until it has a weight fitting in the window (see fig. 2.10). The advantage of this technique above that with importances, is that, because of the absolute weight bounds, tally fluctuations caused by high weighted particles can be prevented. Whereas geometry splitting is done on the ratio of the importances across a surface, the weight window technique is normally used in combination with other techniques.

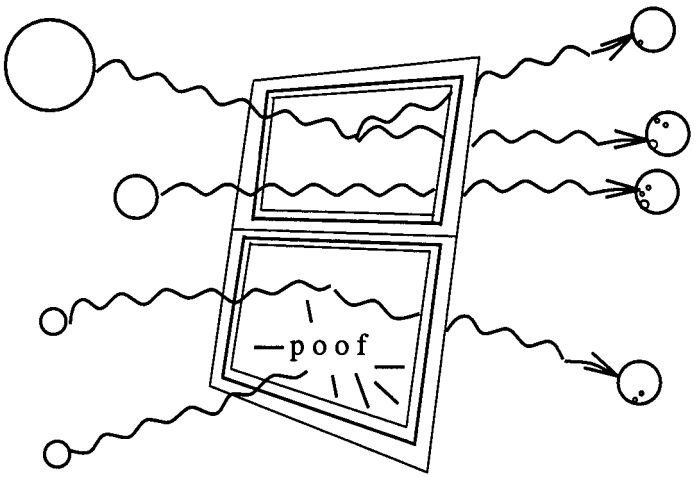

Figure 2.10 *Particle splitting or Russian roulette at a weight window. Particles with weight larger than the upper weight bound are splitted and for particles with weight smaller than the lower weight bound, Russian Roulette is played.*

The build-in weight window generator can be used to let MCNP optimize the weight windows. It generates for all cells the lower weight bounds by assigning them a value inversely proportional to the total score contribution per unit weight entering the cell. One should be very careful at using the weight window generator. When a region is too large or not sampled adequately, the generated weight windows will be very unreliable. All the generated window bounds have to be checked, and adapted by the user if they appear too low, or even worse, too high. The value -1 as weight window means that the particle is killed (capture), and a zero means that the weight will remain unchanged. Both should be prevented as much as possible, especially in the neighbourhood of a tally. Else there may be a possibility for particles with larger weight than the mean to make a contribution to the tally, disturbing the particle balance. Or certain contributions cannot be made because of killing the particle.

2.4.3 DXTRAN

There are typical problems in which a small region is sampled inadequately because of the very little change of particles to be scattered towards that region, like in streaming problems in beams or ducts. Here defining a DXTRAN sphere can be a solution. The DXTRAN technique in MCNP creates at every collision and at every source particle a DXTRAN-particle (pseudoparticle) that is send directly to a specified destination (a DXTRAN sphere). This pseudoparticle gets a correction in weight according to equation 2.14 for the bridged distance. From the DXTRAN sphere it proceeds travelling normally. The real scattered particle, sampled in the normal way, also keeps on existing. However, this last particle,

the non-DXTRAN particle, is killed if it tries to enter the DXTRAN sphere, to conserve the particle balance.

The DXTRAN sphere consists of two concentric spheres, inner and outer (see fig 2.11), with user defined radii. The inner sphere is sampled with a higher probability than the outer sphere. Like at the point detector, care should be taken that the DXTRAN spheres do not cross scattering media. DXTRAN is generally used in combination with weight windows. By using properly defined weight bounds (no zero's in the neighbourhood of the sphere), weights of particles arriving at the sphere can be controlled and fluctuations of the uncertainty can be prevented. This can be seen by achieving a larger value for the FOM.

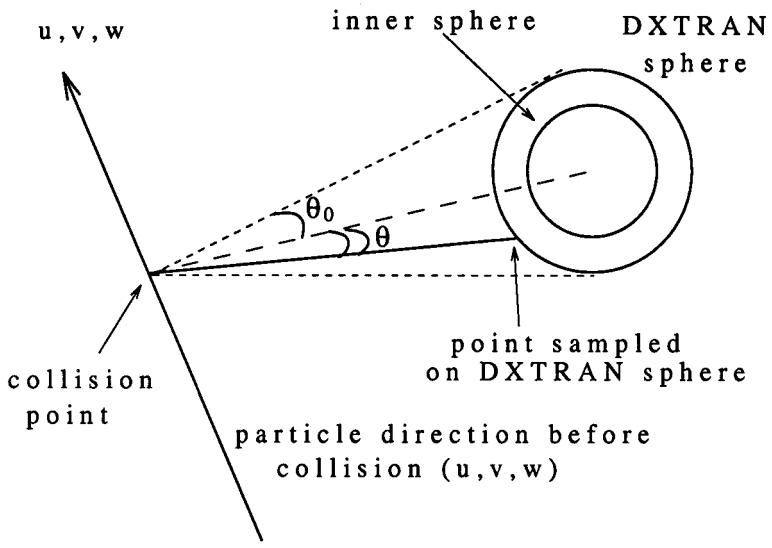

Figure 2.11 *The two DXTRAN spheres*

2.5 Reactor calculations, MCNP

An existing MCNP model of the LFR [8] was extended in the present work with a model of beam channel HN. A horizontal cross section is drawn in fig. 2.12 and the MCNP input file is printed in appendix /refapp MCNP. Not all shielding concrete has been modelled. Inside the beam tube two neutron collimators have been placed, each consisting of a cadmium, a boron-polythene and a lead layer. The fuel elements have been modelled as a homogeneous mixture of uranium, aluminium, carbon and water. Also the graphite ring and the inner and outer vessel have been modelled as mixtures of aluminium, carbon and water.

The source distribution over the fuel cells has been determined by earlier measurements of thermal neutron fluxes [9]. The vertical distribution is shown in fig. 2.13 except for the outer "wings". For the Watt fission spectrum (eq. 2.7) the constants for fission of pure ^{235}U were taken: a = 0.988 keV and b = 2.49 keV^{-1}. As a matter of fact, the LFR is a reactor with highly enriched uranium (about 90%).

The purpose was to calculate the neutron fluxes divided over 47 energy groups, the same groups as in the BUGLE80 library used with DORT, as treated in chapter 3. This has been done for positions inside the beam channel HN at the first collimator, and outside the beam channel at a distance of 110 cm from the shutter. This last position is also the phantom position. Both calculations were checked by foil activity measurements (see chapter 2.6). Calculations are done with MCNP version 4A, using the ENDL85 cross-section tables for neutron

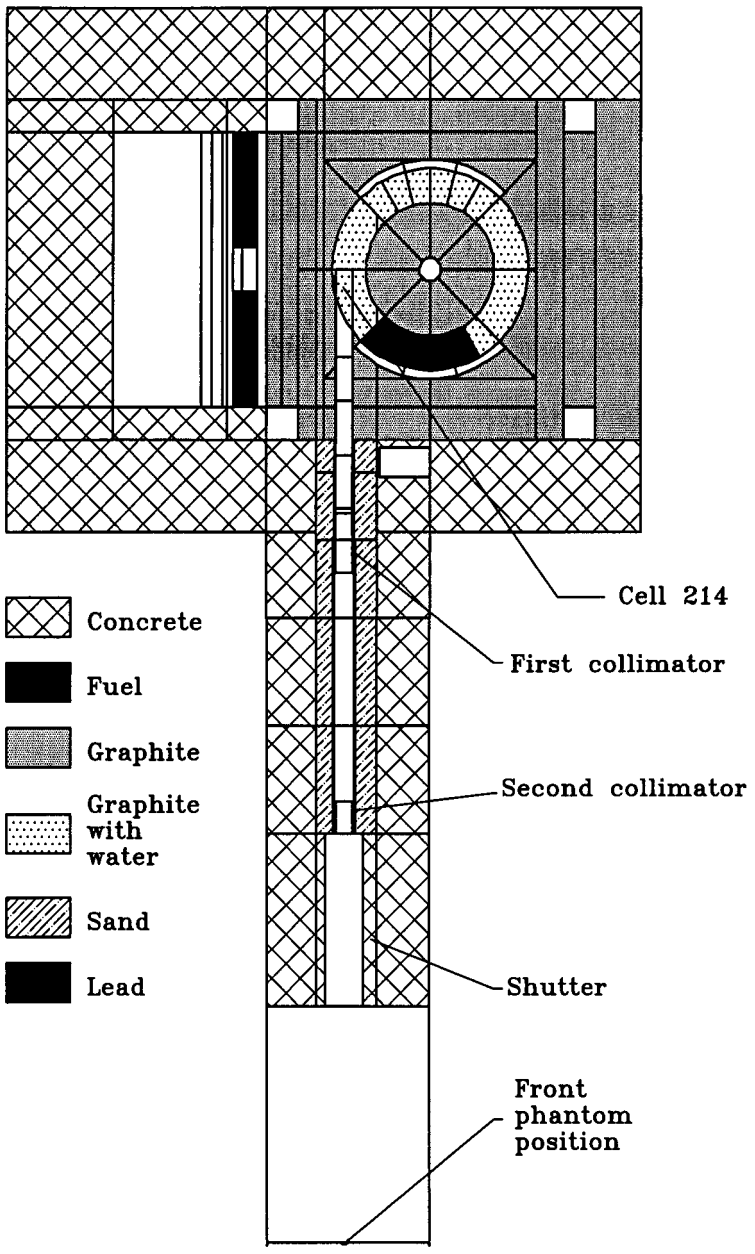

Figure 2.12 *Horizontal cross section of the MCNP model of the LFR.*

transport. For foil activity calculations we used libraries of LEFF13 (for ^{186}W, ^{55}Mn, ^{115}In), L532DOS (for ^{45}Sc, ^{65}Cu, ^{139}La) and again ENDL85 (for ^{197}Au, ^{238}U, ^{58}Ni).

It appeared not to be possible to calculate any fluxes in beam channel HN with only the use of importance factors. The recurrent use of the weight window generator was necessary to obtain an optimized weight window distribution. Highly necessary was to the let it run for more than 100,000 histories so that all the important regions could be sampled, and to check the generated windows for unexpected values afterward. Finally, after much effort had been spend to find the best combination and use of variance reduction techniques, the next MCNP runs were done. One with a DXTRAN sphere with r = 1.5 cm around the foils at the collimator position (for more than 400,000 histories) and one for foils at the phantom position. Calculated were the neutron spectra (undisturbed as well as disturbed by the foils) at the positions and the foil activations. Also the effect

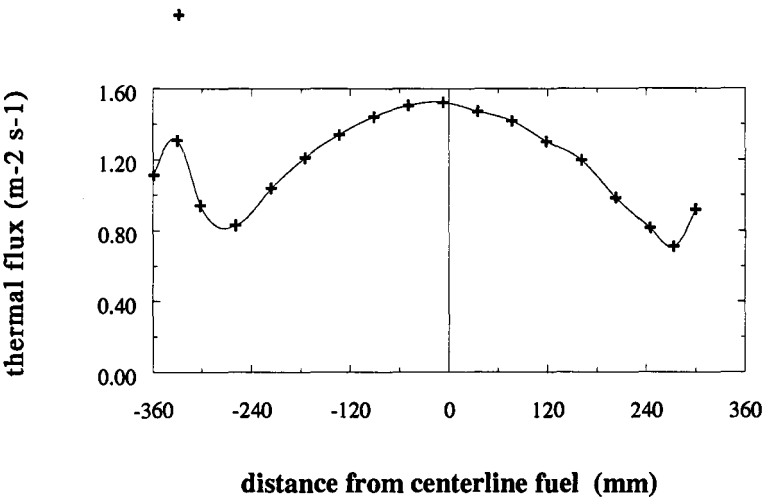

Figure 2.13 *Vertical distribution of thermal neutrons [9].*

on the neutron fluxes by filling the first 30 cm of beam channel HN with graphite and/or polythene has been investigated.

2.6 Measurement of neutron densities by activation detectors

Most materials get activated if irradiated with neutrons. Then they disintegrate with a certain decay constant lambda that represents the fraction $\frac{dN}{N}$ of the excited atoms that decays per second

$$\lambda = \frac{\ln 2}{t_{\frac{1}{2}}} \tag{2.18}$$

with $t_{\frac{1}{2}}$ = half-life time. The contribution to the activity of a sample of mass m with N_m atoms/g at irradiation time t is given by

$$dA(t) = \lambda \, dN \, e^{-\lambda t} \tag{2.19}$$

with

$$dN = m \, N_m \, dt \int_0^\infty \sigma(E)\phi(E)dE. \tag{2.20}$$

Integration over the time yields the activity at irradiation time t

$$A(t) = m \, N_m \, (1 - e^{-\lambda t}) \int_0^\infty \sigma(E)\phi(E)dE. \tag{2.21}$$

If the total irradiation time is very long, a balance is reached between increase in activity by irradiation and decrease by decay. This activity is called the saturation activity and it equals $\frac{dN}{dt}$. In practice the saturation activity per atom is used, also called the reaction rate per atom (R)

$$R = \int_0^\infty \sigma(E)\phi(E)dE. \tag{2.22}$$

This principle can be used for determining a neutron flux by irradiation of foils with a known quantity of an isotope. If a foil has been irradiated by neutrons, the

saturation activity is a measure of the total flux. As can be seen in fig. 2.2 the absorption cross section may have some resonances. The foil activation occurs at those resonances as well as in the thermal region. By making use of several foils with responses at different energy intervals, the flux dependency of the energy can be reconstructed. In order to exclude the thermal response, the foils can be surrounded by cadmium. Examples of foil detectors are

- $^{197}Au(n,\gamma)^{198}Au$ and $^{115}In(n,\gamma)^{116}In$ for low energy neutrons,
- $^{63}Cu(n,\gamma)^{64}Cu$ and $^{55}Mn(n,\gamma)^{56}Mn$ for epithermal neutrons,
- $^{58}Ni(n,p)^{58}Co$, $^{115}In(n,n')^{115m}In$ and $^{27}Al(n,\alpha)^{24}Na$ for the fast part of the spectrum (see fig. 2.14).

A computer program to calculate a neutron spectrum by means of fitting a spectrum with foil activities and cross section libraries, is the program STAYNL. It adjusts a calculated spectrum with measured activities using the generalized least squares method.

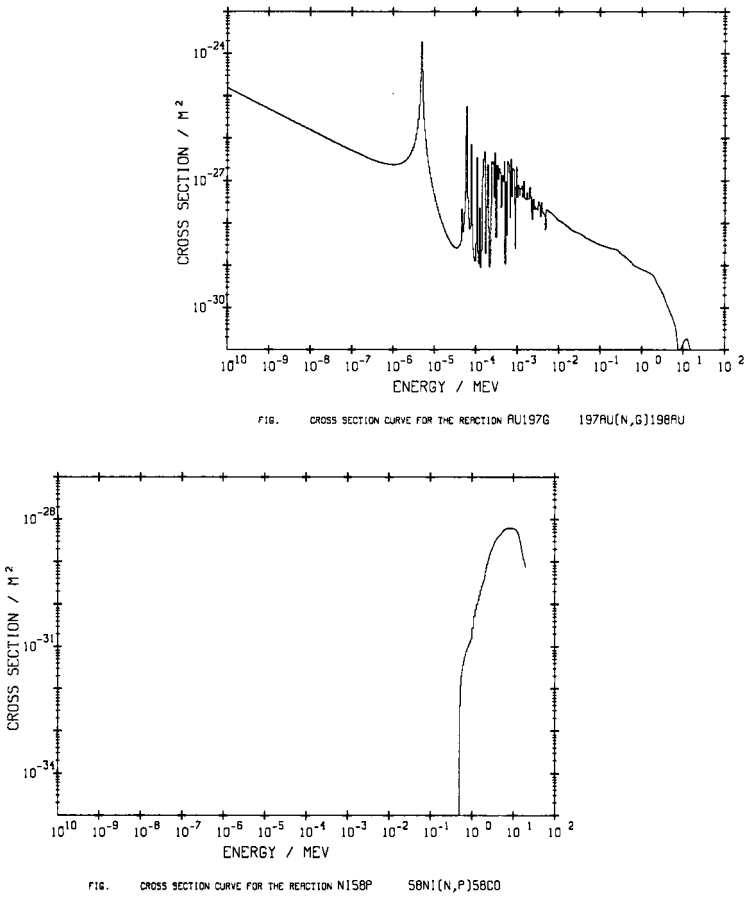

Figure 2.14 *Absorption cross sections for $Au(n,\gamma)$ and $Ni(n,p)$. The latter is only a fast neutron reaction.*

2.7 Calculations and measurements of the HN neutron spectrum

With MCNP, by use of DXTRAN, a neutron spectrum inside the beam tube has been calculated (see fig. 2.15). Also activations for the foils present in the set have been computed in the same calculation. A very good agreement was obtained between the measured and calculated values for the thermal and epithermal part

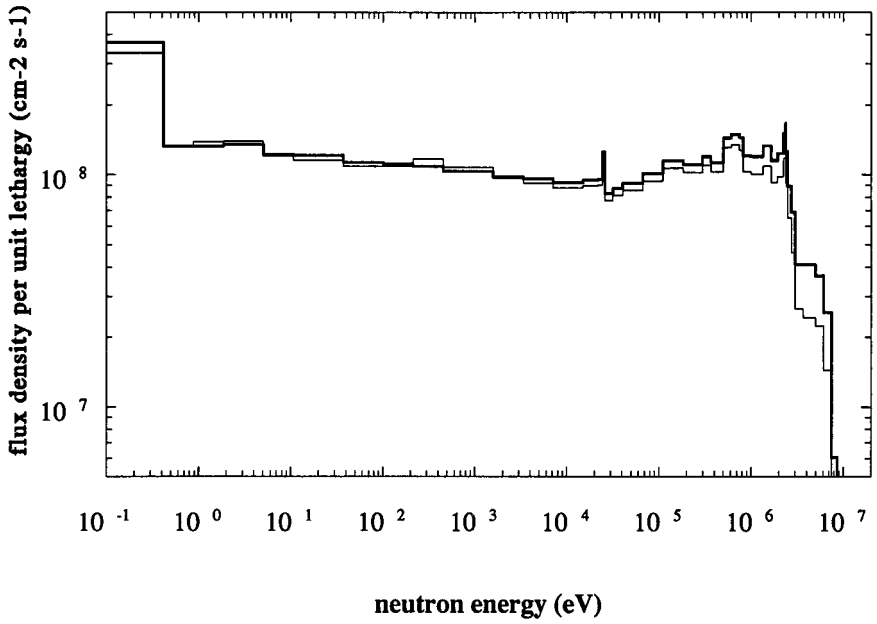

Figure 2.15 *Neutron spectum inside HN, centered on the first neutron collimator. The thick line has been calculated by MCNP without correction for foils, the thin line is the adjusted spectrum. For $E < 4$ MeV the group fluxes calculated by MCNP have uncertainties below 5%.*
The thermal neutron flux ($E < 0.4$ eV) is $2.5 \cdot 10^9$ $cm^{-2}s^{-1}$.

of the spectrum. However, large deviations, up to a factor 2, were found for the fast neutron monitors In, Ni and Al. This is shown in table 2.1. With the spectrum adjustment program STAYNL (using the latest cross section libraries) a spectrum adjustment has been performed (see fig. 2.15). The difference between cross section libraries used by MCNP and the libraries used by STAYNL appears from the table.

In the spectrum, at about 24 keV, the influence of aluminium and of the cast iron beam channel can be seen clearly (these materials have a large resonance in the absorption cross section at about 24 keV). The peak at 2.2 MeV and the peaks and dips around it from 0.3 MeV till 5 MeV are mainly caused by the oxygen of the sand around the beam tube. Apart form these peaks and dips the spectrum resembles rather good the $\frac{1}{E}$ spectrum of fig. 2.5.

The MCNP neutron spectrum at the phantom position is drawn in fig. 2.16. In table 2.3 some group fluxes are mentioned. From table 2.2 it appears that the foil calculations are not consistent with the foil measurements. However, this only concerns the amplitude of the spectrum. This has been calculated a factor 1.5 too high. Spurious trace elements not accounted for in the calculations can easily accommodate for these deviations. The shape of the spectrum is in good agreement with measurements.

The fact that the presence of the elements of the sand are recognizable in the peaks of the spectrum inside HN demonstrates that the sand strongly influences the high energy part of the spectrum. The unavailable data of the sand (like density, composition and amount of water) resulted in the use of estimations. This may have lead to the difference of calculated and measured activities of the high energy foils. The effect of the influence of sand is emphasized by the fact that at the calculations at the phantom position, there was no special deviation in the

Measured and calculated activities of saturation (Bq/atom):

foil reactions	measured (M)	calculated by MCNP (C)	fraction C/M	calculated with STAYNL[1)] C'	fraction C'/M
$^{197}Au(n,\gamma)$	$3.45{\cdot}10^{-13}$	$3.62{\cdot}10^{-13}$ (0.02)	1.05	$3.76{\cdot}10^{-13}$	1.09
$^{115}In(n,\gamma)$	..	$3.80{\cdot}10^{-13}$ (0.04)	..	..	..
$^{45}Sc(n,\gamma)$	$1.51{\cdot}10^{-15}$	$1.39{\cdot}10^{-15}$ (0.02)	0.92	$1.38{\cdot}10^{-15}$	0.91
$^{197}Au(n,\gamma)$	$2.07{\cdot}10^{-13}$	$1.74{\cdot}10^{-15}$ (0.05)	0.84	$1.85{\cdot}10^{-13}$	0.89
$^{186}W(n,\gamma)$	$6.75{\cdot}10^{-14}$	$5.81{\cdot}10^{-14}$ (0.06)	0.86	..	..
$^{238}U(n,\gamma)$	$3.12{\cdot}10^{-14}$	$2.94{\cdot}10^{-14}$ (0.06)	0.94	$2.97{\cdot}10^{-14}$	0.95
$^{139}La(n,\gamma)$	$1.33{\cdot}10^{-15}$	$1.13{\cdot}10^{-15}$ (0.10)	0.85	..	..
$^{55}Mn(n,\gamma)$	$1.61{\cdot}10^{-15}$	$1.71{\cdot}10^{-15}$ (0.03)	1.06	$1.25{\cdot}10^{-15}$	0.78
$^{65}Cu(n,\gamma)$	$5.46{\cdot}10^{-16}$	$5.47{\cdot}10^{-16}$ (0.06)	1.00	$4.99{\cdot}10^{-16}$	0.91
$^{115}In(n,n')$	$2.99{\cdot}10^{-17}$	$1.02{\cdot}10^{-16}$ (0.03)	3.41	$3.70{\cdot}10^{-17}$	1.23
$^{58}Ni(n,p)$	$1.18{\cdot}10^{-17}$	$2.03{\cdot}10^{-17}$ (0.03)	1.72	$1.81{\cdot}10^{-17}$	1.53
$^{27}Al(n,\alpha)$	$5.76{\cdot}10^{-20}$	$1.23{\cdot}10^{-19}$ (0.11)	2.13	$1.29{\cdot}10^{-19}$	2.24

Table 2.1 *Results of the foil activation inside the beam tube. The values between brackets behind the calculated values are their relative uncertainties. The measured values have an uncertainty of 5%.*
To shield them from thermal neutrons all foils except for Al, Ni and the first Au have been surrounded by a cadmium box.
The $In(n,\gamma)$ reaction has not been measured. For the $In(n,n')$ reaction probably a wrong reaction number has been used in MCNP.
[1)] *Before adjustment.*

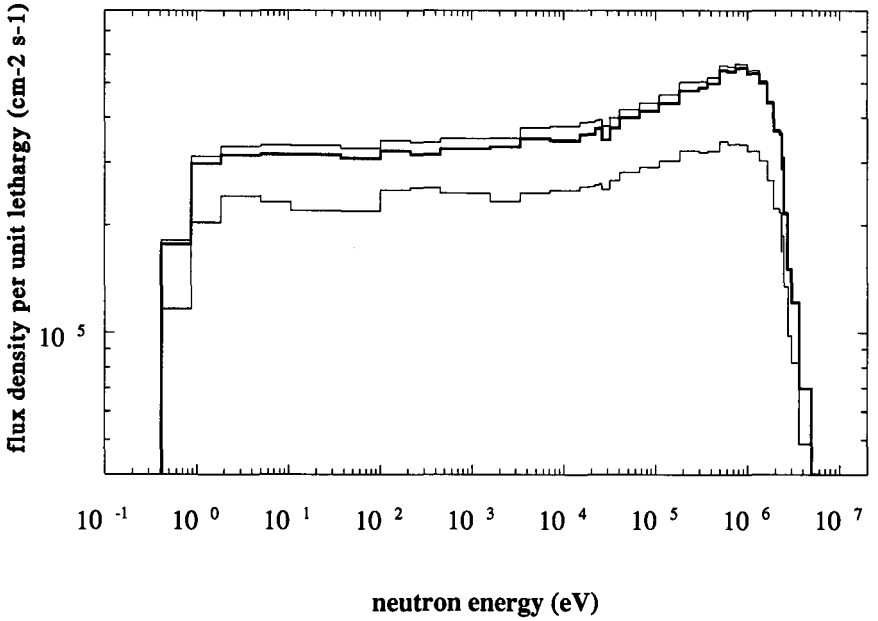

Figure 2.16 *Neutron spectum outside HN, at the phantom position. The upper thin line has been calculated by MCNP without correction for presence of the foil set. The middle thick line is the calculated spectrum after correction for backscattering of the foils. The lower thin line is the adjusted spectrum.*
For $E < 4$ MeV the group fluxes calculated by MCNP have uncertainties below 5%.
The thermal neutron flux according to MCNP is $4.2{\cdot}10^3$ $cm^{-2}s^{-1}$.

spectrum up to the high energy part. This can be explained because no neutrons arrive at the phantom position that have travelled through more than 2 meters of sand, whereas for the position inside the beam tube they have to travel through the sand for maximal 40 cm before reaching the foils.

The influence of the sand on the spectrum inside HN can be seen in fig. 2.17. Here the modelled density of the sand has been raised from 1.5 g/cm^3 to 1.8 g/cm^3, and the hydrogen atom weight fraction has been lowered from 0.5% to 0.15%. The changes are so large that the real spectrum cannot be calculated accurately by MCNP without the knowledge of the exact composition. However, by making a spectrum adjustment also the real spectrum can be obtained because STAYNL adjusts the level of the group fluxes, but the fine structure between neighbouring groups of the input spectrum is maintained.

Later it appeared that 66% of the neutrons at the phantom position has made a collision in cell 214 (fig 2.12). At the foil set on the first collimator only about 10% of the neutrons has scattered in cell 214. Although 63% of that neutrons has travelled through the sand. From these data it is clear that the spectrum inside HN cannot be extrapolated to a spectrum outside HN by just taking into account the attenuation. This is why it can be very dangerous to split a MCNP calculation in two, using the spectrum of the first calculation as a source for the second.

Because at the phantom position the beam can be regarded as a free beam, the influence of the presence of the foil set on the flux has been investigated. It

Measured and calculated activities of saturation (Bq/atom):

foil reactions	measured (M)	calculated by MCNP (C)	fraction C/M	calculated with STAYNL[1)] C'	fraction C'/M
$^{197}Au(n,\gamma)$	$3.73{\cdot}10^{-16}$	$5.48{\cdot}10^{-16}$ (0.04)	1.47	$3.48{\cdot}10^{-16}$	0.93
$^{115}In(n,\gamma)$	$5.99{\cdot}10^{-16}$	$1.08{\cdot}10^{-15}$ (0.04)	1.80	$6.46{\cdot}10^{-16}$	1.08
$^{45}Sc(n,\gamma)$	$2.37{\cdot}10^{-15}$	$3.72{\cdot}10^{-15}$ (0.01)	1.56	$2.19{\cdot}10^{-18}$	0.92
$^{197}Au(n,\gamma)$	$3.65{\cdot}10^{-16}$	$5.47{\cdot}10^{-16}$ (0.04)	1.50	$3.37{\cdot}10^{-16}$	0.92
$^{187}W(n,\gamma)$	$1.33{\cdot}10^{-16}$	$2.00{\cdot}10^{-16}$ (0.08)	1.50	..	..
$^{238}U(n,\gamma)$	$5.99{\cdot}10^{-17}$	$9.66{\cdot}10^{-17}$ (0.05)	1.61	$6.03{\cdot}10^{-17}$	1.01
$^{139}La(n,\gamma)$	$2.61{\cdot}10^{-18}$	$4.70{\cdot}10^{-18}$ (0.11)	1.80	..	..
$^{55}Mn(n,\gamma)$	$2.90{\cdot}10^{-18}$	$5.60{\cdot}10^{-18}$ (0.03)	1.93	$2.37{\cdot}10^{-18}$	0.82
$^{65}Cu(n,\gamma)$	$1.04{\cdot}10^{-18}$	$1.87{\cdot}10^{-18}$ (0.06)	1.80	$1.05{\cdot}10^{-18}$	1.01
$^{115}In(n,n')$	$6.97{\cdot}10^{-20}$	$2.86{\cdot}10^{-19}$ (0.02)	4.10	$7.80{\cdot}10^{-20}$	1.12
$^{58}Ni(n,p)$	$2.43{\cdot}10^{-20}$	$4.01{\cdot}10^{-20}$ (0.03)	1.65	$2.39{\cdot}10^{-20}$	0.98
$^{27}Al(n,\alpha)$	$2.26{\cdot}10^{-22}$	$7.01{\cdot}10^{-23}$ (0.18)	0.30	$5.40{\cdot}10^{-23}$	0.24

Table 2.2 *Results of the foil activation at the phantom position. The values between brackets behind the calculated values are their relative uncertainties. The measured values have an uncertainty of 10%, except for Al (with 30%).*
To shield them from thermal neutrons all foils except for Al, Ni and the first Au have been surrounded by a cadmium box.
For the $In(n,n')$ reaction probably a wrong reaction number has been called in MCNP.
[1)] *Before adjustment, but after correction for factor 1.50.*

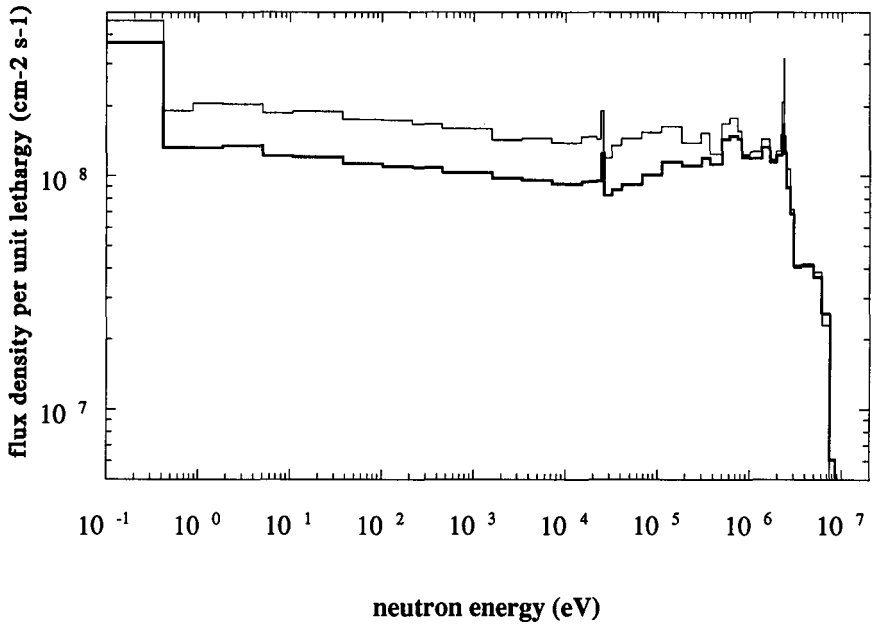

Figure 2.17 *Neutron spectrum inside HN, centered on the first neutron collimator, calculated by MCNP. Here the density of the sand around HN has been modelled higher (1.8 g/cm^3), and the hydrogen fraction has been modelled lower (0.15%).*
For E < 4 MeV the group fluxes calculated by MCNP have uncertainties below 5%.

appears from MCNP that for neutron energies between 1 eV and 0.5 MeV the foil set contributes to the flux for about 6%. This occurs by back scattering of the neutrons in the foil package, thus enlarging the flux. This means that for obtaining a free beam spectrum, the adjusted spectra still should be corrected for this backscattering. In fig. 2.16 both spectra, calculated by MCNP, are shown.

2.8 Optimalisation of test facility HN

An attempt has been made to compute from which part of the reactor the neutrons at the phantom position originated. It appeared that about 67% of those neutrons have made a collision in cell 214 (see fig. 2.12). This means that many neutrons have to travel a long way to the graphite in cell 214 to become scattered into the beam channel. Then the thought rose that it must be possible to increase the neutron flux by reducing the distance from the source to the latest scattering point. This can be done by filling a part of beam channel HN with graphite. Results of some calculations by MCNP of neutron group fluxes are written in table 2.18. In these calculations HN is filled with pieces of graphite from the outer vessel up to positions indicated in fig. 2.3, referred to a power level of 30 kW.

To obtain a maximum epithermal neutron flux, the beam channel has to be filled with graphite up to surface B (x = -40 cm). Then an increase of the total flux of 1.65 is expected. The results of this experiment on the measured gamma spectrum are described in chapter 4.7.

Group fluxes relative to N

energy	N	A	B	C	D	E
< 1 eV	$0.20 \cdot 10^6$	1.22	1.35	1.26	1.15	0.95
1 eV .. 1 keV	$2.32 \cdot 10^6$	1.44	1.48	1.46	1.31	1.15
1 keV .. 0.1 MeV	$1.87 \cdot 10^6$	1.52	1.57	1.55	1.39	1.13
0.1 MeV .. 1 MeV	$1.03 \cdot 10^6$	1.99	2.08	1.90	1.65	1.22
> 1 MeV	$5.17 \cdot 10^5$	1.78	1.91	1.91	1.71	1.39
total	$5.95 \cdot 10^6$	1.58	1.64	1.59	1.42	1.17

Table 2.3 *Increase of group fluxes for HN at the phantom position with reference to N. The beam channel has been filled with graphite to positions A,B,C,D and E. N corresponds to the normal situation, and its column contains absolute group fluxes ($cm^{-2}s^{-1}$).*

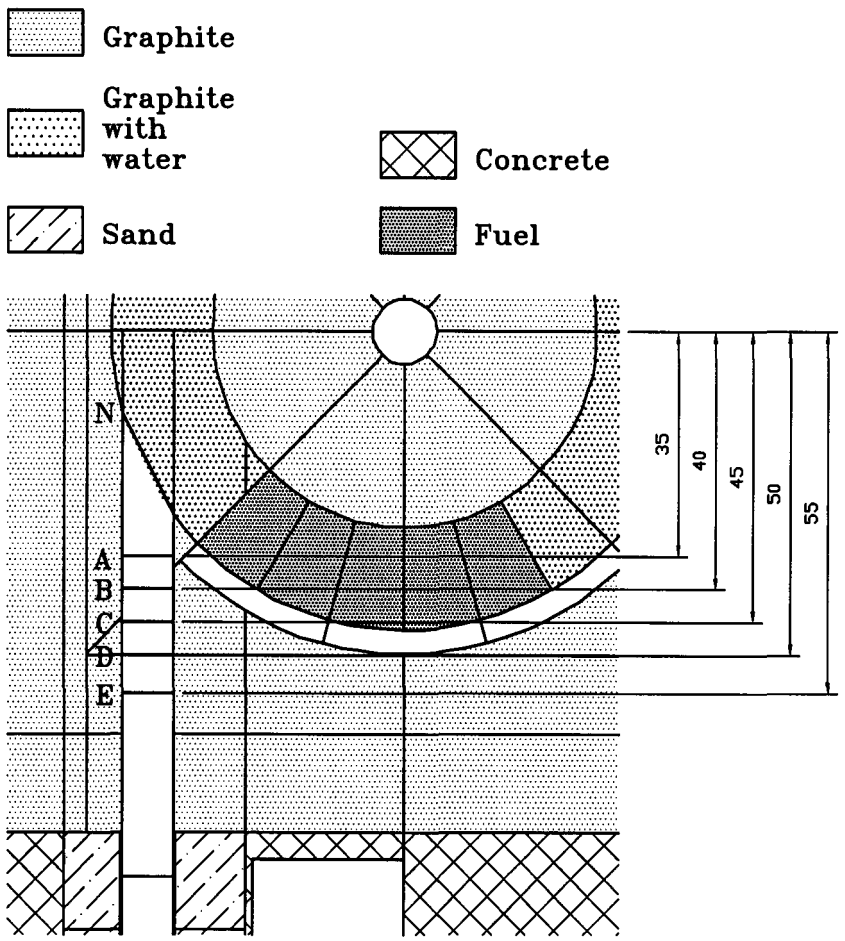

Figure 2.18 *HN filled with graphite up to N,A,B,C,D or E.*

3. HEAD PHANTOM

The neutron beam HN will be used for simulation of the irradiation of the therapy (BNCT) applied on a patient with a brain tumor. In stead of a real human's head a "phantom" head is used. This phantom physically has to look like a patient's head with a tumor positioned a few centimeters below the skull. In a BNCT situation this tumor physically represents a region with a higher boron concentration than the surrounding tissue. The phantom consists of a perspex cylinder (radius of 8 cm, length of 15 cm) at one side combined with a hemisphere and filled with water, eventually with a few ppm's of ^{10}B (see fig. 3.1). This water represents the tissue of brains and blood as the real tissue contains water for about 80% (further some C, Na, Cl, P, Ca, S, etc). In a further stage the water can be replaced by tissue equivalent liquid. The "tumor" of the phantom is a small cylinder (inner radius of 1.07 cm, volume of 7.8 cm^3) of polythene that is filled with water and a fraction of ^{10}B up to 62 ppm for these experiments. By means of some perspex rods (see fig. 3.1) this tumor can be positioned everywhere in the hemisphere. The phantom axes is aligned with the neutron beam axes, and the hemisphere side is irradiated.

To obtain an optimal situation for tumor irradiations, knowledge of the distribution of neutron fluxes is very important. To this purpose neutron transport will again be considered, but now in a much smaller system than a nuclear reactor.

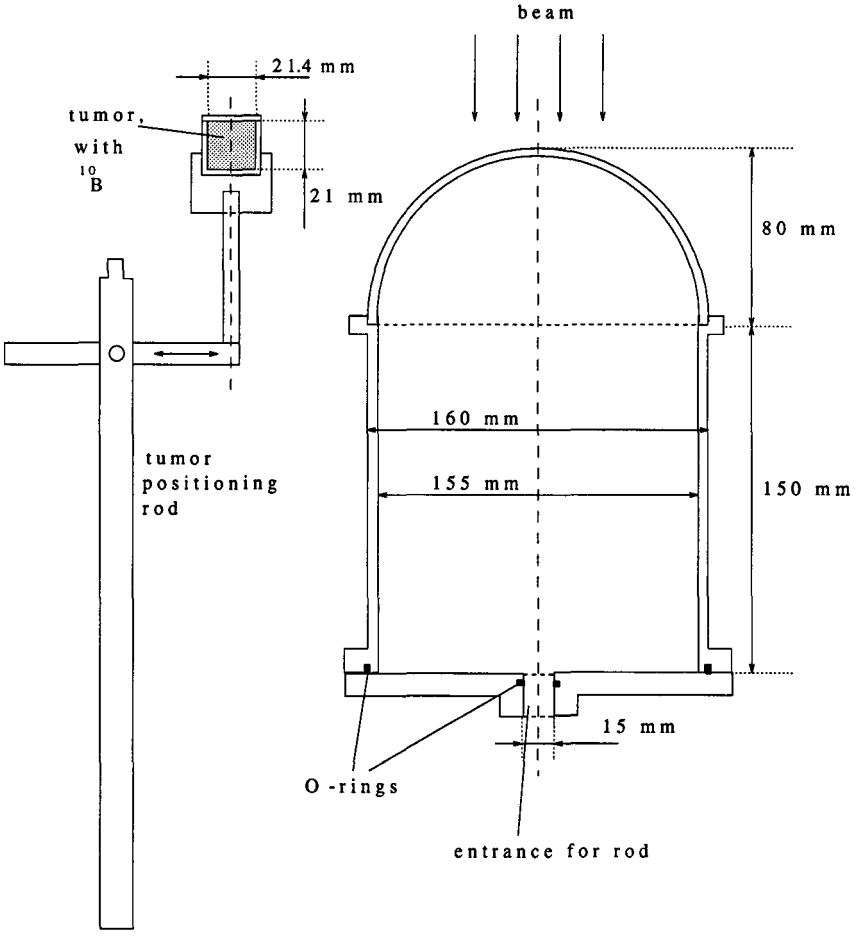

Figure 3.1 *The hemisphere phantom with tumor positioning system.*

3.1 Neutron beam profile

To make sure that the axes of the phantom was aligned well with respect to the axes of the neutron beam, the beam profile has been measured. The expectation was that the beam at phantom position (at 110 cm of the shutter) consists of a circular primary beam of the same diameter as the aperture of the neutron collimators (8 cm), surrounded by a penumbra beam of decreasing intensity, as shown in fig. 3.2.

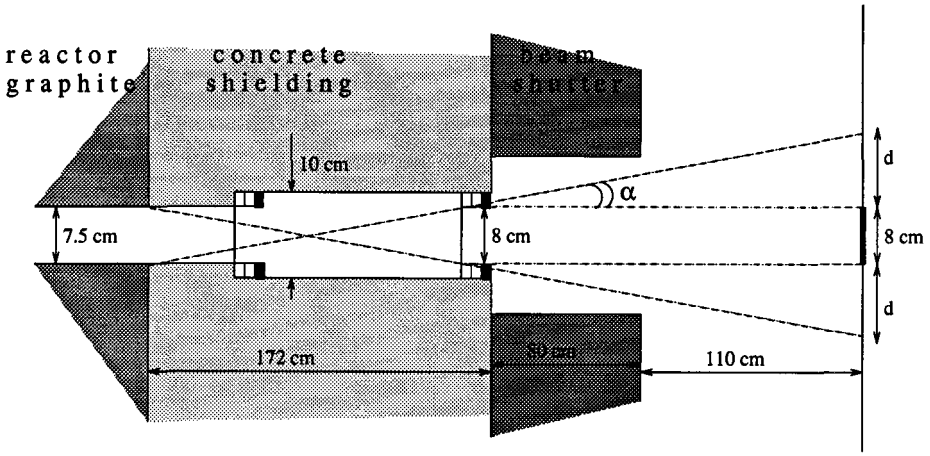

$$\tan\alpha = \frac{7.5 + 0.25}{172} \qquad d = \tan\alpha\,(110 + 80) = 8.6 \text{ cm}.$$

Figure 3.2 *Determination of neutron beam HN. The vertical scale is different of the horizontal scale. At the phantom position the beam consists of a full beam of diameter 8 cm surrounded by a penumbra beam of 8.6 cm.*

The measured beam profile is shown in fig. 3.3. It has been measured by scanning with a BF_3-counter, surrounded by nylon and a sleeve of cadmium outside. The nylon has to slow down epithermal neutrons, and the cadmium has to stop the thermal background neutrons. The shape of the beam profile courses as expected.

3.2 Neutron energy group structure

By discretisation of the energy scale into a certain number of energy groups, the transport equation becomes solvable per group. The group flux ϕ_g for energy group g is defined as

$$\phi_g(\bar{r},t) = \int_{E_g}^{E_{g-1}} \phi(\bar{r},E,t)dE \tag{3.1}$$

and so we get for each energy group a reduced transport equation. In stead of the continuum or point cross sections Σ, group cross sections Σ_g have to be used. These group cross sections are the flux weighted average of the cross sections over one group:

$$\sigma_g = \frac{\int_{E_g}^{E_{g-1}} \sigma(E)\phi(E)dE}{\int_{E_g}^{E_{g-1}} \phi(E)dE} \tag{3.2}$$

where the epithermal flux to weight with is normally the $\frac{1}{E}$ spectrum of fig. 2.5, linked with a Maxwellian flux at the thermal side and a Watt spectrum at the fast

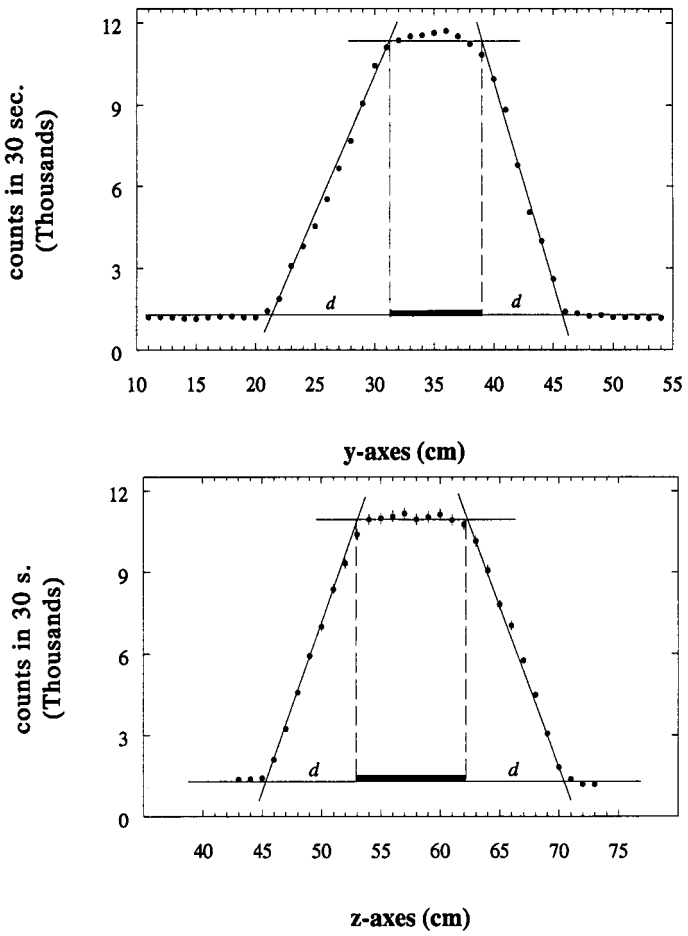

Figure 3.3 *Beam profile of HN, measured with a BF_3 counter. The upper is the horizontal profile and the lower the vertical profile. It consists of a full beam, a penumbra and background.*

side. At resonances in the cross section a further adaption of the weighing is necessary because then the one over E spectrum shows a dip at that energy [4]. By also classifying space into cells and discrete directions, the transport equation turns to a system of linear equations that can be solved numerically.

3.3 Phantom calculations by DORT

DORT is an example of a deterministic code that numerically solves the Boltzmann transport equation by approaching a two-dimensional system with discrete ordinates [10]. DORT makes it possible to determine fluxes of particles by making up the particle balance in all the cells of a system. The particle balance is made up from the different source and sink terms like spatial and energetic in and out scatter, (fission-) sources and absorption, over all directions in a cell. This source can be an external neutron source as well as an internally generated source.

The energy structure (g) of the neutrons and gamma's is chosen conform to the energy structure of the cross section libraries. The geometry is divided into (mostly equally sized) cells in two directions (i, j) and a quadrature set can be chosen for defining the discrete directions (m) in which particles can move. Each of these directions has a weight factor W_m so that $\sum_m W_m = 1$. The directions are indicated by the cosines of angles with the axes. An example of a quadrature set with 48 directions is shown in figure 3.5.

The angular or directional flux (ψ) is the flux through one part of surface area of the discretized sphere and has unity $cm^{-2}s^{-1}$. Then the scalar group fluxes are calculated as

$$\phi_{i,j,g} = \sum_m W_m \psi_{i,j,m,g} \tag{3.3}$$

also with unity $cm^{-2}s^{-1}$. Anisotropic scattering is represented by a Legendre expansion of arbitrary order of the group scatter cross section.

The group transport equations must comply to some boundary conditions. These can be: a boundary source (external neutron source), a reflecting surface (in case of a symmetrical problem) or void. Starting with the highest energy group, DORT will calculate in one inner iteration ψ and ϕ for all the cells and directions for one energy group, so that the transport equations fulfil the boundary conditions and inscattering as good as requested. When this has been done for all energy groups (the first outer iteration), the particle balance is made up again and the second outer iteration starts, with for every energy group new values for the updated directional fluxes. DORT will continue these iterations until the difference in fluxes between two iterations is smaller than a user defined value. At last DORT can calculate the reaction rates of specified isotopes in the cells by summing the product of the neutron fluxes and the macroscopic cross sections for all energy groups.

3.4 DORT input

The DORT code version 1 has been used to perform calculations of neutron transport in the phantom, in this way obtaining neutron and gamma group flux distributions over the phantom. Because of the cylindrical symmetry of the hemispherical phantom, a reflecting left boundary was chosen and the phantom had to be modelled in $R\,Z$ geometry. A mesh size of 0.25 cm was chosen since a mesh size much smaller than the mean free path is not useful. A quadrature set with 96 directions ($S12$ symmetric) has been used. As external boundary source the neutron spectrum calculated with MCNP at phantom position (fig. 2.16) was taken. As the DORT neutron source is defined as a directional flux, the MCNP flux still has to be divided by the sum of the directions in which the neutrons are send in (see equation 3.3). The shape of the neutron source beam has been modelled in conformance with the measured shape in fig. 3.3. The model is shown in fig. 3.4 and for the code input see appendix Appendix B. As the perspex casing of the phantom has almost the same properties as water (for neutrons and photons), it has not been modelled separately. The tumor is defined as a small cylinder on the axes with higher boron concentration.

Next to the group flux distributions, also boron reaction rates are computed. This kind of calculations but merely with thermal neutrons have also been carried out by Matsumoto and Aizawa [11],[12]. To check the calculations of DORT with a measurement, a calibration has been performed. A volume of 7.8 ml filled with a solution of 4 gr. $KMnO_4$ has been irradiated for one hour, while positioned in the phantom at the thermal flux peaking. The Mn is activated by mainly thermal neutrons (see fig. 2.2). After irradiation the activity is measured and can be compared with the activity per atom Mn, as calculated by DORT.

3.5 Results of DORT code

DORT has calculated the distribution of the group fluxes over the phantom. The unadjusted MCNP spectrum has been used as the source spectrum. It is modelled

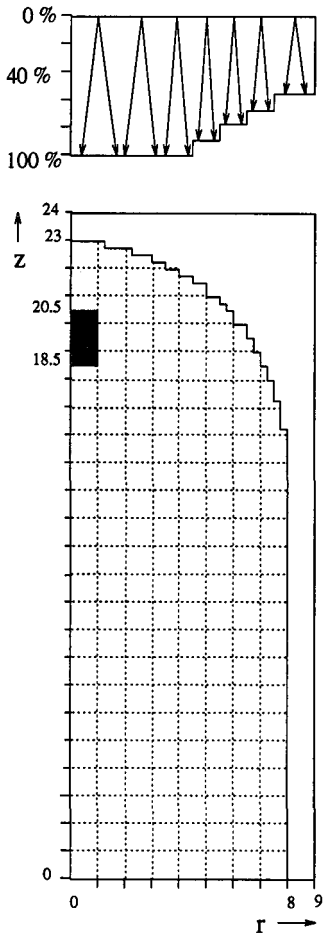

Figure 3.4 *The DORT model of the phantom and the shape of the neutron boundary source.*

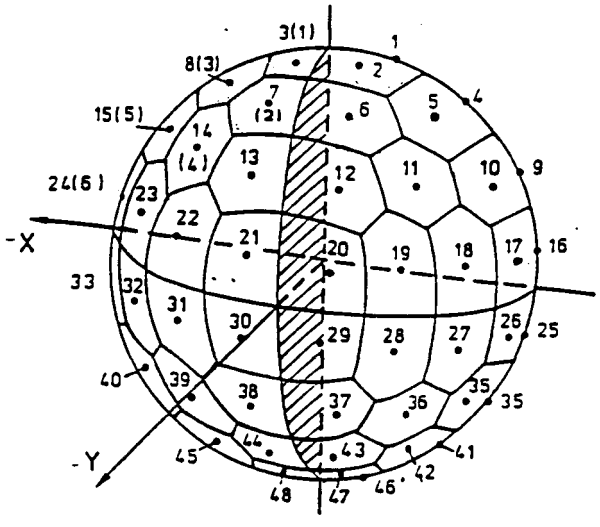

Figure 3.5 *Example of a quadrature set in DORT with 48 directions.*

as a circular beam with radius r = 4 cm, with a shadow beam or halo decreasing to r = 13 cm. As the ^{10}B nuclei have the largest cross section for thermal neutrons, the neutrons of the latest energy group from 0.1 eV to 10^{-5} eV are most important. The distribution of these neutrons is shown in fig. 3.6. Up to 62 ppm ^{10}B only

little significant disturbance over the phantom of the thermal flux occurs. This means that the amount of emitted 478 keV gamma's is proportional to the ^{10}B concentration up to 62 ppm.

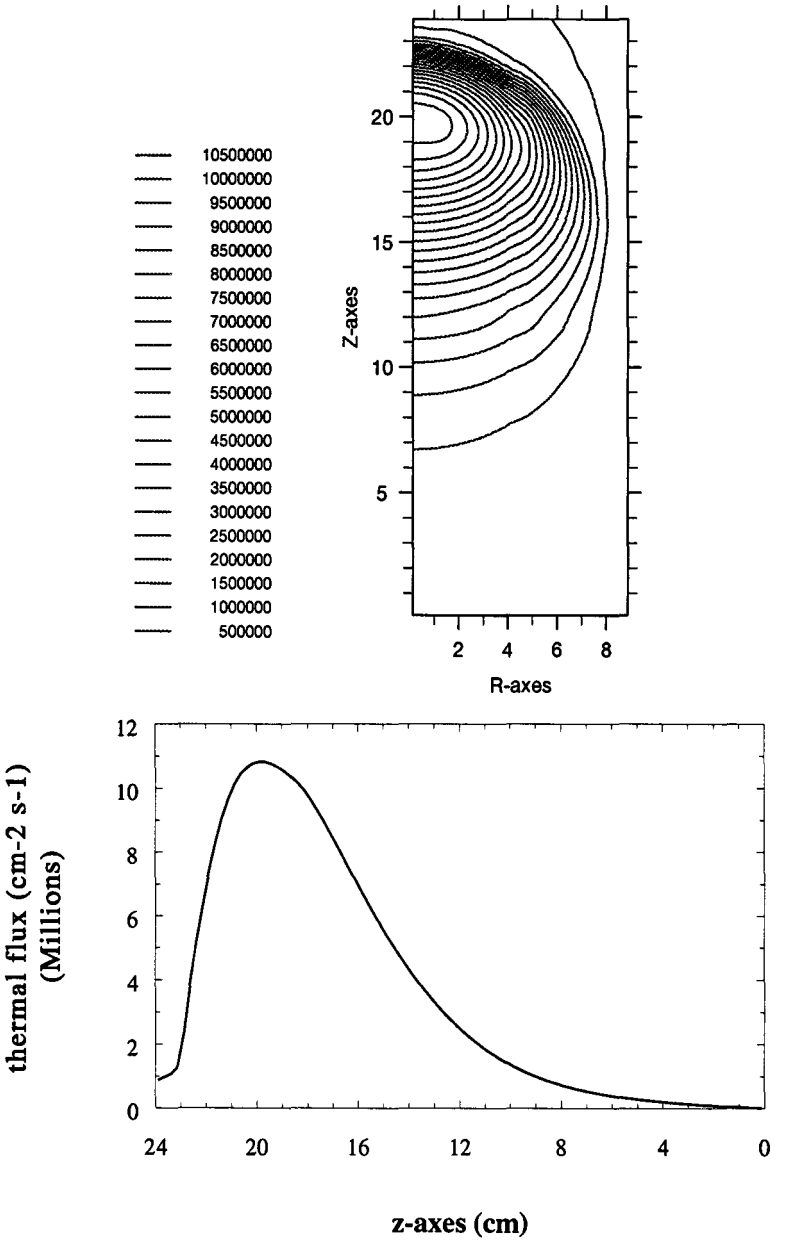

Figure 3.6 *Thermal neutron flux distribution of group 47.*
a. Lines of equal fluxes.
b. Flux distribution at the z-axes.
The front of the phantom corresponds to z = 23 cm, the outer cylindrical boundary corresponds to r = 8 cm.
This picture is cylindrical symmetric around the z-axes.

It can be seen that a thermal flux peaking of 10^7 neutrons/cm^{2}s occurs at 3.5 cm depth from the front of the phantom. This is caused by the moderation inside the phantom of the incoming, epithermal neutrons. The thermal flux gradient is larger in front of the thermal flux peaking than behind it. In figure 3.7 the neutron spectrum at the thermal flux peaking is drawn.

The calibration calculation in which a region of $KMnO_4$ was modelled, predicted

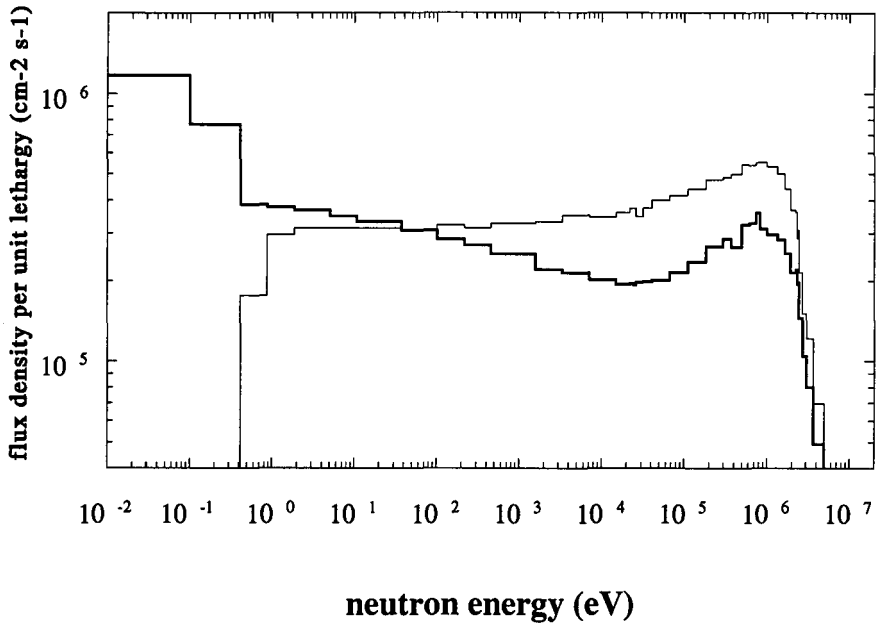

Figure 3.7 *Neutron spectrum inside the phantom at a depth of 3.25 cm (thick line) compared to the neutron spectrum in front of the phantom (thin line).*

a number of neutron absorptions by ^{55}Mn of $1.15 \cdot 10^{-16}$ per sec per atom. The measurements provided a reaction rate of 7.27 ($\pm$ 0.06) 10^{-17} Bq/atom. With these measurements the activity was measured by treating the little cylinder with $KMnO_4$ as a point source at 80 cm of a detector. However, neglecting the self absorption will provide a somewhat too low ($\approx$ 10%) activity and reaction rate. Without this correction it results to a difference of a factor 1.58. This should be noted with the fact that the neutron source, as calculated by MCNP at phantom position had been calculated by a factor 1.5 too high as well.

DORT appears not to be able to calculate photon fluxes in water or air emitted from a point source. As photons scatter only very little in not-dense materials, most of the photons starting in one direction of the quadrature set, will still have the same direction after having travelled 20 cm. This results in star shaped gamma fluxes (see fig. 3.8) because the gamma rays will unsufficiently be scattered into some cells. Even a quadrature set with 210 directions doesn't solve this problem.

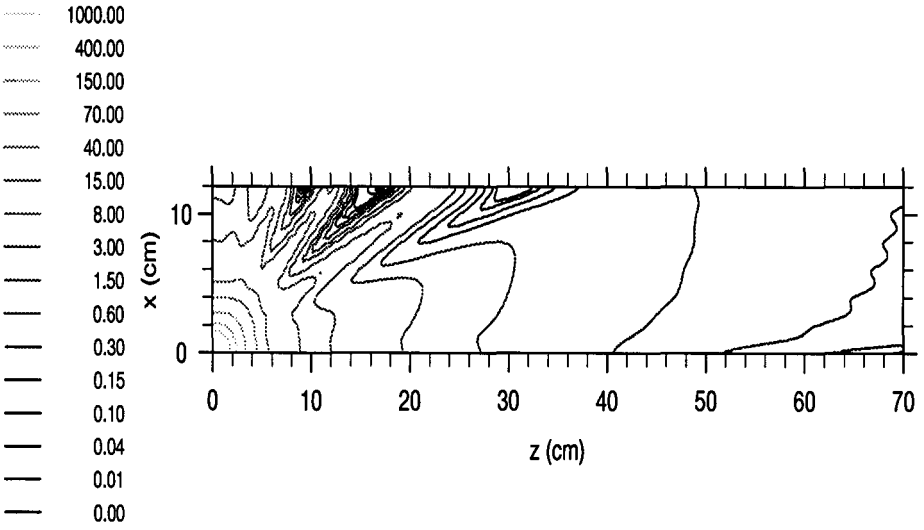

Figure 3.8 *Star effect of DORT. The source is a point source of gamma rays of 500 keV. The total space has been modelled as water. A biassed quadrature set with 210 directions has been used. It is biassed in the positive z direction.*

4. PROMPT GAMMA-RAY SPECTROSCOPY AS A PROBE FOR BORON CONCENTRATIONS

In the previous chapter is shown how a distribution of thermal neutron flux is generated by irradiation with epithermal neutrons. This thermal neutron flux has a local peaking, and will interact with the tissue so that many (n, γ) reactions occur. Also at the reaction of neutrons and boron a prompt gamma-ray of 478 keV is released. Neutron induced gamma radiation can be measured with a detector. As the energy and combination of several emitted gamma-rays is specific for a element, it is possible to analyse the element composition of some irradiated material.

There are two kinds of measurements: activation analysis and prompt gamma spectroscopy. At activation analysis material gets activated at irradiation with neutrons for some time, and later the decay gamma-rays will be measured at some special detector arrangement. At prompt gamma-ray spectroscopy the gamma-rays, emitted during the capture proces, are measured during irradiation with neutrons. Therefore the detector is placed somewhere near the neutron beam. This means that the detector should be shielded for the neutrons as well as for the background gamma-rays. These background gamma-rays are emitted by the specimen, by the shielding material (for example the neutron beam stop, the shielding concrete of the irradiation facility, etc.), and by the nuclear reactor itself. Next to the prompt gamma-rays, also the decay gamma-rays as a result of activation are detected. This means that there is a very large background of radiation and the shielding of the detector is very important.

4.1 Interaction of electromagnetic radiation with matter

Electromagnetic radiation like gamma-rays have mainly three ways to interact with matter: photoelectric absorption, pair production and the Compton scattering.

1. At photoelectric absorption the total gamma-ray energy is absorbed and converted into kinetic energy of a free electron. This electron loses its energy by ionisation of other atoms. This proces only occurs for low energetic gamma-rays ($E < 0.5$ MeV).
2. At pair production the gamma-ray energy is converted into an electron and positron pair (each having rest masses of 511 keV) and the rest is converted to kinetic energy of these particles. This means that pair production can only occur for gamma-rays with energies higher than 1.1 MeV. The created positron exists for a short time, it will soon annihilate with an electron and two 511 keV gamma-rays will be emitted.
3. The Compton effect is the scattering of a gamma-ray by an electron. The gamma, with energy E_γ, loses part of his energy that is transferred to kinetic energy of the electron.

The gamma-ray energy after Compton scattering ($E_{\gamma'}$) depends on the scattering angle θ and is given by

$$E_{\gamma'} = \frac{E_\gamma}{\left(1 + \frac{E_\gamma}{mc^2}\right)(1 - \cos\theta)}. \tag{4.1}$$

The kinetic energy of the electron is

$$T_e = E_\gamma - E_{\gamma'}. \tag{4.2}$$

The factor mc^2 is the relativistic rest energy of a free electron, 511 keV. The probability function for Compton scattering at an angle θ is described by the Klein-Nishina formula [13]

$$\frac{d\sigma_c}{d\Omega} = r_0^2 \left[\frac{1}{1+\alpha(1-\cos\theta)}\right]^3 \left[\frac{1+\cos\theta}{2}\right] \cdot \left[1 + \frac{\alpha^2(1-\cos\theta)^2}{(1+\cos^2\theta)(1+\alpha(1-\cos\theta))}\right]. \quad (4.3)$$

This is the differential cross section per electron in the scatterer, with $\alpha = \frac{E_\gamma}{mc^2}$, and r_0 = 2.818 fm. A polar plot of this cross section is shown in fig. 4.1. The macroscopic differential Compton cross section is obtained by multiplying with the number of electrons per atom (Z) and the number of atoms per unit volume (N):

$$\frac{d\Sigma_c}{d\Omega} = \frac{d\sigma_c}{d\Omega} ZN. \quad (4.4)$$

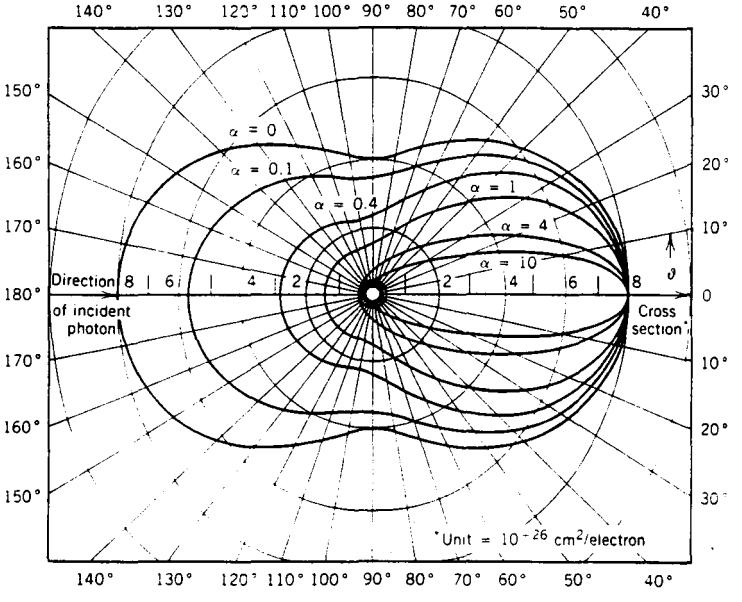

Figure 4.1 *The Compton scattering cross section for various incident energies. From R.D.Evans, The atomic Nucleus (New York: McGraw-Hill, 1955)*

4.2 Germanium detectors

4.2.1 Peak formation

Detection of gamma-rays and determination of their energies is possible with a high purity germanium detector. This belongs to the semiconductor detector type. Entering gamma-rays create photo- and/or Compton-electrons leaving electron-hole pairs. Under the influence of an electric field the electrons can be collected, giving rise to an electronic pulse whose amplitude is proportional to the energy of the photon. As the required amount of energy to create one electron-hole pair (ϵ) or the band- gap is very small (about 3 eV) the number of created charge carriers is accordingly high. Their number will be distributed around the mean number of created carriers by a gamma-ray of energy E, according to the Gaussian

distribution with relative standard deviation

$$\sigma_{rel} = \frac{\sqrt{\frac{FE}{\epsilon}}}{\frac{E}{\epsilon}}. \tag{4.5}$$

F Is the Fano factor ($0 < F < 1$, mostly around 0.12), depending e.g. on the size of the crystal [14]. For a good charge collection there should be very few free electrons and/or holes in the crystal itself. This can be done by using a very pure and perfect crystal, and cooling it down to liquid nitrogen temperature (therefore enlarging the band-gap).

The electric pulse of the germanium crystal is amplified by a preamplifier and an amplifier to a pulse which is scaled by a multichannel analyzer. The detected peak of gamma-rays of energy $\bar{E}$ can be described by

$$f(E) = \frac{A}{2\pi\sigma} e^{\frac{-(E-\bar{E})^2}{2\sigma^2}} \tag{4.6}$$

with $\sigma = \sigma_{rel}E$ and A is the area beneath the peak. The Full Width Half Maximum ($FWHM$) is a measure of the resolution and is determined by

$$FWHM = 2\sigma\sqrt{2\ln 2} \tag{4.7}$$

If gamma-rays enter a detector they can be Compton scattered in the crystal. If the scattered gamma-rays escape from the crystal, only the energy of the free electrons will be measured, resulting in a Compton continuum from 0 keV ($\theta = 0°$) to $T_e(\theta = 180°)$. If gamma-rays scatter outside the crystal (in shielding material) there is also a small background due to detection of scattered gamma-rays. The Compton effect of high energy gamma-rays in the detector is mostly the main cause of background in a measured gamma-ray spectrum.

4.2.2 Efficiency

The efficiency of a detector (ϵ) is defined by

$$\epsilon(E) = \epsilon_{det}(E)\epsilon_{geom} \tag{4.8}$$

with $\epsilon_{det}(E) = \frac{\text{number of gamma-rays in a gamma line of energy } E}{\text{number of gamma-rays of energy } E \text{ falling on the crystal}}$

and

$$\epsilon_{geom} = \frac{\text{area of the detector crystal}}{4\pi R^2}$$

where

R = distance of gamma source to surface of surface of the detector.

The efficiency decreases almost exponentially for energies larger than about 200 keV, depending on the dimensions of the crystal. For determination of ϵ_{geom} see also chapter 4.8.

4.2.3 Neutron Damage

The resolution of a detector deteriorates if the crystal contains impurities (normally smaller than 3.10^{10} atoms/cm^3) or lattice imperfections. These impurities, and possible lattice imperfections, are called trapping centres because they can "trap" the electrons or holes for some time. If the time for release of the trapped carriers is larger than the pulse shaping time, those carriers cannot contribute to the detection

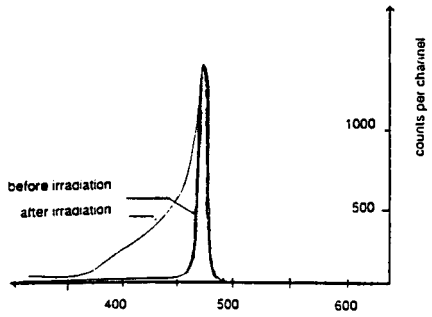

Figure 4.2 *Low energy tail in a gamma-ray spectrum (1.33 MeV), caused by lattice neutron damage [15]*

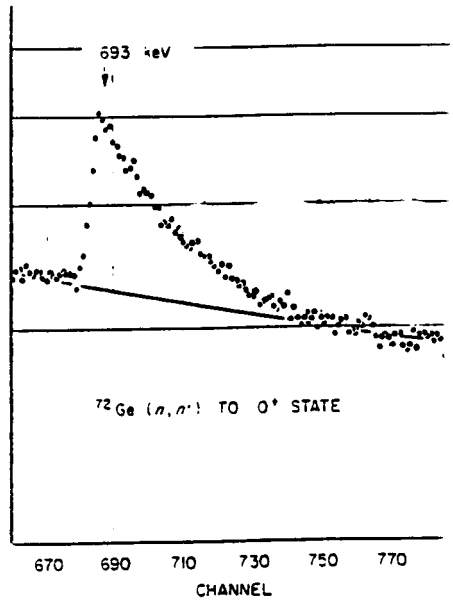

Figure 4.3 *The 691 keV line of germanium, with an high energy tail [16].*

of the total gamma energy. This results into an incomplete electronic pulse [14]. In the spectrum this will be seen as a "low energy tail" of a peak as shown in fig. 4.2.

Germanium detectors can be damaged by fast neutrons and charged particles as protons. Fast neutrons may produce vacancies by knocking atoms out of the lattice. These defects act as hole traps. This effect becomes obvious at irradiations of more than 5.10^7 n/cm^2 [16] [17].

If a detector is irradiated by thermal neutrons, several peaks can be seen due to the Ge(n, γ) reaction. The most powerful peak occurs at 596 keV and has a normal width. At irradiation by fast neutrons several broadened peaks occur, now also due to Ge$(n, n'\gamma)$ reactions. At 596 keV and 834 keV there will be gamma lines that are broadened by the recoil of the Ge nucleus. The line at 691 keV is caused by excitation of the 0^+ state in ^{72}Ge by inelastic neutron scattering to another 0^+ state. This 0^+ 0^+ transition only occurs by electron emission, resulting in a high efficiency of detection. This line, shown in fig. 4.3 has a high energy tail also due to recoil. These broadened lines can act as a measure for fast neutrons.

It is possible to reduce the number of thermal neutrons at the detector by shielding with materials of a large cross section for thermal neutrons. Examples are boron, lithium and cadmium [1], but cadmium is an emitter of high energy gamma-rays at neutron capture, therefore it deteriorates the peak background ratio by these unwanted gamma-rays.

4.3 Detector collimation and shielding

The first purpose is to measure the boron gamma-rays from the phantom and to improve the peak background ratio around 478 keV. The phantom (fig.3.1) is cylindrical, with a hemisphere at the front, and is made of perspex. It can be

[1] Not boron if boron is the element to be detected

filled with water, representing the human tissue (possibly later tissue equivalent liquid can be used). The "tumor" is a small polythene cylinder (diameter $\approx$ 2 cm, length $\approx$ 2.2 cm), filled with water and a concentration of 62 $\pm$ 2 ppm ^{10}B [2]. This "tumor" can be positioned anywhere in the phantom by means of a perspex bar.

Because of the large amount of water a very important reaction is ^{1}H(n,γ)^{2}H with σ_{therm} = 0.33 b, emitting a prompt gamma-ray of 2223.3 keV. In spite of the low cross section compared to ^{10}B, much more hydrogen gamma-rays are emitted than ^{10}B gamma-rays. It are these gamma-rays that should be shielded of the detector mainly. Further there will be a large gamma-ray background with energies beneath 511 keV due to gamma-rays coming from the reactor, being Compton scattered in the phantom with $\theta = 90°$ to the detector.

There has been chosen for a kind of "telescope" detector collimator. The detector placed at a large distance (133 cm) of the phantom, seeing only a small part of the target by means of a set of collimators. The idea behind this is that there are two kind of background sources:

1. the phantom itself,
2. the shielding walls and polythene.

The $\frac{1}{r^2}$ law has most influence on the sources nearest to the detector. Therefore by enlarging the distance to the phantom, the decrease in background produced by the shielding is larger than the decrease of the tumor count rate.

The ultimate detector collimation and shielding is drawn in fig. 4.4. It particularly consists of one 5 cm thick lead collimator (aperture = 4.5 cm) just in front of the detector and a circular aperture (1.5 cm) in the lead shielding of the wall at a distance of 40 cm of the centreline of the phantom. This lead shielding of the wall is made of several lead bricks that can be shifted so that a range of 15 cm parallel to the beam axes can be achieved. Moreover the detector itself has been shielded by a steel cover (against low energetic X-rays) and 5 cm of lead. As it is placed on a moveable frame the detector can be shifted too. The inside polythene wall has a slit formed aperture in front of the first lead collimator. To shield the detector from neutrons a 1 cm thick lithiumpolythene slab is placed in front of it.

[2] According to concentration measurements by prompt gamma analysis at the HFR

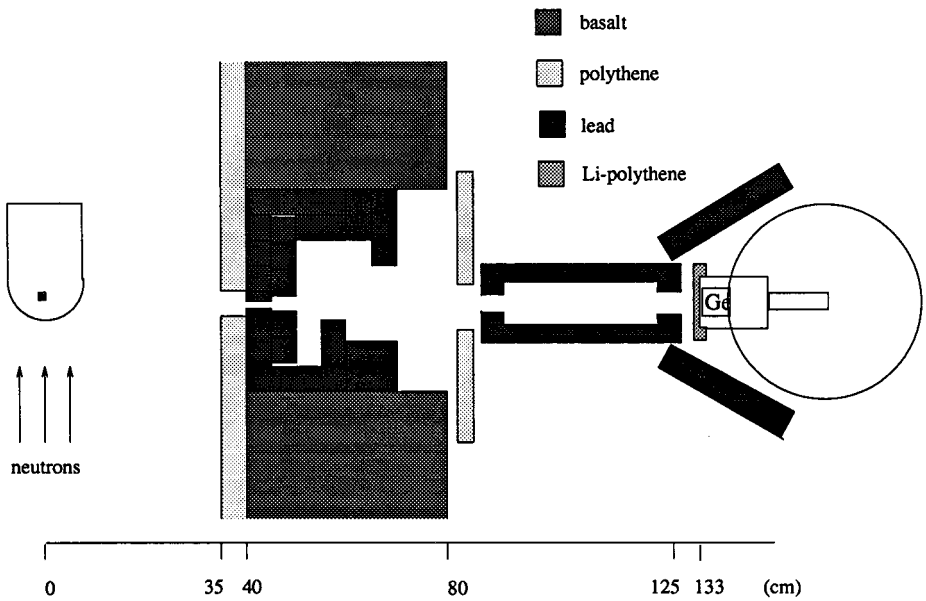

Figure 4.4 *Shielding and collimation of the HPGe detector.*

4.4 The $^{10}B(n,\alpha)^{7}Li$ reaction

One of the main reasons of the use of boron in BNCT is the very high cross section for thermal neutrons (for v = 2200 m/s) of σ = 3837 barn. This cross section decreases by one over v (fig. 4.5) hence mainly thermal neutrons give raise to this reaction. As a result of neutron capture a $^{11}B^*$ compound nucleus is created that immediatly decays by emission of a α-particle of energy either 1.48 MeV or 1.79 MeV. The cross section for the reaction $^{10}B(n,\gamma)^{11}B$ is 0.5 barn.

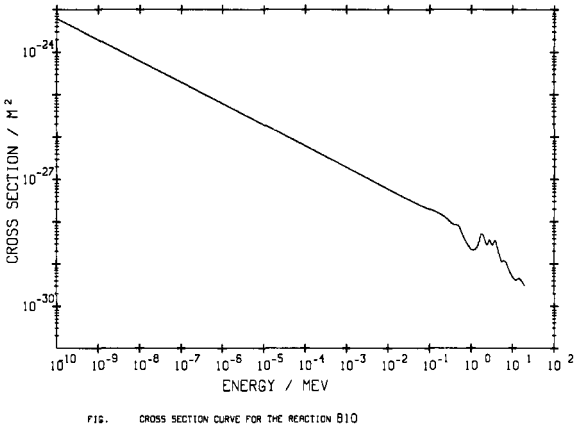

FIG. CROSS SECTION CURVE FOR THE REACTION B10

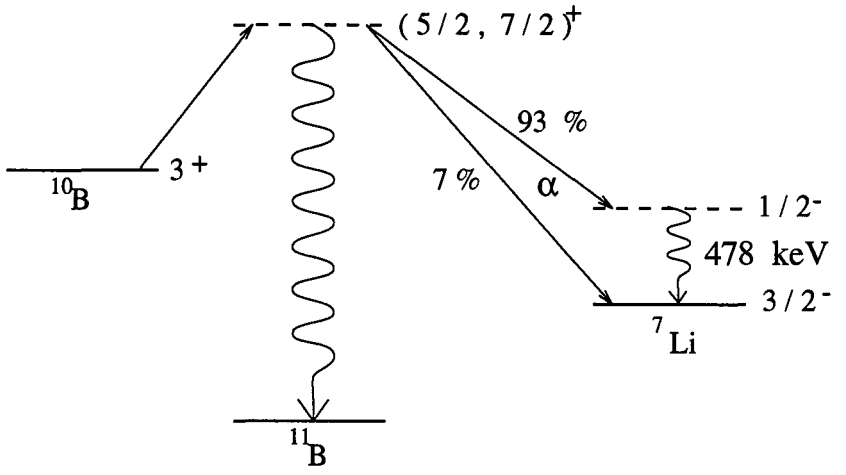

Figure 4.5 *Neutron absorption cross section of ^{10}B and the reaction scheme of $^{10}B(n,\alpha)^{7}Li^*$.*

By means of a neutron moderator like water the neutrons can be scattered and the thermal capture neutrons will have isotropic directions so that the directions of the $^{7}Li^*$ fragments are also isotropically distributed [20]. The basic principles of BNCT are based on the high initial energy of the He and Li fragments: respectively 1.473 MeV and 841 keV (93%). They have enough energy to destroy a cell nucleus. Next to this, the excited $^{7}Li^*$ nucleus will de-excite with time constant τ = 102 fs [20] to its ground state by emission of a gamma-ray with E_γ = 478 keV.

4.5 478 keV Gamma-ray line shape reconstruction

Those gamma-rays have an isotropic angular distribution in the center of mass system (c.m.) of the $^{7}Li^*$ nuclei. Considering a number of N excited $^{7}Li^*$

projectiles then

$$\frac{dN}{d\Omega_{c.m.}} = \frac{N}{4\pi} \text{ or } \frac{dN}{d(\cos\theta_{c.m.})} = -\frac{N}{2} \tag{4.9}$$

Because of the very short lifetime mostly the gamma-ray is emitted during the slowing down of the Li-nucleus that has a momentary velocity v. An observer in the laboratory system observes a gamma-ray with a Doppler shifted energy [21]

$$E_{\gamma'} = E_{\gamma 0}\frac{\sqrt{1-\beta^2}}{1-\beta\cos\theta}. \tag{4.10}$$

In this expression $\beta = \frac{v}{c}$, and θ is the angle between the initial velocity vector of the moving Li nucleus and the direction of motion of the emitted γ-quant in the laboratory system. This can be related to the angle in the center of mass system (see fig. 4.6).

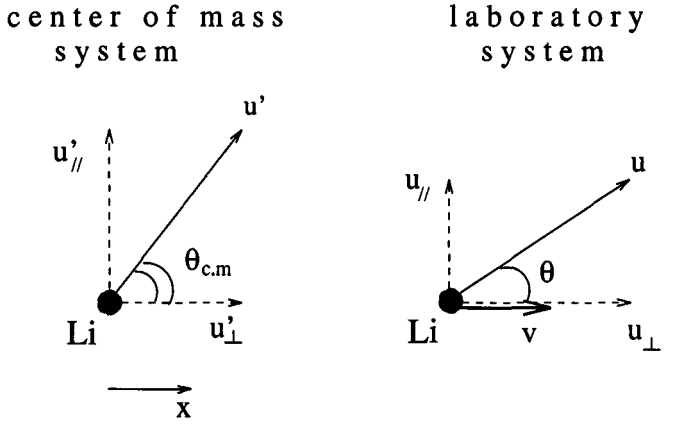

Figure 4.6 *Center of mass system, laboratory system.*

Consider a center of mass system moving with velocity v according to the laboratory system in the positive x direction, emitting a γ-quantum in the center of mass system with velocity u', at an angle $\theta_{c.m.}$ with the x-axes. In the laboratory system the velocities parallel and perpendicular to v, are given by [22]

$$u_{\parallel} = \frac{u'_{\parallel} + v}{1 + \frac{\vec{v}.\vec{u}'}{c^2}} \tag{4.11}$$

and

$$u_{\perp} = \frac{u'_{\perp}}{\gamma_v\left(1 + \frac{\vec{v}.\vec{u}'}{c^2}\right)} \tag{4.12}$$

with

$$\gamma_v = \frac{1}{\sqrt{1-\frac{v^2}{c^2}}}. \tag{4.13}$$

The angle of u with the x-axes in the laboratory system is defined by

$$\tan\theta = \frac{u_{\perp}}{u_{\parallel}}. \tag{4.14}$$

The relation between θ and $\theta_{c.m.}$ can be computed as

$$\cos\theta = \frac{\cos\theta_{c.m.} + \beta}{1 + \beta\cos\theta_{c.m.}}. \tag{4.15}$$

Now the number n of gamma quanta seen by a solid detector in the laboratory system within an energy interval $(E, E + dE)$ is

$$n = \frac{dN}{dE} = \frac{dN}{d(\cos\theta_{c.m.})} \frac{d(\cos\theta_{c.m.})}{d(\cos\theta)} \frac{d(\cos\theta)}{dE}. \tag{4.16}$$

Using formulas 4.9, 4.10 and 4.15 n can be computed as

$$n = \frac{N}{2} \frac{\sqrt{1-\beta^2}}{\beta} \tag{4.17}$$

which is independent of θ. Suppose we have a large number of de-exciting ^{7}Li* projectiles that move in a vacuum (this means that they are not subject to a stopping power, and $v = 4.8.10^6$ m/s = constant), the line shape of the boron peak for an ideal detector response is a rectangle between (in first order treatment of $E_{\gamma'}$) $E^- = E_0(1-\beta)$ and $E^+ = E_0(1+\beta)$. However, normally the recoiling projectile is slowed down by the surrounding material and its momentary velocity will be $v = v(t)$. The number of nuclei de-exciting between t_1 and t_2 after creation of ^{7}Li* is given by

$$N_1 - N_2 = N_0 \left(e^{\frac{-t_1}{\tau}} - e^{\frac{-t_2}{\tau}} \right). \tag{4.18}$$

The continuous decrease of the velocity in time, depending on the stopping power $\frac{dE}{dx(v)}$, can be used to obtain the stopping power for ^{7}Li in several materials as function of the velocity [20] [19] [18]. For this a measured boron line shape is divided into several rectangles with width (in first order) of $\frac{2 \cdot v(t)}{c \cdot 478\ keV}$ and height according to eq. 4.18 (for a specific time interval), see fig 4.7. This height is a measure of the stopping power.

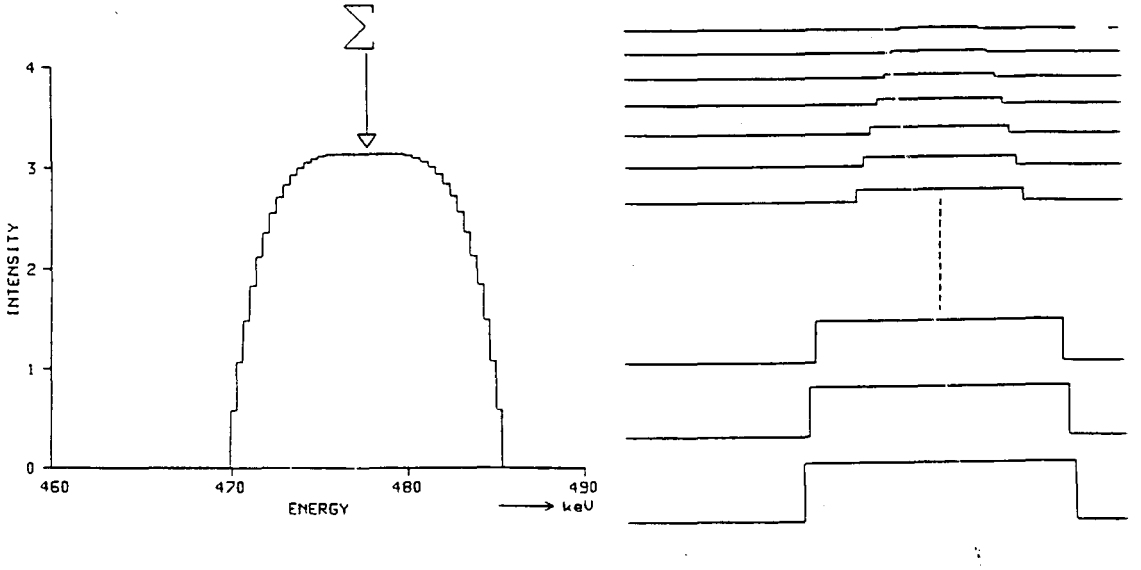

Figure 4.7 *Boron line shape constructed with rectangles.*

An other possibility is to calculate the expected boron line shape in a medium when $\frac{dE}{dx}$ is known. This has been done for boron in water, using stopping power data of TRIM [23] (fig. 4.8, fig. 4.9). According to Neuwirth et al. this peak can be described by

$$N(\Delta E) = c\left(1 - \left|\frac{\Delta E}{\Delta E_0}\right|^q\right) \quad \text{for} \quad -\Delta E_0 < \Delta E < \Delta E_0,$$
$$N(\Delta E) = 0 \ \text{ else}, \tag{4.19}$$

with ΔE = maximal energy increase as a result of the Doppler shift by $v(t)$,
$\Delta E_0 = \frac{v(0)}{c} E_\gamma$ = 7.648 keV = maximum energy increase at t=0,
q = factor depending on the stopping power,
c = normalisation factor (= $\frac{q+1}{q \cdot \Delta E_0}$ · total number of counts in ^{10}B peak.)

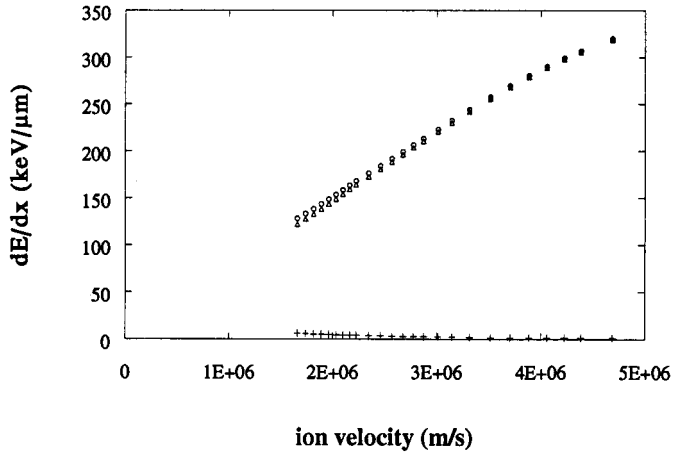

Figure 4.8 *Stopping power for Li in water against velocity, calculated with TRIM. The ∘ represents the total stopping power, △ the electron stopping power and + the nuclear stopping power.*

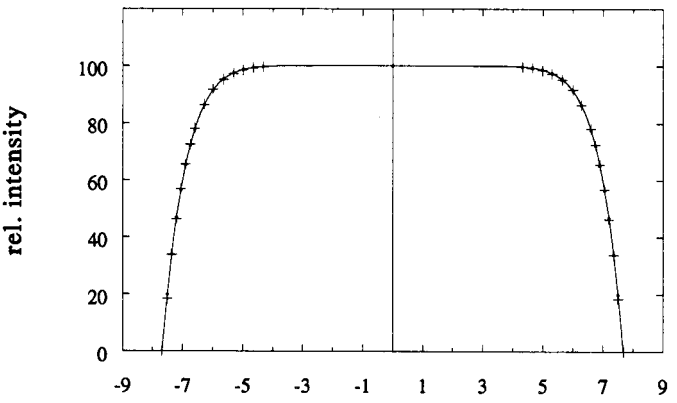

Figure 4.9 *Ideal boron line shape in water, constructed using the stopping power calculated by TRIM (+). The drawn line is fitted according to equation 4.19.*

By use of a curve fitting program the factor q is determined to be 9.9 in water. To describe the ^{10}B line as measured by a normal Ge detector, this function still has to be folded with the detector response function. For N mono-energetic gamma-rays with energy A being detected in the peak, this response function is

$$F(E) = \frac{N}{\sigma\sqrt{2\pi}} e^{-\frac{(E-A)^2}{2\sigma^2}} \tag{4.20}$$

with σ as the width of the γ-peak. For boron the resulting gamma peak as measured by a Ge detector can be described by

$$D(\Delta E) = \int_{-\infty}^{\infty} F(\Delta E) N(A) dA. \tag{4.21}$$

With $\sigma \approx 0.60$ keV for gamma-rays of 478 keV this will result to a curve as shown in fig. 4.10.

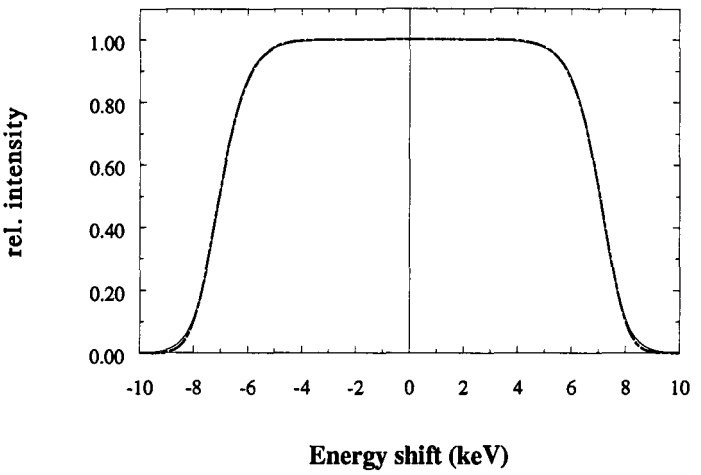

Figure 4.10 *Boron peak as detected by Ge-detector. The solid line is constructed according to equation 4.21. The dashed line represents the reconstruction by fitting with eq. 4.22.*

It is not possible to give an exact analytical description of this peak, but we can approximate it by the function

$$B(E) = \frac{N}{13.95} \frac{1}{1 + e^{\frac{(E-478)^2 - a1^2}{a2}}} \tag{4.22}$$

with for the best fit parameters of $a1 = 6.91$ keV and $a2 = 6.7$ keV. The difference in area under the curve is less than 0.5% (see fig. 4.10).

4.6 Measurements

Gamma-ray spectra were measured with an Oxford HPGe detector, type CNHDS30-10190. The pulse height was amplified with an ORTEC 672 amplifier with shaping a time of 2 μsec and analysed with a multichannel analyser with 4096 channels. The amplification was adjusted such that the maximum measurable gamma energy was about 2.5 MeV.

By trial and error the detector collimation and shielding has been optimized. This optimization implies that was sought for a as high as possible peak/background relation for the boron peak. The center of the "tumor" with boron was positioned at 2.5 cm from the front of the phantom. A laserpen alignment configuration has been designed to be able to align the middle of the detector crystal to a position at the middle surface of the phantom. Further the necessity to shield the detector from neutrons has been investigated.

After the best collimator configuration was found, some tomography measurements were performed. For this, the phantom was filled with tap water with 5.1 ppm ^{10}B added. The "tumor" was the same as before with 62 ppm ^{10}B, now positioned asymmetric, with axes at 3 cm of the phantom axes, located at a depth of 3.5 cm. The overall concentration was added because in a situation with a real patient, injected with a boron compound, the not-tumor tissue also has a boron concentration of about one tenth of the tumor concentration.

By starting at one position of the "tumor" in the phantom, and after each measurement of 20 minutes turning the perspex bar with the "tumor" for 15°, a radial scan has been performed. It resulted into 24 "projections" of boron concentration of tumor and background of the space seen by the detector. One of these boron lines with a curve fitted according to eq. 4.22 can be seen in fig. 4.11. The values of the χ^2 tests for the 24 curves were lying between 0.86 and 1.9 (mostly around 1.3). For two spectra that have been measured for 120 minutes, the χ^2 tests resulted in values of 3.1. These higher values may be caused by the better statistics which made the Cu-line of 466 keV more significant. More details about the tomography will be given in chapter 4.9.

4.7 The boron line in the gamma-ray spectrum

With the detector collimation and shielding configuration described in chapter 4.3 the largest peak/background relation has been obtained. This background mainly originates from Compton scattered H-gamma-rays of 2223.3 keV. The used collimation configuration is also suitable for space dependent boron measurements and tomography. A typical measured gamma-ray spectrum is shown in fig. 4.12. In this situation a "tumor" with 62 ppm ^{10}B is placed on the phantom axes at a depth from 1.5 to 3.7 cm. The water in the phantom doesn't contain any boron. The detector is adjusted on 2.5 cm depth. No polythene neutron shielding is present between the phantom and the detector.

A boron count rate of 2.98 counts/sec ($\pm$ 1%) was obtained. The peak/background relation was 0.64 and the ^{10}B/H relation was 0.23. To determine the ^{10}B counts within 7%, at least a counting time of 30 minutes is required. Next to ^{10}B, obvious gamma lines are: H, single escape of H (1712.3 keV), double escape of H (1201.3 keV), 511 keV, Co (1173 keV and 1333 keV) from the background, and many Ge lines (e.g. 596 keV, 834 keV, 500 keV, 493 keV). As these Ge lines are not obvious broadened, detector damage by high energy neutrons is not to be

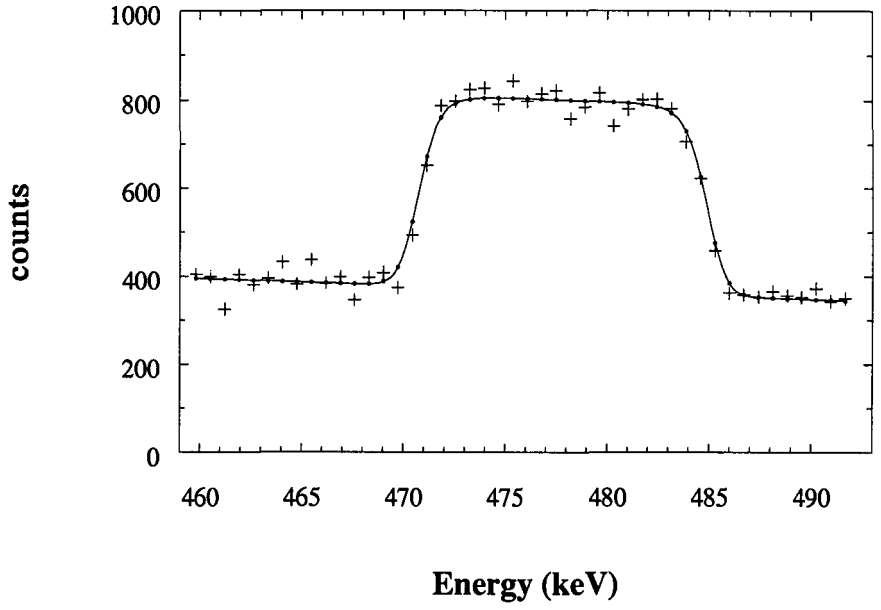

Figure 4.11 *Boron line of tomography measurement 17, measured for 20 minutes, and the fitting according to eq. 4.22.*

expected.

In the range of 0 to 8 MeV no distinct lead gamma-rays are visible. The large increase of background at low energy (< 511 keV) is due to gamma-rays in the beam coming from fission products of the reactor. They have been scattered under 90° to the detector. Also the triangle shaped peak at 417 keV originates from the reactor. These are hydrogen gamma-rays (2223.3 keV) scattered between 88.1° and 91.9° to the detector. The resulting gamma-ray energy can be calculated with formula 4.1. It will be between 404 keV and 427 keV.

After filling a part of beam channel HN with graphite (see chapter 2.8) the total count rate increased. The ^{10}B and H count rate increased with a factor 1.79, while the background and 511 keV count rate only increased with a factor 1.59. This may be due to the fact that the gamma-rays from the reactor are shielded by about 15 cm of graphite now. This improve of the irradiation facility makes it possible to reduce the counting time of a spectrum to only 20 minutes.

4.8 Detector geometric efficiency

Consider the detector, partly shielded of the source by means of some collimators, while the source cannot be assumed as a point source (see fig.4.13). In this case the geometric efficiency (see also chapter 4.2.2) becomes space dependent. Now $\epsilon_{geom}(x, y, z)$ can be determined by calculating the area of the detector seen at position (x, y, z) for every point source position. In case of circular apertures of the collimator there is cylindrical symmetry $(x, y, z) \rightarrow (r, y)$.

By projection of the first collimator on the detector it becomes a circle of radius a, with $a = \frac{r_1 \cdot y}{d}$. The centre of the circle moves from s to $-s$ if one moves at source position from $-x$ to x and $s = \frac{y-d}{d} \cdot x$ (see fig. 4.14). The surface in common of the two circles is the area of the detector seen from source position (x, y, z). This

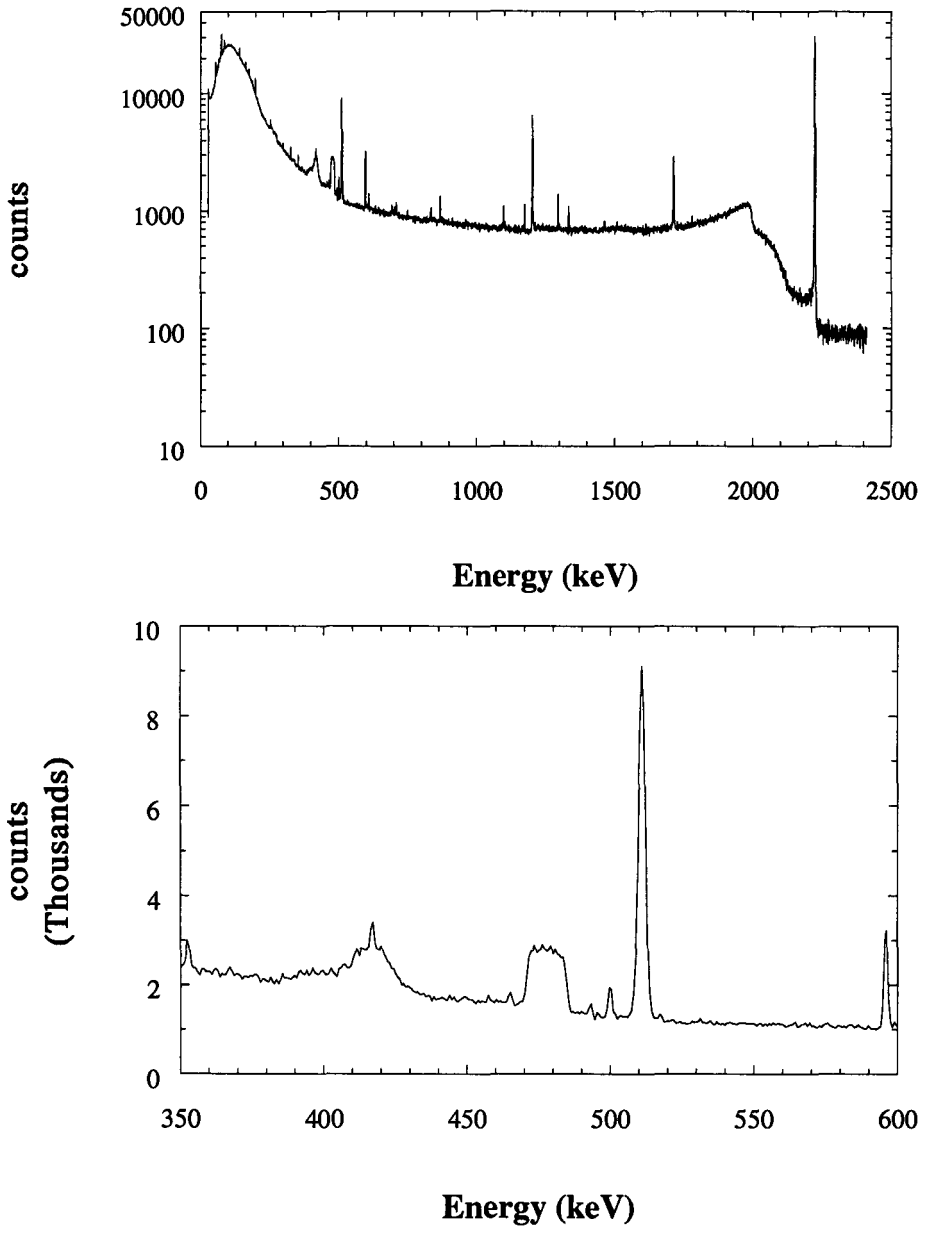

Figure 4.12 *Measured gamma-ray spectrum of a neutron irradiated phantom filled with water and a region of 7.8 ml 62 ppm ^{10}B. Measuring time was 140 minutes.*
a. Logarithmic vertical scale
b. Linear vertical scale, reproduced on a larger energy scale.

area can be computed as

$$S = a^2 \arccos(\frac{p}{a}) + r_2^2 \arccos(\frac{s-p}{r_2}) - s\sqrt{a^2 - p^2} \qquad (4.23)$$

with p = x-coordinate of the intersection between the two circles,
p = $\frac{a^2+s^2-r_2^2}{2s}$.

In this practical situation, the phantom is the gamma source. The distance between the detector and the centreline of the phantom is y = 133 cm. The two collimators are made of 5 cm thick lead with circular apertures of r_2 = 2.15 cm and r_1 = 0.75 cm. The distance d from the centreline of the phantom to the front of the second collimator is 40 cm. The x dependency (or z, because of circular symmetry) on

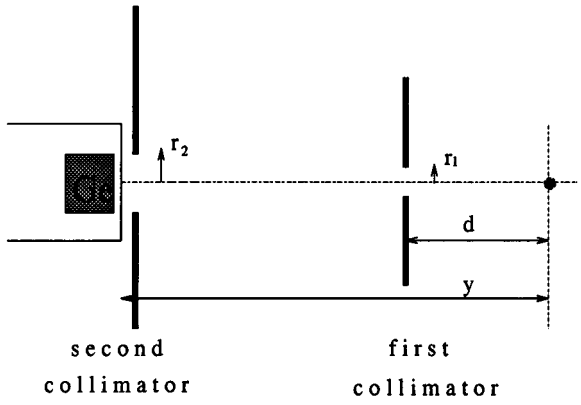

Figure 4.13 *Detector collimation.*

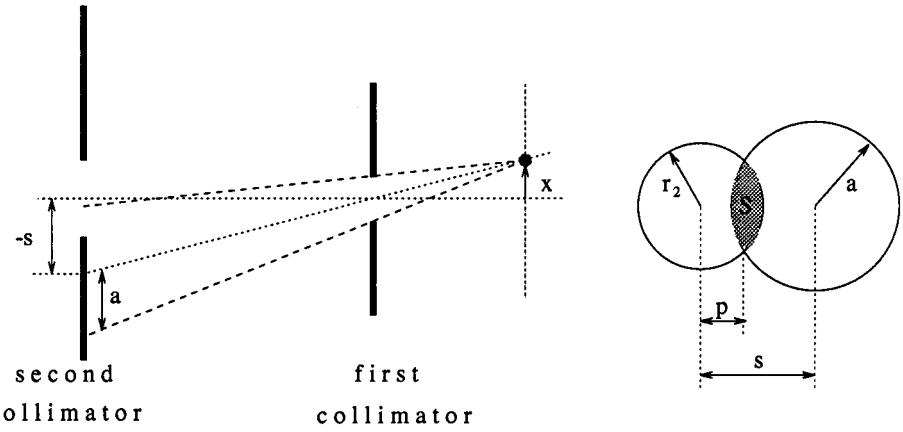

Figure 4.14 *Determination of the detector geometric efficiency by projection of the first collimator on the second one.*

the centre plane of the phantom of the area of the detector seen from that position has been computed and is drawn in fig. 4.15. Here also the thickness of the lead collimator has been taken into account.

Because of the radius of the phantom of maximal 8 cm, the value of y can vary between 125 cm and 141 cm resulting in slight differences of the curve. This curve will be flattened a bit for larger values of y, and it will be a bit higher and narrower for smaller values of y (see fig. 4.15). These calculations can be checked by measuring the number of ^{10}B counts of a small piece of boroncarbide (diameter $\approx$ 5 mm), while irradiated by thermal neutrons at different positions on the centre surface of the phantom. These results are shown in fig. 4.16.

The total efficiency of the detector for $E \approx 478$ keV at the centrepoint of the alignment can be determined by positioning a small calibrated ^{134}Cs source. This source emits gamma-rays including one of 475 keV (1.46% abundancy). With a front surface of the detector crystal of 15.5 cm^2 it is known that here $\epsilon_{geom} = \frac{15.5}{4\pi 133^2}$.
By this measurement ϵ_{tot}(475 keV) = $1.39.10^{-5}$ has been determined, so that ϵ_{det}(475 keV) = 0.20 can be concluded.

4.9 Tomography

Reconstruction of internal structures executing mathematical operations on external measurements is called tomography. In this case one likes to determine position dependent boron concentrations in the phantom (and later during therapy

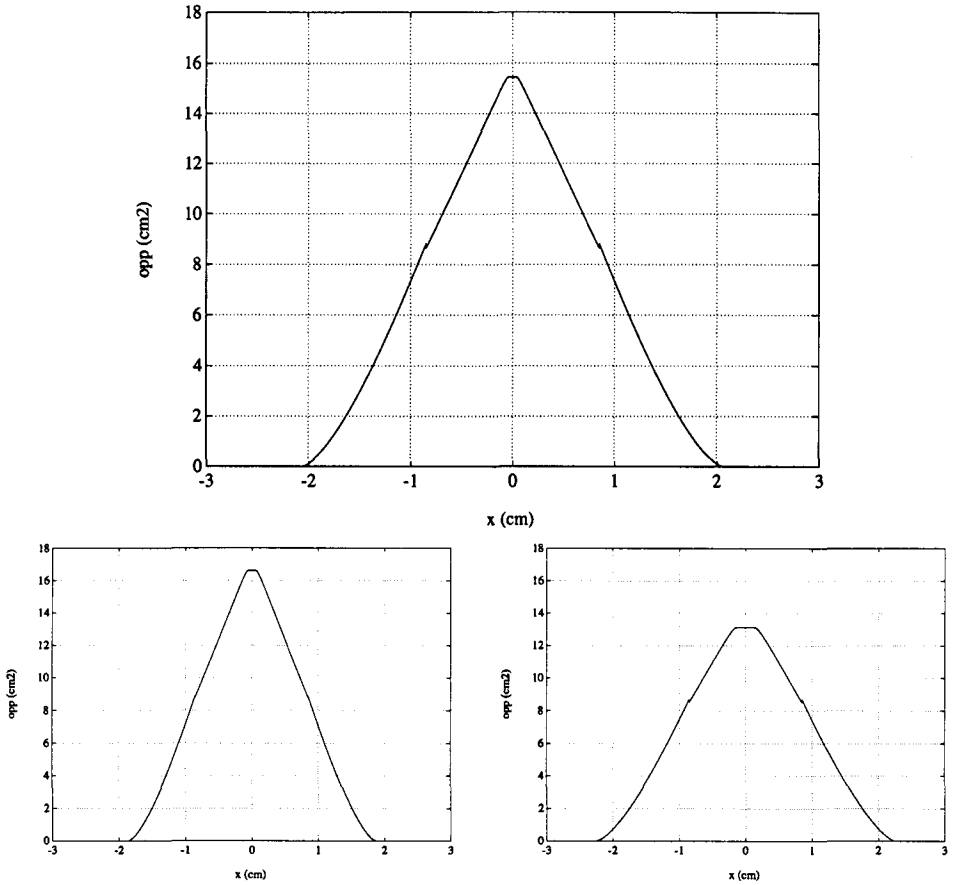

Figure 4.15 *Calculated space dependent geometric efficiency, multiplied with* $4\pi 133^2$. *a. for y = 133 cm, b. for y = 127 cm, c. for y = 139 cm.*

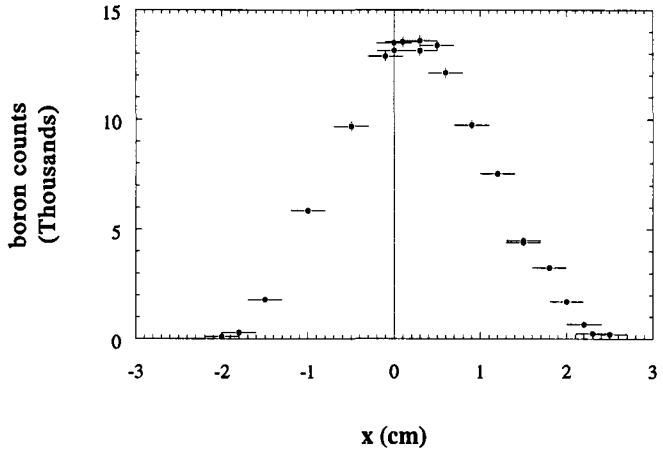

Figure 4.16 *Measurement of the shape of space dependent geometric efficiency by scanning a piece of* B_4C *positioned at y = 133 cm. The scan-axes is the x-axes.*

situation, in a human head) in one cylindrical slice. The most common method for tomography is "back projection". However, with that method the number of discrete area's is restricted to the number of measurements. In our situation 24 measurements have been performed for 24 subsequent equal angles to the circle (see chapter 4.6). In this way the cylindrical slice could be divided in only 4 x 6 cells, providing insufficient detail of the phantom.

Another possibility is to make some assumptions, and describe the situation with

a formula that can be fitted with the measurements [3]. In this case there are seven assumptions:

1. the boron background concentration is homogeneous over the slice,
2. the tumor concentration is homogeneous and added to the background,
3. the tumor is circular,
4. there is only one tumor,
5. the gamma-ray attenuation coefficient is that of water and equals 0.0986 cm^{-1} everywhere,
6. the thermal neutron flux is homogeneous over the cross section of the phantom,
7. the z-dependency of the detector geometric efficiency ϵ_{geom} is known.

The last assumption is not true (see fig. 3.6). As a matter of fact the thermal flux distribution should be taken into account.

The fitting parameters are (see fig. 4.17):

- y-coordinate of the center of the tumor at first angle, y_{tum0}
- z-coordinate of the center of the tumor at first angle, z_{tum0}
- radius of the tumor, r_{tum}
- overall background or bulk emitted boron gamma rate ($cm^{-2}s^{-1}$) by the entire phantom (including the tumor), C_{back}
- the extra boron gamma rate emitted by the tumor only, C_{tum}.

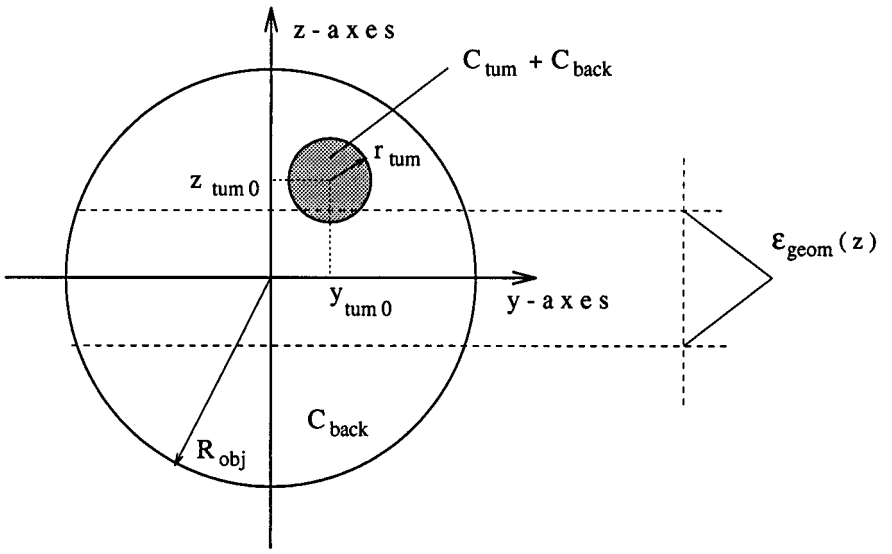

Figure 4.17 *Model of a cylindrical slice of the phantom with a cylindrical tumor.*

At height z the contribution of a bar dz is calculated. This consists of a line integral over y of the contribution of the bulk boron gamma rate and possibly the contribution of the tumor:

$$p(z)dz = \int_{-\sqrt{R_{obj}^2 - z^2}}^{\sqrt{R_{obj}^2 - z^2}} [p_{back}(y,z) + p_{tum}(y,z)]\, dy. \qquad (4.24)$$

Finally all the z contributions are integrated to the total measured ^{10}B gamma-rays

[3] This tomography program has been developped in cooperation with G. Leendertse of the mathematical department of the ECN.

(I_i) for the measurement with angle bin i:

$$I_i = \int_{-2}^{2} \epsilon_{det} \cdot \epsilon_{geom}(z) \cdot p(z) dz. \tag{4.25}$$

In the fitting formula the detector geometric efficiency $S(z)$ (see fig. 4.15) for y = 133 cm has been taken into account. For this use it has been simplified to a triangular shape.

Formula 4.25 has been fitted for all 24 angle bins i to the measured data. In fig. 4.18 the measured ^{10}B counts and the ultimate function fit are drawn. The computed results correspond well to the real values (see table 4.9).
The real begin situation was (y_{tum0}, z_{tum0}) = (0.78 , 2.90) cm, and calculated was (0.77 , 3.28) cm.
The real tumor radius of 1.1 cm agrees with the calculated r_{tum} = 0.96 cm.
In practice the relation between the boron concentration in tumor and background was $\frac{62}{5.1}$ = 12.2. The calculated relation between emitted boron gamma-rays in tumor and background was $\frac{(C_{tum}+C_{back})}{C_{back}} = \frac{(2.68 \cdot 10^8 + 2.02 \cdot 10^7)}{2.02 \cdot 10^7}$ = 14.3.
To obtain a figure of the absolute boron concentration distribution, the fitting formula has to be weighted with the thermal flux distribution as calculated by DORT. Another possibility to obtain absolute boron concentrations is to perform a calibration with a gauge phantom.

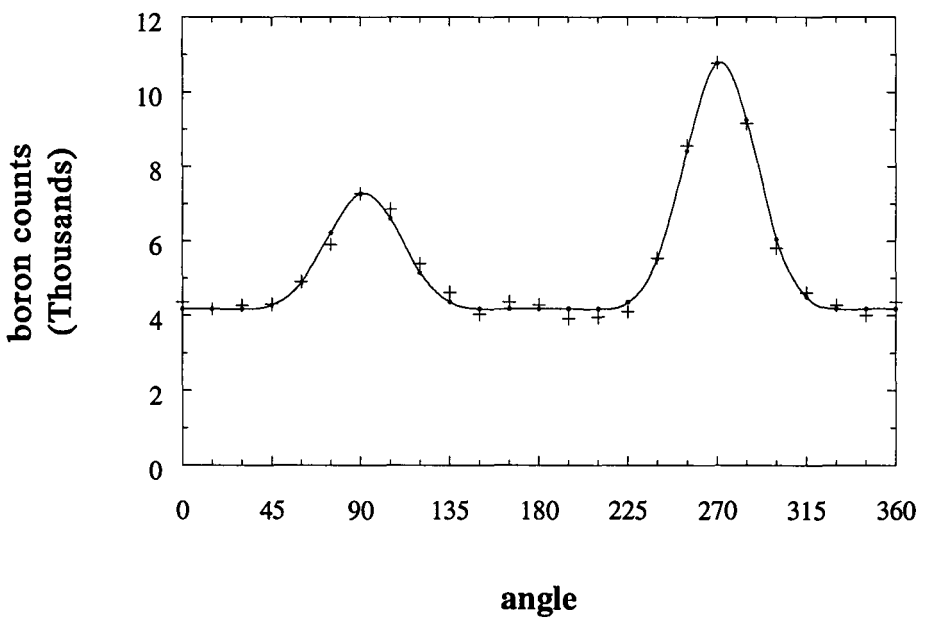

Figure 4.18 *The 24 measurements of boron counts and the fitted function of the tomography calculation.*

	real	calculated
y_{tum0}	0.78	0.77
z_{tum0}	2.90	3.28
r_{tum}	1.07	0.96
$\frac{C_{tum}+C_{back}}{C_{back}}$	12.2	14.3

Table 4.1 *Results of the tomography calculation compared to the real situation.*

5. CONCLUSIONS, DISCUSSION

The measurements have shown that it is indeed possible to detect small boron concentrations somewhere in a phantom at irradiation with epithermal neutrons ($\phi_{total} = 4.0 \cdot 10^6$ cm^{-2}s^{-1}). A very good detector collimation and shielding configuration is recommended. In this case it is a telescope configuration. Also tomography has proven to be possible with 24 measurements. At an enlarged flux of $6.6 \cdot 10^6$ cm^{-2}s^{-1}, tumor concentration of 62 ppm ^{10}B and background concentration of 5 ppm ^{10}B, a measuring time of 20 minutes was required for one angle. At the High Flux Reactor, the patient treatment beam HB11, the total flux is about 70 times higher. If the scaling to measuring time is proportional, then this could be reduced to less than a minute per angle. This however will require faster detection systems. The overall conclusion is that a on-line space dependent boron measuring system during irradiation with neutrons is possible to realize, favourably with more detectors. Also reconstruction out of 24 data points to a two dimensional picture of the boron concentration for a single tumor belongs to the possibilities. To obtain absolute boron concentrations there are two possibilities:

1. unfolding of the tomography results with the calculated thermal neutron flux distribution,
2. calibration with a gauge phantom.

For the calculation of the neutron spectrum the computer code MCNP has been used. Following are some conclusions that can be made. It appeared that MCNP is a good code to calculate a neutron spectrum in a beam tube of a nuclear reactor at a large distance of the core. Because of that large distance and a neutron beam arrangement the use of the variance reduction technique DXTRAN in combination with the weight window generator is recommended. The shape of the neutron flux spectrum at the phantom position can be calculated correct. However the absolute value of the flux appeared to be a factor 1.5 too high. This can be caused by several reasons:

- The core of the reactor has not been modelled well (homogenized fuel elements).
- The distribution modelling of the release of source neutrons could be ameliorated by having more measurements of the real neutron flux distributions (thermal as well as fast) in the fuel elements.
- All used cross sections have uncertainties. As neutrons from the graphite reflector have to be scattered into a very small solid angle through the beam to arrive at the phantom position, the model and data for the probability of scattering should be very accurate.
- The composition and densities of the modelled materials may have little differences compared to the real materials
- The reactor power level cannot be checked with an energy balance. Therefore it is not exactly known how well an indicated power level of 30 kW corresponds to really 30 kW.

The importance of correct absolute values of cross sections appears from the calculated flux inside HN. By changing the density and the hydrogen fraction of the sand around the beam, large changes of the flux occurred.

A conclusion that can be made by comparing the 2 calculated spectra, inside the beam channel and outside, is that the shape is not the same. This means that wrong results can be obtained when splitting a large calculation into two smaller

ones. If a calculation had been done by defining a neutron source as the first calculated spectrum inside HN, the shape at the phantom position would be the same, corrected with a cut-off beneath 0.5 eV due to Cd.

By a better understanding where neutrons scatter before arriving at a position, it appeared to be possible to optimize the flux. For an extra piece of graphite in the front end of the beam the predicted values roughly agreed with measurements. The boron count rate increased with 79%.

DORT is able to calculate neutron distributions over a less complex system. Taking into account the transport of gamma's in air or water in the used geometry is not possible because of the "ray-effect". The factor 1.7 too high calcultated values compared with measurements may have 3 reasons:

- The used neutron source spectrum (of MCNP) appeared to be a factor 1.5 too high.
- The measured activity could be at maximum 10% too low because of self shielding.
- The available group cross sections in the BUGGLE80 library have only one thermal group. More thermal groups could improve the results of reactions with thermal neutrons.

6. TECHNOLOGY ASSESSMENT

It may be clear that BNCT will be of great use in the battle against cancer. Especially when it concerns brain tumors as there is no other therapy for brain tumors yet. When it is proven that BNCT is working well and patients with brain tumors can be cured, this technique has large medical and social relevance. Also of social relevance is the fact that there is created a new positive function of a nuclear reactor, and a new application of nuclear technology in medicine.

At the moment the use of conventional cancer therapies (photon irradiation, chemo therapy) cannot give the same tumor selectivity of the dose as provided by BNCT. Therefore BNCT allows a much larger saving of healthy tissue, because:

1. a tumor seeking boron compound causes a difference of boron concentration between tumor and healthy tissue of about a factor of 10,
2. the largest contribution to the total dose is caused by the $^{10}B(n,\alpha)^{7}Li$ reaction. The high energetic Li and He particles cause a high cell killing ratio by damaging the cells in which they are stopped saving the healthy tissue. These cells are destroyed due to the large amount of closely spaced ionizations.

BNCT with thermal neutrons has been performed many times already by the Japanese. Because of the small penetration depth of thermal neutron they had to remove the skull of the patients head. This will not be necessary any more with the use of epithermal neutron beams as in the HFR in Petten. BNCT may also be applied for several kinds of cancer. One example is the fight of skin melanomas for which thermal neutron beams can be used.

The possibility of on-line determination of boron concentrations is of great use for an ultimate patients dose monitoring system. It is very important not to exceed a specific dose during the irradiation. The determination of the dose has been complicated by the large changes of boron concentration in tumor and healthy tissue in time. This problem can be solved now by the possibility of tomography of the boron concentration in the head, during one irradiation of about 20 minutes.

REFERENCES

[1] D.Gabel
Safety and Efficacy in Boron Neutron Capture Therapy
In: Boron Neutron Capture Therapy, toward Clinical Trials of Glioma Treatment, D.Gabel, R.Moss, 7-13
Plenum Press, New York and London (1992)

[2] G.Stragliotto, D.Schüpbach, P.R.Gavin, H.Fankhauser
Update on biodistribution of borocaptate sodium (BSH) in patients with intracranial tumors
In: Advances in Neutron Capture Therapy, A.H.Soloway, R.F.Barth, D.E.Carpenter, 719-726
Plenum Press, New York and London (1993)

[3] D.Haritz, D.Gabel, H.Klein, R.Huiskamp
Results of continued clinical investigations of BSH in patients with malignant glioma
In: Advances in Neutron Capture Therapy, A.H.Soloway, R.F.Barth, D.E.Carpenter, 727-730
Plenum Press, New York and London (1993)

[4] J.E.Hoogenboom, H.van Dam
Kernreactorkunde
collegedictaat c27, Technical University of Delft (1991)

[5] S.Glasstone, M.C.Edlund
The elements of Nuclear Reactor Theory
D. van Nostrand Company (1952)

[6] J.F.Briesmeister
MCNP - A General Monte Carlo N-Particle Transport Code
Version 4A, University of California (1993)

[7] T.E.Booth
A Sample Problem for Variance Reduction in MCNP
LA-10363-MS, Los Alamos (1985)

[8] W.E. Freudenreich, F.Stecher-Rasmussen, J.B.M.de Haas
Development study of a biological thermal neutron facility for the Petten BNCT project at the LFR
ECN-report, ECN-I–92-022 (1992)

[9] ECN-report Memo: Fys/RASA-83/03 (1983)

[10] W.A.Rhoads, R.L.Childs
The TORT Three-Dimensional Discrete Ordinates Neutron/Photon Transport Code
report ORNL-6286, Oak Ridge National Laboratory (1987)

[11] T.Matsumoto, O.Aizawa
Phantom Experiment and Calculation for in Vivo ^{10}B Analysis by Prompt Gamma-ray Spectroscopy
Phys. Med. Biol. (1991) Vol. 36, 329-338

[12] T.Kobayashi, K.Aoki, M.Ono, K.Kanda
Measurement of ^{10}B concentrations and its location in phantom by prompt gamma-ray spectroscopy
In: Neutron Capture Therapy, H.Hatanaka, 2-8
MTP, Lancaster (1986)

[13] K.S.Krane
Introductory Nuclear Physics
John Wiley & Sons, Inc. (1988)

[14] R.H.Pehl
Germanium gamma-ray detectors
Physics Today 50-61, november (1977)
[15] N.Fourches, A.Huck, G.Walter
The role of secondary defects in the loss of energy resolution of fast-neutron-irradiated HPGe gamma-ray detectors
IEEE Transactions on Nuclear Science, Vol. 38, No. 6, 1728-1735 (1991)
[16] P.H.Stelson, J.K.Dickens, S.Raman, T.C.Trammell
Deterioration of large Ge(Li) diodes caused by fast neutrons
Nuc. Instr. Meth., Vol. 98, 481-484 (1972)
[17] L.S.Darken, R.C.Trammell, T.W.Raudorf, R.H.Pehl J.H.Elliott
Mechanism for fast neutron damage of Ge(HP) detectors
Nuc. Instr. Meth., Vol. 171 49-59 (1980)
[18] U.Hauser, W.Neuwirth, W.Pietsch, K.Richter
On the determination of collision cross sections by nuclear Doppler shift
Z. Physik, Vol. 269, 181-188 (1974)
[19] W.Neuwirth, U.Hauser, E.Kühn
Energy loss of charged particles in matter
Z. Physik, Vol. 220, 241-264 (1969)
[20] P.J.J.Kok
Capture of thermal neutrons in ^{10}B and ^{7}Li
Proefschrift, ECN Petten (1986)
[21] R.P.Feynman, R.B.Leighton, M.L.Sands
Feynman Lectures on Physics, Volume 1, chapter 34
California Institute of Technology (1989)
[22] J.D.Jackson
Classical Electrodynamics, second edition, chapter 11
John Wiley & Sons, Inc. (1975)
[23] J.F.Ziegler
TRIM-88 The Transport of Ions in Matter
Computer Program, IBM Research, Yorktown New York (1987)

APPENDIX A. MCNP INPUT FILE OF THE LFR

```
rm  lfr103.out
#
ln -s /home/urbi2/reactor/nucdat/mcnp/4A/lanl/d9 d9
ln -s  /home/urbi2/reactor/nucdat/mcnp/4A/lanl/endl85 endl85
ln -s   /home/urbi2/reactor/nucdat/mcnp/4A/lanl/532dos 532dos
ln -s  /home/urbi2/reactor/nucdat/mcnp/4A/lanl/bmccs bmccs
ln -s  /home/urbi2/reactor/nucdat/mcnp/4A/lanl/tmccs tmccs
ln -s  /home/urbi2/reactor/nucdat/mcnp/4A/eff1.3/leff13 leff13
ln -s libs/mcnp4a_wilko xsdir
#
cat <<EOF > inp
message: mctal=mc

BNCT - LFR    Wilko Verbakel  mrt. 1994
C
C
C
C
C
C
C
C
C
C
C
C    C E L L - cards
C    ===============
C
C    O U T S I D E   W O R L D
    1    0     (-15 :  1 : -24 : 16 : -38 : 25)
               (-10 :  5 : 24 : -115: 85 : -86)
C
C    concrete south + north
    2   25 -3.5     15  -10   17  -16   38  -25
    3   25 -3.5     10   -6   17  -16   38  -25
    4   25 -3.5      6   -5   17  -16   38  -25
    5   25 -3.5      5   -1   17  -16   38  -25
    6   25 -3.5     15  -10   24  -23   38  -25
    7   25 -3.5     10   -6   24  -23   38  -25
                    (85 : -86)
    8   25 -3.5      6   -5   24  -23   38  -25
                    (85 : -86)
    9   25 -3.5      5   -1   24  -23   38  -25
C    thermal column
   10    1 -1.6      2   -1   23  -17   38  -25
C    VC
   11    7 -1.840                -39   36  -35
   12    6 -1.826                -39   35  -32
   13    5 -.5061                -39   32  -26
C    inner graphit reflector (8 segments)
   14    1 -1.6     20  -45   39  -40   36  -26
   15    1 -1.6     45    5   39  -40   36  -26
   16    1 -1.6     -5   44   39  -40   36  -26
   17    1 -1.6    -44   20   39  -40   36  -26
   18    1 -1.6    -20   45   39  -40   36  -26
   19    1 -1.6    -45   -5   39  -40   36  -26
   20    1 -1.6      5  -44   39  -40   36  -26
   21    1 -1.6     44  -20   39  -40   36  -26
C    below inner graphit reflector
   22   17 -2.133       -40             37  -36
   23   18 -1.567       -40             38  -37
C    core ring fuel region one plate core (6 sgments)
   24    8 -1.518  -45   46   40  -42   34  -30
   25    8 -1.518  -46   47   40  -42   34  -30
   26    8 -1.518  -47   -5   40  -42   34  -30
   27    8 -1.518    5   48   40  -42   34  -30
   28    8 -1.518  -48   49   40  -42   34  -30
   29    9 -1.576  -49  -44   40  -42   34  -30
C                above fuel
   30   10 -1.225  -45   46   40  -42   30  -29
```

```
   31   10 -1.225  -46   47   40  -42   30  -29
   32   10 -1.225  -47   -5   40  -42   30  -29
   33   10 -1.225    5   48   40  -42   30  -29
   34   10 -1.225  -48   49   40  -42   30  -29
   35   12 -1.180  -49  -44   40  -42   30  -29
C                 below fuel
   36   11 -1.450  -45   46   40  -42   35  -34
   37   11 -1.450  -46   47   40  -42   35  -34
   38   11 -1.450  -47   -5   40  -42   35  -34
   39   11 -1.450    5   48   40  -42   35  -34
   40   11 -1.450  -48   49   40  -42   35  -34
   41   13 -1.403  -49  -44   40  -42   35  -34
C                 below fuel elements
   42   16 -1.169  -45   47   40  -42   38  -35
   43   16 -1.169  -47   48   40  -42   38  -35
   44   16 -1.169  -48  -44   40  -42   38  -35
C                 above fuel elements
   45   14 -1.074  -45   47   40  -42   29  -28
   46   14 -1.074  -47   48   40  -42   29  -28
   47   14 -1.074  -48  -44   40  -42   29  -28
C                 above H2O
   48   15 -0.118  -45  -44   40  -42   28  -26
C    core ring (fuel) region two plate core (6 sgments)
   49    9 -1.576   45  -46   40  -42   34  -30
   50    9 -1.576   46  -47   40  -42   34  -30
   51    9 -1.576   47    5   40  -42   34  -30
   52    9 -1.576   -5  -48   40  -42   34  -30
   53    9 -1.576   48  -49   40  -42   34  -30
   54    9 -1.576   49   44   40  -42   34  -30
C                 above (fuel)
   55   12 -1.180   45  -46   40  -42   30  -29
   56   12 -1.180   46  -47   40  -42   30  -29
   57   12 -1.180   47    5   40  -42   30  -29
   58   12 -1.180   -5  -48   40  -42   30  -29
   59   12 -1.180   48  -49   40  -42   30  -29
   60   12 -1.180   49   44   40  -42   30  -29
C                 below (fuel)
   61   13 -1.403   45  -46   40  -42   35  -34
   62   13 -1.403   46  -47   40  -42   35  -34
   63   13 -1.403   47    5   40  -42   35  -34
   64   13 -1.403   -5  -48   40  -42   35  -34
   65   13 -1.403   48  -49   40  -42   35  -34
   66   13 -1.403   49   44   40  -42   35  -34
C                 below (fuel) elements
   67   16 -1.169   45  -47   40  -42   38  -35
   68   16 -1.169   47  -48   40  -42   38  -35
   69   16 -1.169   48   44   40  -42   38  -35
C                 above (fuel) elements
   70   14 -1.074   45  -47   40  -42   29  -28
   71   14 -1.074   47  -48   40  -42   29  -28
   72   14 -1.074   48   44   40  -42   29  -28
C                 above H2O
   73   15 -0.118   45   44   40  -42   28  -26
C    core ring (fuel) region west
   74    9 -1.576   44  -20   40  -42   34  -30
   75    9 -1.576   20  -45   40  -42   34  -30
C                 above (fuel)
   76   12 -1.180   44  -20   40  -42   30  -29
   77   12 -1.180   20  -45   40  -42   30  -29
C                 below (fuel)
   78   13 -1.403   44  -20   40  -42   35  -34
   79   13 -1.403   20  -45   40  -42   35  -34
C                 below (fuel) elements
   80   16 -1.169   44  -45   40  -42   38  -35
C                 above (fuel) elements
   81   14 -1.074   44  -45   40  -42   29  -28
C                 above H2O
   82   15 -0.118   44  -45   40  -42   28  -26
C    core ring (fuel) region east
   83    9 -1.576   20  -44   40  -42   34  -30
                    (  91 : 92 : -93)
   84    9 -1.576   45  -20   40  -42   34  -30
                    (  91 : 92 : -93)
```

```
C                  above (fuel)
   85   12 -1.180    20  -44   40  -42   30  -29
   86   12 -1.180    45  -20   40  -42   30  -29
C                  below (fuel)
   87   13 -1.403    20  -44   40  -42   35  -34
   88   13 -1.403    45  -20   40  -42   35  -34
C                  below (fuel) elements
   89   16 -1.169    45  -44   40  -42   38  -35
C                  above (fuel) elements
   90   14 -1.074    45  -44   40  -42   29  -28
C                  above H2O
   91   15 -0.118    45  -44   40  -42   28  -26
C    Cadmium safety and control plates
C          P1
   92    1 -1.6      44   48   42  -43   29  -26
   93    3 -.0012    44   48   42  -43   33  -29
   94    1 -1.6      44   48   42  -43   38  -33
C          P3
   95    1 -1.6      45  -47   42  -43   29  -26
   96    3 -.0012    45  -47   42  -43   33  -29
   97    1 -1.6      45  -47   42  -43   38  -33
C          P4
   98   20 -.352    -48  -44   42  -43   27  -26
   99   21 -2.6     -48  -44   42  -43   30  -27
  100   20 -.352    -48  -44   42  -43   33  -30
  101    1 -1.6     -48  -44   42  -43   38  -33
C          P6
  102   20 -.352     47  -45   42  -43   27  -26
  103   21 -2.6      47  -45   42  -43   30  -27
  104   20 -.352     47  -45   42  -43   33  -30
  105    1 -1.6      47  -45   42  -43   38  -33
C          P2
  106   20 -.352     47  -48   42  -43   31  -26
  107   21 -2.6      47  -48   42  -43   33  -31
  108    1 -1.6      47  -48   42  -43   38  -33
C          P5
  109   20 -.352     48  -47   42  -43   30  -26
  110   22 -2.418    48  -47   42  -43   50  -30
  111   20 -.352     48  -47   42  -43   33  -50
  112    1 -1.6      48  -47   42  -43   38  -33
C    graphite around core (3-point blocks, 8)
C          north
  113    1 -1.6    6  -5  21  -45  43  38  -26
               (56: -30) (  91 : 92 : -93)
  114    1 -1.6    5  -4  21  -44  43  38  -26
               (55: -30)
C          west
  115    1 -1.6    44  42  -4  -20     38  -26
               (55: -30)
  116    1 -1.6    42  -4  20  -45     38  -26
               (54: -30)
C          south
  117    1 -1.6    5  -4  -19  45  43  38  -26
               (54: -30)
  118    1 -1.6    6  -5  -19  44  43  38  -26
               (53: -30)
C          east
  119    1 -1.6    6  42   20  -44     38  -26
               (53: -30) (  91 : 92 : -93)
  120    1 -1.6    6  42  -20   45     38  -26
               (56: -30) (  91 : 92 : -93)
C    graphite reflector
C          west
  121    1 -1.6     4   -3   23  -17   38  -51
               ((54  55) : -30)
  122    1 -1.6     4   -3   22  -18   51  -26
                (54  55)
  123    1 -1.6     3   -2   22  -18   38  -51
C          south
  124    1 -1.6     6   -5   19  -18   38  -26
               (53: -30)
  125    1 -1.6     5   -4   19  -18   38  -26
               (54: -30)
```

```
  126    1 -1.6    6   -5   18  -17   38  -51
  127    1 -1.6    5   -4   18  -17   38  -51
C           north
  128    1 -1.6    6   -5   22  -21   38  -26
               (56: -30) (  91 : 92 : -93)
  129    1 -1.6    5   -4   22  -21   38  -26
               (55: -30)
  130    1 -1.6    6   -5   23  -22   38  -51
                         (  91 : 92 : -93)
  131    1 -1.6    5   -4   23  -22   38  -51
C           east
  132    1 -1.6    7   -6   22  -18   38  -26
               ((53  56) : -30) ( 92 : -93)
  133    1 -1.6    8   -7   22  -18   38  -26
               ((53  56) : -30) ( 92 : -93)
  134    1 -1.6    7   -6   23  -22   38  -51
                       ( 92 : -93)
  135    1 -1.6    8   -7   23  -22   38  -51
                       ( 92 : -93)
  136    1 -1.6    7   -6   18  -17   38  -51
  137    1 -1.6    8   -7   18  -17   38  -51
  138    1 -1.6    9   -8   22  -18   38  -51
  139    1 -1.6   10   -9   22  -18   38  -51
C    aluminium construction around reflector
C           vertical 4
  140   19 -0.367   10   -8   18  -17   38  -26
  141   19 -0.367    3   -2   18  -17   38  -26
  142   19 -0.367    3   -2   23  -22   38  -26
  143   19 -0.367   10   -8   23  -22   38  -26
C           top 4
  144   19 -0.367    8   -3   18  -17   51  -26
  145   19 -0.367    3   -2   22  -18   51  -26
  146   19 -0.367    8   -3   23  -22   51  -26
  147   19 -0.367   10   -8   22  -18   51  -26
C    above graphite reflector
  148   26 -2.6     10   -5   23  -17   26  -25
  149   26 -2.6      5   -4   23  -17   26  -25
  150   26 -2.6      4   -2   23  -17   26  -25
C    concrete BIBOP north
  151   25 -3.5     13  -10   23  -22   38  -25
  152   25 -3.5     14  -13   23  -22   38  -25
  153   25 -3.5     15  -14   23  -22   38  -25
C    concrete BIBOP south
  154   25 -3.5     13  -10   18  -17   38  -25
  155   25 -3.5     14  -13   18  -17   38  -25
  156   25 -3.5     15  -14   18  -17   38  -25
C    concrete above BIBOP
  157   25 -3.5     13  -10   22  -18   26  -25
  158   25 -3.5     14  -13   22  -18   26  -25
  159   25 -3.5     15  -14   22  -18   26  -25
C    steel wagon BIBOP (below)
  160   27 -1.581   13  -10   22  -18   38  -52
  161   27 -1.581   14  -13   22  -18   38  -52
  162   27 -1.581   15  -14   22  -18   38  -52
C    irradiation chamber BIBOP
  163    3 -.00125  11  -64   22  -18   52  -26
                    (-57 : 58 : -60 : 59)
  164    2 -11.4    12  -11   22  -18   52  -26
                    (-57 : 58 : -60 : 59)
  165    3 -.00125  13  -12   22  -18   52  -26
  166    3 -.00125  61  -13   22  -18   52  -26
  167   25 -3.5     15  -14   22  -18   52  -26
C
C    Wholes D1 ... D4
  168    1 -1.6      -53  30  -26
  169   23 -.149     -54  30  -26
  170    1 -1.28     -55  30  -26
  171   24 -1.577    -56  30  -26
C
C
  172    2  -11.4    65  -11  57  -58  60  -59
  173    3 -.00125   11  -64  57  -58  60  -59
C
```

```
  174   3 -.00125   64  -10  22  -18  52  -26
C
  175   3 -.00125   62  -61   22  -18   52  -26
  176   3 -.00125   63  -62   22  -18   52  -26
  177   3 -.00125   14  -63   22  -18   52  -26
C
  178   2 -11.4     12  -66  57  -58  60  -59
  179   2 -11.4     66  -65  57  -58  60  -59
C
C    Beam HN
  180   3 -.00125   70  -71  -20  42  88  -74   75
  181   3 -.00125   70  -71  -88  89  -74  75
  182   3 -.00125   70  -71  -89  90  -74  75
  183   3 -.00125   70  -71  -90  83  -74  75
  184   3 -.00125   70  -71  -83  84  -74  75
  185   3 -.00125   70  -71  -84  78  -74  75
  186   3 -.00125  -79   81   -87
  187   3 -.00125   72  -73  -81 106  -76  77
  188   3 -.00125   72  -73 -106 107  -76  77
  189   3 -.00125   72  -73 -107 102  -76  77
  190   3 -.00125 -103  101   -87
  191   3 -.00125 -101  105  111 -110 113 -112
  192   3 -.00125 -105  109  10  -5  86  -85
                  (108 :306)
  193   3 -.00125 -108  109  -306
C    concrete around HN
  194  25 -3.5      10   -7   24  -23  -85  86
  195  25 -3.5       7   -5   24  -23  -85  86
                    ( 91 :-128:129)
                    (-134 : 132 : -133 : 130 : -131)
C    sand around HN
  196  36 -1.5       7  -91   94  -23  -129 128
                    (-125 : 124 : 126 : -127)
  197  36 -1.5       7  -91   78  -94  -129 128
                    (-125 : 124 : 126 : -127)
  198  36 -1.5       7  -91  -78  106  -129 128
                    (-121 : 120 : 122 : -123)
  199  36 -1.5       7  -91 -106  107  -129 128
                    (-121 : 120 : 122 : -123)
  200  36 -1.5       7  -91 -107  101  -129 128
                    (-121 : 120 : 122 : -123)
C
C    Graphite around HN
  201   1 -1.6       6  -91   23  -22  -92  93
                    (-70 : 71 : 74 : -75)              $ in 130
  202   1 -1.6       6  -91   22  -21  -92  93
                    (-70 : 71 : 74 : -75)              $ in 128
  203   1 -1.6       6  -91   21  -45  43   -92  93
                    (-70 : 71 : 74 : -75)              $ in 113
  204   1 -1.6       6   42  -20   45  -92  93
                    (-70 : 71 : 74 : -75)              $ in 120
  205   1 -1.6       6   42   20  -44  -91   -92  93    $ in 119
  206   9 -1.576    45  -20   40  -42  -91   -92  93    $ in 84
                    (-70 : 71 : 74 : -75)
  207   9 -1.576    20  -44   40  -42  -91   -92  93    $ in 83
  208   1 -1.6       7   -6   22  -20   93  -92         $ in 132
  209   1 -1.6       7   -6   20  -18   93  -92         $ in 132
  210   1 -1.6       8   -7   22  -20   93  -92         $ in 133
  211   1 -1.6       8   -7   20  -18   93  -92         $ in 133
  212   1 -1.6       7   -6   23  -22   93  -92         $ in 134
  213   1 -1.6       8   -7   23  -22   93  -92         $ in 135
  214   1 -1.6       70  -71  -74  75  -42 -20 45       $ in 205
C
  215  25 -3.5      10   -5  -24  106  -85  86
                    ( -7 : 91 : -128 : 129)
  216  25 -3.5      10   -5 -106  107  -85  86
                    ( -7 : 91 : -128 : 129)
  217  25 -3.5      10   -5 -107  101  -85  86
                    ( -7 : 91 : -128 : 129)
  218  25 -3.5      10   -5 -101  105  -85  86
                    ( -7 : 91 : -93 : 92)
  219  25 -3.5       7  -91 -101  105  -92  93
                    (-111 : 110 : 112 : -113)
```

```
C     2nd neutron collimator
  220  34 -8.6      72  -73 -102  103  -76  77
  221  35 -0.93     72  -73 -103  104   87 -76  77
  222  2  -11.4     72  -73 -104  101   87 -76  77
C     1st neutron collimator
  223  34  -8.6     72  -73  -78  79  -76  77
  224  35  -0.93    72  -73  -79  80  87  -76  77
  225   2 -11.4     72  -73  -80  81  87  -76  77
C
  226   3 -.00125 -109  114   10  -5  86  -85
                 (306 : 200 : -214)
C     Iron around HN
  227  37 -7.3     125  -124  127  -126  94  -23
                    ( -70 : 71 : 74 : -75)
  228  37 -7.3     125  -124  127  -126  78  -94
                    ( -70 : 71 : 74 : -75)
  229  37 -7.3      121  -120  123  -122  106 -78
                    ( -72 : 73 : 76 : -77)
  230  37 -7.3     121  -120  123  -122  107 -106
                    ( -72 : 73 : 76 : -77)
  231  37 -7.3      121  -120  123  -122  101 -107
                    ( -72 : 73 : 76 : -77)
C     Hole for source
  232   3 -.00125  134  -5  131  -130  -132  133
C     Foils
  233   3 -.00125    -200  201 304 -306              $ void @ foil1
  234   3 -.00125    -211  212 304 -306              $ void @ foils
  235   3 -.00125    -212  214 305 -306              $ void @ foils
C
  236   41 -2.723       -304    -200  201            $ Au/Al
  237   42 -2.703       -304    -202  203            $ In/Al
  238   50 -2.7         -304    -203  204            $ Al
  239   41 -2.723       -304    -204  205            $ Au/Al
  240   44 -2.723       -304    -205  206            $ W/Al
  241   45 -3.364       -304    -206  207            $ U238/Al
  242   50 -2.7         -304    -207  208            $ La/Al but Al
  243   46 -2.717       -304    -208  209            $ Mn/Al
  244   47 -2.902       -304    -209  210            $ Cu/Al
  245   48 -7.31        -304    -211  212            $ In
  246   49 -8.90        -305    -212  213            $ Ni
  247   50 -2.7         -305    -213  214            $ Al
  248   51 -8.65        (305:202:-210) -306 -201 211  $ Cd case
  249   3  2.66810E-5   -305 304 -202  210           $ Void in Cd
C     Beam catcher
  250   35 -.93     -114  115  10  -5  86  -85

C
C
C    S U R F A C E - cards
C    =====================
C
    1 PX      100.0              $  pos. x-boundary
    2 PX       77.95             $  west end of graph. refl.
    3 PX       62.7              $  right step in graph. refl.
    4 PX       50.2              $  close to cylinder for Cd
    5 PX        0.0              $
    6 PX      -50.2              $  close to cylinder for Cd
    7 PX      -53.8              $  split. surf. in refl.
    8 PX      -62.7              $  left step in graph. refl.
    9 PX      -70.5              $  split. surf. in refl.
   10 PX      -77.95             $  east end of graph. refl.
   11 PX      -82.0              $  end of lead plate
   12 PX      -93.2              $  begin of lead plate
   13 PX      -96.2              $  monitor surface
   14 PX     -150.0              $  end of concrete
   15 PX     -200.0              $  neg. x-boundary
C
   16 PY      120.0              $  pos. y-boundary
   17 PY       77.95             $  south end of graph. refl.
   18 PY       62.7              $  step in graph. refl.
   19 PY       50.3              $  close to cylinder for Cd
   20 PY        0.0              $
   21 PY      -50.3              $  close to cylinder for Cd
```

```
   22 PY      -62.7              $  step in graph. refl.
   23 PY      -77.95             $  north end of graph. refl.
   24 PY     -120.0              $  neg. y-boundary
C
   25 PZ       75.0              $  upper boundary
   26 PZ       64.0              $  upper end graph. refl.
   27 PZ       60.0              $  top Cd
   28 PZ       57.0              $  top H2O
   29 PZ       42.0              $  top fuel element
   30 PZ       30.5              $  top fuel
   31 PZ       14.0              $  top Cd
   32 PZ       -8.6              $  1/3 graph. in VC
   33 PZ      -16.5              $  bottem Cd
   34 PZ      -30.5              $  bottem fuel
   35 PZ      -42.0              $  bottem fuel element
   36 PZ      -50.0              $  bottem centr. graph. refl.
   37 PZ      -53.0              $  bottem inner vessel
   38 PZ      -56.0              $  lower boundary
C
   39 CZ        5.08             $  VC
   40 CZ       30.4              $  inner vessel
   41 CZ       38.0              $  cylinder between fuel elem.
   42 CZ       46.4              $  outer vessel
   43 CZ       50.2              $  cylinder for Cd
C
   44  1  PX    0.0              $  y1
   45  1  PY    0.0              $  x1
   46  2  PY    0.0              $  x2
   47  3  PY    0.0              $  x3
   48  4  PY    0.0              $  x4
   49  5  PY    0.0              $  x5
C
   50 PZ       0.0              $  Centre line fuel
   51 PZ      48.75             $  step in graph. refl.
   52 PZ     -44.0              $  wagon BIBOP
C
   53  8  CZ    8.25             $  D1
   54  6  CZ    8.25             $  D2
   55  7  CZ    8.25             $  D3
   56  9  CZ    8.25             $  D4
C    additional surfaces for segmenting
   57 PZ     -10.0
   58 PZ      10.0
   59 PY      10.0
   60 PY     -10.0
   61 PX     -98.2
   62 PX    -103.2
   63 PX    -108.2
C    additional surface for boron
   64 PX     -81.5
C    additional surface for Bi / Al
   65 PX     -89.0
   66 PX     -89.2
C
   70 PX     -44.61             $  left boundary HN
   71 PX     -36.67             $  right boundary HN
   72 PX     -45.64
   73 PX     -35.64
   74 PZ       3.97             $  upper boundary HN
   75 PZ      -3.97             $  lower boundary HN
   76 PZ       5.0
   77 PZ      -5.0
   78 PY    -124.0              $  first Cd filter in HN
   79 PY    -124.1              $  1mm Cd filter
   80 PY    -134.1              $  Polyboron collimator
   81 PY    -139.1              $  Pb collimator
C
   83 PY    -110.0        $  surface for cell for flux tally
   84 PY    -112.0
   85 PZ      50.0              $  extra surface
   86 PZ     -50.0              $  extra surface
   87 10 CY    4.0              $  8cm diameter collimator
C
```

```
   88 PY      -40.0              $  extra surface
   89 PY      -60.0              $  in HN tube
   90 PY      -85.0              $  idem
   91 PX      -25.0              $  extra surface in concrete
   92 PZ       14
   93 PZ      -14
   94 PY      -93                $  extra surface in concrete
C
  101 PY     -260.0              $  End of concrete of reactor
  102 PY     -244.9              $  2nd Cd filter in HN
  103 PY     -245.0              $  1 mm Cd filter
  104 PY     -255.0              $  Polyboron collimator
  105 PY     -340.0              $  end of shutter
  106 PY     -160.0              $  extra surface in concrete
  107 PY     -210.0              $  ,,
  108 PY     -449.8              $  phantom  position
  109 PY     -449.9
  110 PX      -31.64             $  shutter hole
  111 PX      -49.64
  112 PZ        9.0
  113 PZ       -9.0
  114 PY     -592.0              $  polyboron beam catcher
  115 PY     -620.0
C
  120 PX      -35.24             $  beam tube, 4mm
  121 PX      -46.04
  122 PZ        5.4
  123 PZ       -5.4
  124 PX      -36.27
  125 PX      -45.01
  126 PZ        4.37
  127 PZ       -4.37
C
  128 PZ      -11.0
  129 PZ       35.0
C
  130 PY      -82.0
  131 PY      -95.0              $ source hole
  132 PZ        6.5
  133 PZ       -6.5
  134 PX      -24.0
C
C    Planes to define foils
  200 PY -450.0
  201 PY -450.02
  202 PY -450.12
  203 PY -450.14
  204 PY -450.15
  205 PY -450.17
  206 PY -450.19
  207 PY -450.20
  208 PY -450.22
  209 PY -450.24
  210 PY -450.26
  211 PY -450.36
  212 PY -450.37
  213 PY -450.467
  214 PY -450.569
C    Cylinders to define foils
  304 10 CY      0.6
  305 10 CY      1.0
  306 10 CY      1.1

C
C    Transformation cards for fuel rods
 *TR1  0.0   0.0   0.0       45.0 -45.0  90.0 135.0  45.0  90.0
 *TR2  0.0   0.0   0.0       60.0 -30.0  90.0 150.0  60.0  90.0
 *TR3  0.0   0.0   0.0       75.0 -15.0  90.0 165.0  75.0  90.0
 *TR4  0.0   0.0   0.0      105.0  15.0  90.0 195.0 105.0  90.0
 *TR5  0.0   0.0   0.0      120.0  30.0  90.0 210.0 120.0  90.0
C    Transformation cards for D2, D3, D1 and D4
 *TR6   53.5   53.5   0.0
 *TR7   53.5  -53.5   0.0
```

```
 *TR8  -53.5   53.5   0.0
 *TR9  -53.5  -53.5   0.0
C    Transformation card for collimators in beam tube HN
 TR10 -40.64   0.0   0.0
C
C
C     M A T E R I A L - definition
C     ============================
C
M1    6012.35C  -98.8    6013.35C   -1.2                  $ graphite
M2    82000.35C   -1.0                                    $ lead
M3    7014.04C  -77.0    8016.35C  -22.9
       1001.35C  -0.00114                      $ air 70% vochtigheid
C     M4
C     materials for VC
M5    13027.35C  -99.8    7014.04C  -.153    8016.35C   -.047
M6     6012.35C  -69.31   6013.35C   -.84   13027.35C  -29.32
      26000.35C  -.392   28000.11C  -.043   24000.35C  -.095
M7    13027.35C  -99.98   7014.04C  -.0153   8016.35C  -.0047
C     materials 1-plate core
M8    13027.35C  -37.17   6012.35C  -21.83   6013.35C  -.26
       1001.35C   -4.28   8016.35C  -33.88
      92235.11D   -2.29  92238.35C  -.28
C     materials graphite ring
M9    13027.35C  -5.57    6012.35C  -87.09   6013.35C  -1.06
       1001.35C  -.70     8016.35C  -5.58
C     materials above fuel
M10   13027.35C  -17.7    6012.35C  -18.9    6013.35C  -0.2
       1001.35C  -7.1     8016.35C  -56.1
C     materials below fuel
M11   13027.35C  -40.3    6012.35C  -14.9    6013.35C  -0.2
       1001.35C  -5.0     8016.35C  -39.6
C     materials above graphite blocks
M12   13027.35C  -12.4    6012.35C  -19.6    6013.35C  -0.2
       1001.35C  -7.6     8016.35C  -60.2
C     materials below graphite blocks
M13   13027.35C  -41.6    6012.35C  -6.7     6013.35C  -0.1
       1001.35C  -5.8     8016.35C  -45.8
C     material above core ring
M14   13027.35C  -10.9    1001.35C  -10.0    8016.35C  -79.1
C     material above H2O
M15   13027.35C  -99.02   7014.04C  -.75     8016.35C   -.23
C     material below core ring
M16   13027.35C  -23.0    1001.35C  -8.6     8016.35C  -68.4
C     materials below inner vessel
M17   13027.35C  -84.4    1001.35C  -1.75    8016.35C  -13.85
M18   13027.35C  -57.4    1001.35C  -4.8     8016.35C  -37.8
C     material for Al-construction arround reflector
M19   13027.35C  -99.72   7014.04C  -.21     8016.35C  -.07
C     materials for P4 + P6  (P2 + P5)
M20   13027.35C  -99.7    7014.04C  -.23     8016.35C  -.07
M21   13027.35C  -95.23  48000.35C  -4.77
C     materials for P2 + P5
M22   13027.35C  -99.05   7014.04C  -.0075   8016.35C  -.0025
      48000.35C  -0.94
C     materials for D2 + D4
M23   13027.35C  -88.4    7014.04C  -.53     8016.35C  -.17
       5010.03C  -10.9
M24   26000.35C  -3.47   24000.35C  -.84    28000.11C  -.37
      82000.35C  -94.87  48000.35C  -.38
       7014.04C  -.053    8016.35C  -.017
C     materials for barytes concrete
M25   56138.35C  -32.0   26000.35C  -14.0    8016.35C  -38.0
      20000.35C  -6.0    16032.35C  -8.0     1001.35C  -1.0
      14000.35C  -1.0
C     materials for iron scrap concrete
M26   26000.35C  -89.0    8016.35C  -6.0    20000.35C  -4.0
      14000.35C  -1.0
C     materials for wagon BIBOP
M27   26000.35C  -99.94   8016.35C  -.014    7014.04C  -.046
C
C
M34   48000.35C  -1.0                                    $ Cadmium
```

```
M35   5010.03C -1.0  5011.35C -4.0  1001.35C -13.62
                     6012.35C  -81.38                          $ Polyboron
C     materials for sand
M36   14000.35C  -39.0   13027.35C  -3.5    8016.35C  -51.0
      20000.35C  -1.2    26000.35C  -1.4     1001.35C  -0.5
      11023.35C  -2.0   19000.35C -1.4
C     iron
M37   26000.35C  -94.0   6012.35C -4.0   14000.35C  -2.0
C
M41   13027.03C -0.99   79197.35C -0.01                            $ Al/Au
M42   13027.03C -0.998  49115.03C -0.001915  49113.03C -0.000085 $ Al/In
M43   21045.26Y  1.0                                              $ Pure Sc
M44   13027.03C -0.99   74182.03C -0.00261   74183.03C -0.00143  $ Al/W
      74184.03C -0.00306 74186.03C -0.00287
M45   13027.03C -0.77   92238.35C -0.2284    92235     -0.00165  $ Al/U238
M46   13027.03C -0.99   25055.03C -0.01                           $ Al/Mn
M47   13027.03C -0.90   29000.03C -0.10                           $ Al/Cu
M48   49115.03C  0.957  49113.03C 0.043                          $ In
M49   28000.03C  1.0                                            $ Ni
M50   13027.03C  1.0                                            $ Al
M51   48000.03C  1.0                                            $ Cd
M52   79197.35C  1.0                                        $ Pure Au197
M53   74186.03C  1.0                                        $ Pure W186
M54   92238.35C  1.0                                        $ Pure U238
M55   57139.26Y  1.0                                        $ Pure La139
M56   25055.03C  1.0                                        $ Pure Mn55
M57   29063.26Y  1.0                                        $ Pure Cu63
M58   49115.03C  1.0                                        $ Pure In115
M59   28058.35C  1.0                                        $ Pure Ni58
C
M63    8016.03C 0.2  7014.03C 0.8                                $ Air
C
C     S(a,b)-specification for H2O + graphite
MT1   GRPH.01T
MT6   GRPH.01T
MT8   LWTR.01T
MT9   GRPH.01T
MT10  LWTR.01T
MT11  LWTR.01T
MT12  LWTR.01T
MT13  LWTR.01T
MT14  LWTR.01T
MT16  LWTR.01T
MT17  LWTR.01T
MT18  LWTR.01T
C
C
C    S O U R C E  definition
C    ======================
C
SDEF  ERG=D1  RAD=D2  EXT=D3  CEL=D4  POS=0 0 0  AXS=0 0 1
C
SP1   -3  0.988 2.249
C
SI2   30.4  46.4
C
SI3  A  -30    -20    -10     0     10     20     30
SP3     0.75   1.05   1.4    1.5   1.33    1.0   0.65
C
SI4  L   24    25    26    27    28
SP4     0.69  0.95  1.0   0.91  0.69
C
C     G E N E R A L  program data
C     ===========================
C
MODE  N
C
NONU
C
WWP:N 5 3 5
WWE:N   5.0000E-02  2.0000E+01
WWN1:N  -1.0000E+00 -1.0000E+00 -1.0000E+00 -1.0000E+00 -1.0000E+00
         -1.0000E+00  0.0000E+00  0.0000E+00 -1.0000E+00 -1.0000E+00
```

```
          0.0000E+00  1.7129E+01  5.6897E+00  1.9274E+01  8.5428E+00
          9.8612E+00  1.5816E+00  3.3557E-01  1.5914E+00  1.6040E+01  $ 20
          8.7947E+02  0.0000E+00  0.0000E+00  3.6213E-01  2.2062E+00
          2.9480E+00  9.5464E+00  2.0000E+01  4.0000E+01  4.4699E-01
          4.0000E+00  6.0000E+00  8.0000E+00  1.5000E+01  0.0000E+00
          5.0000E-01  4.0000E+00  6.0000E+00  8.0000E+00  1.5000E+01  $ 40
         -1.0000E+00  0.0000E+00  0.0000E+00 -1.0000E+00 -1.0000E+00
         -1.0000E+00 -1.0000E+00 -1.0000E+00 -1.0000E+00 -1.0000E+00
         -1.0000E+00 -1.0000E+00  0.0000E+00  0.0000E+00 -1.0000E+00
         -1.0000E+00 -1.0000E+00 -1.0000E+00 -1.0000E+00 -1.0000E+00  $ 60
         -1.0000E+00 -1.0000E+00 -1.0000E+00 -1.0000E+00 -1.0000E+00
         -1.0000E+00 -1.0000E+00 -1.0000E+00 -1.0000E+00 -1.0000E+00
         -1.0000E+00 -1.0000E+00 -1.0000E+00  2.0000E+01  2.0000E+01
         -1.0000E+00 -1.0000E+00 -1.0000E+00 -1.0000E+00 -1.0000E+00  $ 80
         -1.0000E+00 -1.0000E+00  2.2846E-01  1.0310E-01  2.0000E+00
          1.0000E+00  0.0000E+00  1.0087E+00  0.0000E+00  0.0000E+00
          0.0000E+00  0.0000E+00  0.0000E+00  0.0000E+00 -1.0000E+00
         -1.0000E+00 -1.0000E+00  0.0000E+00  0.0000E+00  2.5916E+00  $ 100
          8.0000E-01  0.0000E+00  2.6282E-01  8.8458E-02  2.2781E-01
         -1.0000E+00 -1.0000E+00 -1.0000E+00  5.0000E-01  4.0000E-01
          6.0000E-01  2.7014E+00  1.6994E-01  6.6603E+00  0.0000E+00
         -1.0000E+00 -1.0000E+00 -1.0000E+00  9.0308E-02  6.8473E-02  $ 120
         -1.0000E+00 -1.0000E+00 -1.0000E+00 -1.0000E+00 -1.0000E+00
         -1.0000E+00 -1.0000E+00  1.0000E-01  1.0000E+00  7.0000E-02
          3.0000E+00  1.3398E-01  1.9198E-01  1.6420E-01  2.8552E-01
         -1.0000E+00 -1.0000E+00  3.0000E-01  5.0000E-01 -1.0000E+00  $ 140
         -1.0000E+00 -1.0000E+00  1.4735E-01 -1.0000E+00 -1.0000E+00
          1.1644E+00  0.0000E+00  0.0000E+00  0.0000E+00 -1.0000E+00
          4.2875E-01 -1.0000E+00 -1.0000E+00 -1.0000E+00 -1.0000E+00
         -1.0000E+00 -1.0000E+00 -1.0000E+00 -1.0000E+00 -1.0000E+00  $ 160
         -1.0000E+00 -1.0000E+00  5.4486E-01  6.0000E-01  0.0000E+00
          0.0000E+00 -1.0000E+00 -1.0000E+00 -1.0000E+00 -1.0000E+00
          6.5171E-01  0.0000E+00  0.0000E+00  5.7577E-01  0.0000E+00
          0.0000E+00 -1.0000E+00  0.0000E+00  0.0000E+00  2.0000E-03  $ 180
          1.5000E-03  8.0000E-04  4.0000E-04  3.0000E-04  2.0000E-04
          1.5000E-04  9.0000E-05  4.0000E-05  2.0000E-05  1.5000E-05
          8.0000E-06  0.0000E-06  0.0000E+00  8.0000E-02  4.0000E-02
          8.0000E-03  6.0000E-04  3.0000E-04  1.0000E-04  4.0000E-05  $ 200
          2.7303E-02  2.8984E-02  2.6282E-02  9.2461E-03  3.0000E-02
          1.4590E-02  3.0000E-02  1.7898E-02  3.0000E-02  4.2216E-02
          6.9478E-02  4.0160E-02  8.4173E-02  1.2714E-03  1.0000E-03
          3.0000E-04  1.0000E-04  4.0000E-05  2.0000E-05  2.0000E-05  $ 220
          1.5000E-05  1.5000E-05  2.0000E-04  1.5000E-04  2.0000E-04
          0.0000E+00  2.0000E-03  3.0000E-04  1.5000E-04  8.0000E-05
          4.0E-05     0           2.0E-04     2.0E-04     2.0E-04
          2.0E-04     2.0E-04     2.0E-04     2.0E-04     2.0E-04
          2.0E-04     2.0E-04     2.0E-04     2.0E-04     2.0E-04
          2.0E-04     2.0E-04     2.0E-04     2.0E-04     0
WWN2:N   -1.0000E+00 -1.0000E+00 -1.0000E+00 -1.0000E+00 -1.0000E+00
         -1.0000E+00  0.0000E+00  3.3046E-01 -1.0000E+00 -1.0000E+00
          0.0000E+00  1.9599E-01  9.8983E-02  3.6894E-01  5.9170E+00
          7.8665E-01  7.4800E-02  2.7052E-02  1.6084E-01  9.4288E-01
          6.2103E+00  0.0000E+00  0.0000E+00  4.6371E-02  1.5532E-01
          5.0000E-01  1.6256E+00  2.8697E+00  7.7248E+00  1.7967E-01
          4.6311E-01  1.8541E-01  7.3724E-01  0.0000E+00  0.0000E+00
          5.5097E-01  1.1058E+00  7.8930E-01  9.5260E-01  0.0000E+00
         -1.0000E+00  1.8253E+01  0.0000E+00 -1.0000E+00 -1.0000E+00
         -1.0000E+00 -1.0000E+00 -1.0000E+00 -1.0000E+00 -1.0000E+00
         -1.0000E+00 -1.0000E+00  0.0000E+00  0.0000E+00 -1.0000E+00
         -1.0000E+00 -1.0000E+00 -1.0000E+00 -1.0000E+00 -1.0000E+00
         -1.0000E+00 -1.0000E+00 -1.0000E+00 -1.0000E+00 -1.0000E+00
         -1.0000E+00 -1.0000E+00 -1.0000E+00 -1.0000E+00 -1.0000E+00
         -1.0000E+00 -1.0000E+00 -1.0000E+00  1.5752E+01  1.8000E+01
         -1.0000E+00 -1.0000E+00 -1.0000E+00 -1.0000E+00 -1.0000E+00
         -1.0000E+00 -1.0000E+00  3.2227E-02  1.8152E-02  1.0497E-01
          1.9252E-01  0.0000E+00  1.9028E-01  2.1396E-01  1.3949E-01
          0.0000E+00  0.0000E+00  0.0000E+00  0.0000E+00  0.0000E+00
          0.0000E+00  0.0000E+00  0.0000E+00  0.0000E+00  2.6795E+00
          6.5998E-01  0.0000E+00  1.1286E-01  2.8192E-02  6.7213E-02
         -1.0000E+00 -1.0000E+00 -1.0000E+00  2.5052E-01  2.2163E-01
          1.1520E-01  4.7344E-01  5.5324E-02  9.8140E-01  0.0000E+00
         -1.0000E+00 -1.0000E+00 -1.0000E+00  1.8284E-02  2.2056E-02
         -1.0000E+00 -1.0000E+00 -1.0000E+00 -1.0000E+00 -1.0000E+00
```

```
          -1.0000E+00 -1.0000E+00  8.0000E-02  9.2277E-01  5.0000E-02
           8.1499E-01  2.9143E-02  3.2457E-02  6.1925E-02  3.3900E-02
          -1.0000E+00 -1.0000E+00  4.0000E-02  6.0000E-02 -1.0000E+00
          -1.0000E+00 -1.0000E+00  7.6165E-02 -1.0000E+00 -1.0000E+00
           3.0477E+00  0.0000E+00  0.0000E+00  0.0000E+00 -1.0000E+00
           8.8374E-02 -1.0000E+00 -1.0000E+00 -1.0000E+00 -1.0000E+00
          -1.0000E+00 -1.0000E+00 -1.0000E+00 -1.0000E+00 -1.0000E+00
          -1.0000E+00 -1.0000E+00  1.0638E-01  9.0853E-02  0.0000E+00
           0.0000E+00 -1.0000E+00 -1.0000E+00 -1.0000E+00 -1.0000E+00
           1.0312E-01  0.0000E+00  0.0000E+00  1.2307E-01  0.0000E+00
           0.0000E+00 -1.0000E+00  0.0000E+00  0.0000E+00  2.0000E-03  $ 180
           1.5000E-03  8.0000E-04  4.0000E-04  3.0000E-04  2.0000E-04
           1.5000E-04  9.0000E-05  4.0000E-05  2.0000E-05  1.5000E-05
           8.0000E-06  0.0000E-06  0.0000E+00  8.0000E-02  4.0000E-02
           8.0000E-03  6.0000E-04  3.0000E-04  1.0000E-04  4.0000E-05  $ 200
           1.3744E-02  1.4233E-02  1.2876E-02  5.1239E-03  7.2472E-03
           6.7562E-03  7.3247E-03  6.1455E-03  8.0000E-03  1.2170E-02
           3.0000E-02  1.8068E-02  3.4743E-02  6.8104E-04  1.0000E-03
           3.0000E-04  1.0000E-04  4.0000E-05  2.0000E-05  2.0000E-05  $ 220
           1.5000E-05  1.5000E-05  2.0000E-04  1.5000E-04  2.0000E-04
           0.0000E+00  2.0000E-03  3.0000E-04  1.5000E-04  8.0000E-05
           4.0E-05     0           2.0E-04     2.0E-04     2.0E-04
           2.0E-04     2.0E-04     2.0E-04     2.0E-04     2.0E-04
           2.0E-04     2.0E-04     2.0E-04     2.0E-04     2.0E-04
           2.0E-04     2.0E-04     2.0E-04     2.0E-04     0
C
DXT:N -40.64 -449.8 0  1.5  1.5
DXC:N 0 1 248R
DD   .1
C
PRDMP  -60   -20
PRINT  126 150 170
DBCN  97
FQ0   E M
PHYS:N 20 1E-6
C
C     TALLY DEFINITION
C     ================
C
C       Fluxen over opp  200
C
F22:N  200
E22   2.53E-8  1.00E-7  4.14E-7  8.76E-7  1.86E-6  5.04E-6
      1.07E-5  3.73E-5  1.01E-4  2.15E-4  4.54E-4  1.58E-3
      3.35E-3  7.10E-3  1.50E-2  2.19E-2  2.42E-2  2.61E-2
      3.18E-2  4.07E-2  6.74E-2  1.11E-1  1.83E-1  2.97E-1
      3.69E-1  4.98E-1  6.08E-1  7.43E-1  8.21E-1  1.00E+0
      1.35E+0  1.65E+0  1.92E+0  2.23E+0  2.35E+0  2.37E+0
      2.47E+0  2.72E+0  3.01E+0  3.68E+0  4.97E+0  6.07E+0
      7.41E+0  8.61E+0  1.00E+1  1.22E+1  1.42E+1  1.73E+1
FM22   2.278E+15
C
F12:N  108
E12   2.53E-8  1.00E-7  4.14E-7  8.76E-7  1.86E-6  5.04E-6
      1.07E-5  3.73E-5  1.01E-4  2.15E-4  4.54E-4  1.58E-3
      3.35E-3  7.10E-3  1.50E-2  2.19E-2  2.42E-2  2.61E-2
      3.18E-2  4.07E-2  6.74E-2  1.11E-1  1.83E-1  2.97E-1
      3.69E-1  4.98E-1  6.08E-1  7.43E-1  8.21E-1  1.00E+0
      1.35E+0  1.65E+0  1.92E+0  2.23E+0  2.35E+0  2.37E+0
      2.47E+0  2.72E+0  3.01E+0  3.68E+0  4.97E+0  6.07E+0
      7.41E+0  8.61E+0  1.00E+1  1.22E+1  1.42E+1  1.73E+1
FM12   2.278E+15
SF12  200
C
C
C      Foil activation tallies
C
E0   4.14E-7 1.00E-2 1.45E+1
C
FC4  Gold activation in the Al/Au foils
F4:N  236 239
FM4  (2.278E+15)
     (2.278E-09 52 102)
```

```
SF4  305
FC14 Indium activation in the Al/In foil
F14:N 237
FM14 (2.278E+15)
     (2.278E-09 58 102)
FC24 Scandium activation in the Al/Sc foil
F24:N 238
FM24 (2.278E+15)
     (2.278E-09 43 102)
SF24 305
FC34 Tungsten activation in the Al/W foil
F34:N 240
FM34 (2.278E+15)
     (2.278E-09 53 102)
SF34 114
FC44 U238 activation in the U238/Al foil
F44:N 241
FM44 (2.278E+15)
     (2.278E-09 54 102)
SF44  305
FC54 Lanthanum activation in the Al/La foil
F54:N 242
FM54 (2.278E+15)
     (2.278E-09 55 102)
FC64 Manganese activation in the Al/Mn foil
F64:N 243
FM64 (2.278E+15)
     (2.278E-09 56 102)
SF64 305
FC74 Copper-63 activation in the Al/Cu foil
F74:N 244
FM74 (2.278E+15)
     (2.278E-09 57 102)
FC84 Indium (n,n') in pure In foil
F84:N 245
FM84 (2.278E+15)
     (2.278E-09 58  51:52:53:54:55:91)
FC94 Nickel (n,p) activation in Ni foil.
F94:N 246
FM94 (2.278E+15)
     (2.278E-09 59 103)
SF94 305
FC104 Aluminium (n,alpha) activation in Al foil
F104:N 247
FM104 (2.278E+15)
      (2.278E-09 50 107)
SF104 114
C
C
NPS   2000000
CTME  1200
EOF
#
mcnp4A >  lfr103.out
cat outp >> lfr103.out
#
\rm  end185 532dos tmccs bmccs leff13 xsdir d9
\rm inp outp
#
```

APPENDIX B. DORT INPUT FILE OF THE HEAD PHANTOM

```
*begin

*rpasc dort  -lin1 gip1.gip.outlib1 -lin2 ijkdort1.nflux  -lout1 nflux

*data
TITEL MCNP4A supplied source, from lfr103c, corrected for foils
61$$  4    2    8    0    0
      0    0    0    0    1
      0
  E
62$$  0    3    3   36   96
     67    3    4   70   36
      0   36   52    0   96
      1    1    0    0    4
     10   10    0    4    0
      2    0    0    0    0
      0    0    0    0    1
      3    0    0    1    2
      0    0    0    0    0
      0    1    1    1    1
      4  100    0    0    4
      1    1    0    0    0
      0   -1    0    0    0
      4   47
  E
63** 0.0      0    1.0E-4 1.0E-3  1.0E-3
     1.0E-3 1.0    0.2    1.5    10.0
     1.0    1.0   -1.0    0.3    10.0
     1.0    1.0E-4 1.0E-2 0.3    -1.5
     1.5    0.6    0.0    1.0E-30 0.0
     1.0E-3 0.1    0.9
  E
T
T
81**
          0  2R+18643-6          0    +13760-6  2R+13760-6    +13760-6
          0    +98031-7    +98912-7  2R+98031-7    +98912-7    +98031-7
          0    +98031-7    +76720-7    +76720-7  2R+98031-7    +76720-7
   +76720-7    +98031-7          0    +13760-6    +98912-7    +76720-7
   +98912-7  2R+13760-6    +98912-7    +76720-7    +98912-7    +13760-6
          0    +18643-6    +13760-6    +98031-7    +98031-7    +13760-6
 2R+18643-6    +13760-6    +98031-7    +98031-7    +13760-6    +18643-6
          0  2R+18643-6          0    +13760-6  2R+13760-6    +13760-6
          0    +98031-7    +98912-7  2R+98031-7    +98912-7    +98031-7
          0    +98031-7    +76720-7    +76720-7  2R+98031-7    +76720-7
   +76720-7    +98031-7          0    +13760-6    +98912-7    +76720-7
   +98912-7  2R+13760-6    +98912-7    +76720-7    +98912-7    +13760-6
          0    +18643-6    +13760-6    +98031-7    +98031-7    +13760-6
 2R+18643-6    +13760-6    +98031-7    +98031-7    +13760-6    +18643-6
82**
   -24618-5    -17408-5    +17408-5    -49237-5    -46057-5    -17408-5
   +17408-5    +46057-5    -65134-5    -62765-5    -46057-5    -17408-5
   +17408-5    +46057-5    +62765-5    -77850-5    -75879-5    -62765-5
   -46057-5    -17408-5    +17408-5    +46057-5    +62765-5    +75879-5
   -88763-5    -87039-5    -75879-5    -62765-5    -46057-5    -17408-5
   +17408-5    +46057-5    +62765-5    +75879-5    +87039-5    -98473-5
   -96922-5    -87039-5    -75879-5    -62765-5    -46057-5    -17408-5
   +17408-5    +46057-5    +62765-5    +75879-5    +87039-5    +96922-5
   -24618-5    -17408-5    +17408-5    -49237-5    -46057-5    -17408-5
   +17408-5    +46057-5    -65134-5    -62765-5    -46057-5    -17408-5
   +17408-5    +46057-5    +62765-5    -77850-5    -75879-5    -62765-5
   -46057-5    -17408-5    +17408-5    +46057-5    +62765-5    +75879-5
   -88763-5    -87039-5    -75879-5    -62765-5    -46057-5    -17408-5
   +17408-5    +46057-5    +62765-5    +75879-5    +87039-5    -98473-5
   -96922-5    -87039-5    -75879-5    -62765-5    -46057-5    -17408-5
   +17408-5    +46057-5    +62765-5    +75879-5    +87039-5    +96922-5
```

```
83**
 3R-96922-5  5R-87039-5  7R-75879-5  9R-62765-5 11R-46057-5 13R-17408-5
 3R+96922-5  5R+87039-5  7R+75879-5  9R+62765-5 11R+46057-5 13R+17408-5
T
1** F0
2**  95I  0    24
4**  35I  0     9
5**  1.730E+07  1.420E+07  1.220E+07  1.000E+07  8.610E+06  7.410E+06
     6.070E+06  4.970E+06  3.680E+06  3.010E+06  2.720E+06  2.470E+06
     2.370E+06  2.350E+06  2.230E+06  1.920E+06  1.650E+06  1.350E+06
     1.000E+06  8.210E+05  7.430E+05  6.080E+05  4.980E+05  3.690E+05
     2.970E+05  1.830E+05  1.110E+05  6.740E+04  4.070E+04  3.180E+04
     2.610E+04  2.420E+04  2.190E+04  1.500E+04  7.100E+03  3.350E+03
     1.580E+03  4.540E+02  2.150E+02  1.010E+02  3.730E+01  1.070E+01
     5.040E+00  1.860E+00  8.760E-01  4.140E-01  1.000E-01  1.000E-05
     1.400E+07  1.000E+07  8.000E+06  7.000E+06  6.000E+06  5.000E+06
     4.000E+06  3.000E+06  2.000E+06  1.500E+06  1.000E+06  8.000E+05
     7.000E+05  6.000E+05  4.000E+05  2.000E+05  1.000E+05  6.000E+04
     3.000E+04  2.000E+04  1.000E+04
8$$  32R1  4R3 59Q36
     32R1  4R3 4Q36
     31R1  5R3 3Q36
     30R1  6R3 2Q36
     29R1  7R3 1Q36
     4R2  24R1  8R3 1Q36
     4R2  23R1  9R3 1Q36
     4R2  22R1  10R3 1Q36
     4R2  20R1  12R3 1Q36
     23R1  13R3
     22R1  14R3
     20R1  16R3 1Q36
     18R1  18R3
     16R1  20R3
     14R1  22R3
     12R1  24R3
     9R1  27R3
     5R1  31R3
     36R3 3Q36
9$$   -41  -45  -49
10$$   3R41  3R42  3R43  3R44
       3R45  3R46  3R47  3R48
       3R49  3R50  3R51  3R52
11$$   1  5  9    2  6  10    3  7  11    4  8  12
       1  5  9    2  6  10    3  7  11    4  8  12
       9 17  1   10 18   2   11 19   3   12 20   4
12**   6.69E-2        0  3.34E-2   3Q3
       6.69E-2  3.74E-6  3.34E-2   3Q3
       1.00E-5  4.40E-5  7.40E-7   3Q3
25$$   5
26$$   1
T
92** 3R  0. 93R0. 17Q96   3R  0. 93R0.  3Q96
     3R  0. 93R0.  3Q96   3R  0. 93R0.  3Q96
     3R  0. 93R0.  5Q96   F0. T
92** 3R  0. 93R0. 17Q96   3R  0. 93R0.  3Q96
     3R  0. 93R0.  3Q96   3R  0. 93R0.  3Q96
     3R  0. 93R0.  5Q96   F0. T
92** 3R    15.6518 93R0. 17Q96   3R    13.7736 93R0.  3Q96
     3R    12.0519 93R0.  3Q96   3R   10.33019 93R0.  3Q96
     3R    8.60849 93R0.  5Q96   F0. T
92** 3R    369.160 93R0. 17Q96   3R    324.861 93R0.  3Q96
     3R    284.253 93R0.  3Q96   3R    243.646 93R0.  3Q96
     3R    203.038 93R0.  5Q96   F0. T
92** 3R    546.887 93R0. 17Q96   3R    481.261 93R0.  3Q96
     3R    421.103 93R0.  3Q96   3R    360.945 93R0.  3Q96
     3R    300.788 93R0.  5Q96   F0. T
92** 3R    2689.62 93R0. 17Q96   3R    2366.87 93R0.  3Q96
     3R    2071.01 93R0.  3Q96   3R    1775.15 93R0.  3Q96
     3R    1479.29 93R0.  5Q96   F0. T
92** 3R    8015.83 93R0. 17Q96   3R    7053.93 93R0.  3Q96
     3R    6172.19 93R0.  3Q96   3R    5290.45 93R0.  3Q96
     3R    4408.71 93R0.  5Q96   F0. T
92** 3R    20937.3 93R0. 17Q96   3R    18424.8 93R0.  3Q96
```

```
     3R    16121.7 93R0.  3Q96   3R    13818.6 93R0.  3Q96
     3R    11515.5 93R0.  5Q96   F0. T
92** 3R    24360.3 93R0. 17Q96   3R    21437.1 93R0.  3Q96
     3R    18757.4 93R0.  3Q96   3R    16077.8 93R0.  3Q96
     3R    13398.2 93R0.  5Q96   F0. T
92** 3R    15259.6 93R0. 17Q96   3R    13428.4 93R0.  3Q96
     3R    11749.9 93R0.  3Q96   3R   10071.34 93R0.  3Q96
     3R    8392.78 93R0.  5Q96   F0. T
92** 3R    20744.7 93R0. 17Q96   3R    18255.3 93R0.  3Q96
     3R    15973.4 93R0.  3Q96   3R    13691.5 93R0.  3Q96
     3R    11409.6 93R0.  5Q96   F0. T
92** 3R    12744.9 93R0. 17Q96   3R    11215.5 93R0.  3Q96
     3R    9813.57 93R0.  3Q96   3R    8411.63 93R0.  3Q96
     3R    7009.70 93R0.  5Q96   F0. T
92** 3R    2436.77 93R0. 17Q96   3R    2144.36 93R0.  3Q96
     3R    1876.31 93R0.  3Q96   3R    1608.27 93R0.  3Q96
     3R    1340.22 93R0.  5Q96   F0. T
92** 3R    18865.3 93R0. 17Q96   3R    16601.5 93R0.  3Q96
     3R    14526.3 93R0.  3Q96   3R    12451.1 93R0.  3Q96
     3R   10375.92 93R0.  5Q96   F0. T
92** 3R    54844.2 93R0. 17Q96   3R    48262.9 93R0.  3Q96
     3R    42230.0 93R0.  3Q96   3R    36197.2 93R0.  3Q96
     3R    30164.3 93R0.  5Q96   F0. T
92** 3R    66652.0 93R0. 17Q96   3R    58653.8 93R0.  3Q96
     3R    51322.0 93R0.  3Q96   3R    43990.3 93R0.  3Q96
     3R    36658.6 93R0.  5Q96   F0. T
92** 3R   100293.8 93R0. 17Q96   3R    88258.5 93R0.  3Q96
     3R    77226.2 93R0.  3Q96   3R    66193.9 93R0.  3Q96
     3R    55161.6 93R0.  5Q96   F0. T
92** 3R    159417. 93R0. 17Q96   3R    140287. 93R0.  3Q96
     3R    122751. 93R0.  3Q96   3R   105215.2 93R0.  3Q96
     3R    87679.4 93R0.  5Q96   F0. T
92** 3R    108696. 93R0. 17Q96   3R    95652.5 93R0.  3Q96
     3R    83695.9 93R0.  3Q96   3R    71739.4 93R0.  3Q96
     3R    59782.8 93R0.  5Q96   F0. T
92** 3R    54844.1 93R0. 17Q96   3R    48262.8 93R0.  3Q96
     3R    42230.0 93R0.  3Q96   3R    36197.1 93R0.  3Q96
     3R    30164.3 93R0.  5Q96   F0. T
92** 3R    108117. 93R0. 17Q96   3R    95143.0 93R0.  3Q96
     3R    83250.1 93R0.  3Q96   3R    71357.2 93R0.  3Q96
     3R    59464.4 93R0.  5Q96   F0. T
92** 3R    108251. 93R0. 17Q96   3R    95260.9 93R0.  3Q96
     3R    83353.3 93R0.  3Q96   3R    71445.7 93R0.  3Q96
     3R    59538.1 93R0.  5Q96   F0. T
92** 3R    149530. 93R0. 17Q96   3R    131586. 93R0.  3Q96
     3R    115138. 93R0.  3Q96   3R    98689.8 93R0.  3Q96
     3R    82241.5 93R0.  5Q96   F0. T
92** 3R   105314.9 93R0. 17Q96   3R    92677.1 93R0.  3Q96
     3R    81092.5 93R0.  3Q96   3R    69507.8 93R0.  3Q96
     3R    57923.2 93R0.  5Q96   F0. T
92** 3R    230683. 93R0. 17Q96   3R    203001. 93R0.  3Q96
     3R    177626. 93R0.  3Q96   3R    152251. 93R0.  3Q96
     3R    126876. 93R0.  5Q96   F0. T
92** 3R    219859. 93R0. 17Q96   3R    193476. 93R0.  3Q96
     3R    169291. 93R0.  3Q96   3R    145107. 93R0.  3Q96
     3R    120922. 93R0.  5Q96   F0. T
92** 3R    208185. 93R0. 17Q96   3R    183203. 93R0.  3Q96
     3R    160302. 93R0.  3Q96   3R    137402. 93R0.  3Q96
     3R    114502. 93R0.  5Q96   F0. T
92** 3R    202033. 93R0. 17Q96   3R    177789. 93R0.  3Q96
     3R    155565. 93R0.  3Q96   3R    133342. 93R0.  3Q96
     3R    111118. 93R0.  5Q96   F0. T
92** 3R    92537.2 93R0. 17Q96   3R    81432.7 93R0.  3Q96
     3R    71253.6 93R0.  3Q96   3R    61074.6 93R0.  3Q96
     3R    50895.5 93R0.  5Q96   F0. T
92** 3R    68520.1 93R0. 17Q96   3R    60297.7 93R0.  3Q96
     3R    52760.5 93R0.  3Q96   3R    45223.3 93R0.  3Q96
     3R    37686.1 93R0.  5Q96   F0. T
92** 3R    28263.3 93R0. 17Q96   3R    24871.7 93R0.  3Q96
     3R    21762.7 93R0.  3Q96   3R    18653.8 93R0.  3Q96
     3R    15544.8 93R0.  5Q96   F0. T
92** 3R    37272.2 93R0. 17Q96   3R    32799.5 93R0.  3Q96
     3R    28699.6 93R0.  3Q96   3R    24599.7 93R0.  3Q96
```

```
     3R    20499.7 93R0.  5Q96   F0. T
92** 3R    135843. 93R0. 17Q96   3R    119542. 93R0.  3Q96
     3R   104599.1 93R0.  3Q96   3R    89656.4 93R0.  3Q96
     3R    74713.6 93R0.  5Q96   F0. T
92** 3R    257961. 93R0. 17Q96   3R    227006. 93R0.  3Q96
     3R    198630. 93R0.  3Q96   3R    170254. 93R0.  3Q96
     3R    141879. 93R0.  5Q96   F0. T
92** 3R    262752. 93R0. 17Q96   3R    231222. 93R0.  3Q96
     3R    202319. 93R0.  3Q96   3R    173416. 93R0.  3Q96
     3R    144514. 93R0.  5Q96   F0. T
92** 3R    249343. 93R0. 17Q96   3R    219422. 93R0.  3Q96
     3R    191994. 93R0.  3Q96   3R    164566. 93R0.  3Q96
     3R    137139. 93R0.  5Q96   F0. T
92** 3R    408062. 93R0. 17Q96   3R    359095. 93R0.  3Q96
     3R    314208. 93R0.  3Q96   3R    269321. 93R0.  3Q96
     3R    224434. 93R0.  5Q96   F0. T
92** 3R    236009. 93R0. 17Q96   3R    207688. 93R0.  3Q96
     3R    181727. 93R0.  3Q96   3R    155766. 93R0.  3Q96
     3R    129805. 93R0.  5Q96   F0. T
92** 3R    243859. 93R0. 17Q96   3R    214596. 93R0.  3Q96
     3R    187771. 93R0.  3Q96   3R    160947. 93R0.  3Q96
     3R    134122. 93R0.  5Q96   F0. T
92** 3R    307101. 93R0. 17Q96   3R    270249. 93R0.  3Q96
     3R    236468. 93R0.  3Q96   3R    202687. 93R0.  3Q96
     3R    168906. 93R0.  5Q96   F0. T
92** 3R    393067. 93R0. 17Q96   3R    345899. 93R0.  3Q96
     3R    302662. 93R0.  3Q96   3R    259424. 93R0.  3Q96
     3R    216187. 93R0.  5Q96   F0. T
92** 3R    237854. 93R0. 17Q96   3R    209312. 93R0.  3Q96
     3R    183148. 93R0.  3Q96   3R    156984. 93R0.  3Q96
     3R    130820. 93R0.  5Q96   F0. T
92** 3R    313410. 93R0. 17Q96   3R    275801. 93R0.  3Q96
     3R    241326. 93R0.  3Q96   3R    206851. 93R0.  3Q96
     3R    172376. 93R0.  5Q96   F0. T
92** 3R    224091. 93R0. 17Q96   3R    197200. 93R0.  3Q96
     3R    172550. 93R0.  3Q96   3R    147900. 93R0.  3Q96
     3R    123250. 93R0.  5Q96   F0. T
92** 3R    132405. 93R0. 17Q96   3R    116516. 93R0.  3Q96
     3R   101951.8 93R0.  3Q96   3R    87387.3 93R0.  3Q96
     3R    72822.8 93R0.  5Q96   F0. T
92** 3R    3713.52 93R0. 17Q96   3R    3267.90 93R0.  3Q96
     3R    2859.41 93R0.  3Q96   3R    2450.92 93R0.  3Q96
     3R    2042.44 93R0.  5Q96   F0. T
92** 3R    664.047 93R0. 17Q96   3R    584.361 93R0.  3Q96
     3R    511.316 93R0.  3Q96   3R    438.271 93R0.  3Q96
     3R    365.226 93R0.  5Q96   F0. T
92**  F0. T
92**  F0. T
92**  F0. T
92**  F0. T
92**  F0. T
92**  F0. T
92**  F0. T
92**  F0. T
92**  F0. T
92**  F0. T
92**  F0. T
92**  F0. T
92**  F0. T
92**  F0. T
92**  F0. T
92**  F0. T
92**  F0. T
92**  F0. T
92**  F0. T
92**  F0.
  T
*eod

*end
```